UNIVERSITÀ DEGLI STUDI DI MILANO

PhD Course in Chemistry – XXXVIII Cycle

Department of Chemistry

PhD Thesis

Toward Enhanced Bimodal Sensing: TiO_2-Coated Metallic Nanostructures for Electrochemical and Photoelectrochemical Detection

SSD: CHIM/01

PhD Candidate: Daniele Fumagalli
ID: R13906
ORCID n. 0009-0000-7773-3374

Supervisor: prof.ssa Valentina Pifferi
Co-Supervisor: prof. Luigi Falciola

PhD Coordinator: prof. Daniele Passarella

A.Y. 2024-2025

1 Index

2 General introduction

2.1 Material selection

Electrochemistry has become an essential part of everyday life. Electrochemical processes are central to sustainable development, especially in advancing batteries and fuel cells, and play a crucial role in industrial applications ranging from galvanization to chemical synthesis. They are also employed for corrosion protection, which mitigates damage valued at over $2.5 trillion annually.[1]

One often-underappreciated branch of electrochemistry is electrochemical sensing, which has historically been overshadowed by more traditional analytical techniques. While common devices like pH meters and glucometers are well-known, the potential of electrochemical sensors extends far beyond.

The development of low-cost, easily deployable sensors has the power to revolutionize multiple fields. In healthcare, wearable sensors with IoT integration simplify patient monitoring and treatment. Biosensors with ultra-low detection limits can track biomarkers in bodily fluids. In environmental applications, commercial electrochemical (EC) sensors already detect gases like CO, NO_2, O_3, and SO_2.[2]

Despite some persistent challenges - such as limited lifespan, stability, and selectivity - the advantages of EC sensors are compelling. These include miniaturization, integration with IoT and AI, multi-analyte capability, and affordability. They also enable on-site monitoring in industrial and environmental contexts, reducing the need for complex sampling, preprocessing, and specialized expertise.

It is within this broader context that my thesis is framed. To support the development of EC sensors, new analytical techniques and material preparation methods must be explored.

Over the past few decades, photoactive materials—particularly semiconductors and organic dyes—have gained significant attention for their role in solar energy conversion and photoelectrochemical applications. Semiconductors, in particular, are favored for their chemical stability, cost-effectiveness, and widespread industrial applicability. When irradiated with light of suitable energy, these materials undergo charge separation, generating electron-hole pairs. The photogenerated charges can follow distinct pathways: electrons (or holes) may migrate through the bulk of the semiconductor and be collected via an external circuit, while the complementary charges remain at the surface, where they can participate in redox reactions with adsorbed molecules.

The extent of the chemical reactions can be monitored and controlled by combining irradiation and the application of a potential via standard electrochemical setup. The main advantage of photo-electrochemistry is the separation of the exciting source (the light source) and the recorded signal (the current flowing through the potentiostat). This allows to improve the quality of the analytical measures by obtaining a better signal to noise ratio.[3,4]

Titanium dioxide (TiO_2), a cheap and non-toxic semiconductor, was selected as photoactive material for this work. It is a white solid with peculiar properties, such as opacity and a very high refractive index, giving it plenty of applications as a pigment: paintings, medicines, food coloring, plastics and paper are just some of them. Moreover, it is used as sunscreen in cosmetics, UV blocking agent in plastics industry and in self-cleaning surfaces—thanks to its photoactivity.[5–12]

Titanium dioxide can crystallize in several polymorphic forms, yet only rutile and anatase are naturally occurring. The metastable anatase phase is particularly favored in photocatalytic applications due to its enhanced charge carrier dynamics, including the contribution of carriers from deeper within the bulk material. Rutile, on the other hand, represents the thermodynamically stable phase and typically forms at elevated temperatures between 600°C and 800°C. It is also recognized as the second most abundant mineral source of titania, following ilmenite ($FeTiO_3$).[13]

The typical photoelectrochemical process is schematized in Figure 2.1. Like other semiconductors, when TiO_2 is irradiated at suitable wavelengths (typically in the UV range), it undergoes charge separation. Being an n-type semiconductor, the resulting photogenerated holes (h^+) interact with adsorbed molecules on the surface. This leads to an anodic photocurrent, proportional to the interaction of photogenerated holes and adsorbed molecules. For anatase, the band gap is reported between 3.2–3.4 eV (about 388 nm).

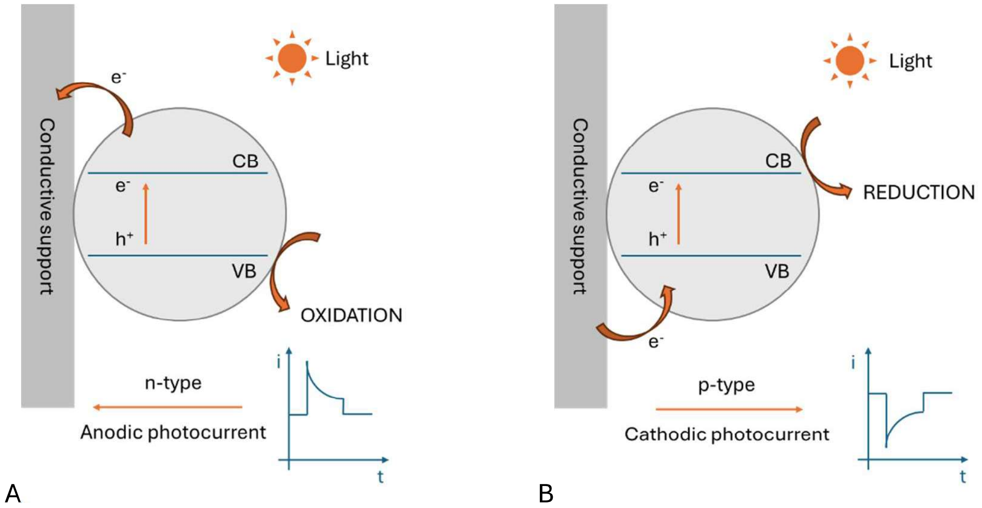

Figure 2.1 - Typical photo-electrochemical behavior of n-type and p-type semiconductors

These photogenerated charges, especially when combined with an externally applied potential, can drive photoelectrochemical (PEC) reactions. PEC sensors have gained attention for their advantages: high stability, low power consumption, rapid response, operational simplicity, and reduced background noise—thanks to the separation between the excitation source and the detected electrical signal.[3,4]

TiO_2 was among the first materials studied for PEC applications, due to its known photocatalytic properties. Nonetheless, limitations remain: rapid recombination of photogenerated charges and activity limited to intense UV light. To overcome these issues, researchers have developed strategies such as morphological tuning, doping, quantum dot sensitization, cocatalyst deposition, and formation of heterojunctions.

The latter, in particular, has proven effective—especially when forming semiconductor–metal nanoparticle heterojunctions. Photogenerated electrons can transfer to metal nanoparticles and remain trapped via Schottky barriers, preventing recombination. Moreover, using metals with localized surface plasmon resonance (LSPR) properties (e.g., Au and Ag) enhances visible light absorption.

The combination of materials to achieve superior properties is a central strategy in modern chemistry. Electrochemical measurements often rely on active materials that catalyze reactions efficiently—typically precious metals like Pt, Ir, Au, or Ag. Integrating these with more abundant and cost-effective materials is both economically and environmentally necessary.

The combined presence of TiO_2 and metal catalysts allows on the one hand to continue to exploit the catalytic properties of the metals, and on the other to introduce in the device the photoactive properties of TiO_2.

Wet-chemical methods are among the most widely employed strategies for the synthesis of metal nanoparticles and their subsequent deposition on conductive supports; however, they present several intrinsic drawbacks that limit their applicability in device fabrication. These approaches typically require the use of chemical reducing agents, stabilizers, or surfactants, which can introduce impurities and complicate post-synthesis purification. Moreover, the spatial distribution of nanoparticles on the support is often poorly controlled, leading to aggregation or uneven coverage, while the overall metal loading is difficult to tune with precision. In many cases, molecular linkers are required to anchor the nanoparticles to the substrate, which can compromise electrical conductivity and long-term stability. The nanoparticles are then drop-casted on top, and weakly bond to the surface. As a result, the obtained devices frequently suffer from metal leaching or detachment under operational conditions, reducing their durability and reproducibility. [14–17]

Electrochemical deposition, although considered a greener alternative due to the absence of chemical reductants, faces similar challenges: the morphology and size distribution of the deposited nanoparticles are strongly dependent on deposition parameters, often requiring complex templating procedures, and achieving uniform coverage or precise control over loading remains difficult. [18,19]

These limitations highlight the need for advanced deposition strategies that combine nanoscale precision with chemical and structural stability.

Solid state dewetting is a physical method to prepare metal nanoparticles on solid supports without needing a chemical synthesis step. A thin metal film can be sputtered on the surface, and thermal aggregation is achieved upon heating. [20]

This process, as explained in the literature, is driven by the minimization of interfacial and surface energies. Upon heating, increased atomic mobility enables surface diffusion, leading to the rupture of the continuous film. The energetically unfavorable metal-FTO interface promotes retraction of the film into isolated nanoparticles, whose size and distribution are influenced by initial film parameters and substrate topography.[20–23]

Historically, dewetting has been studied due to the problem it poses in microelectronics, where the agglomeration of Au lines leads to break up of an interconnect, as shown in Figure 2.2.[24]

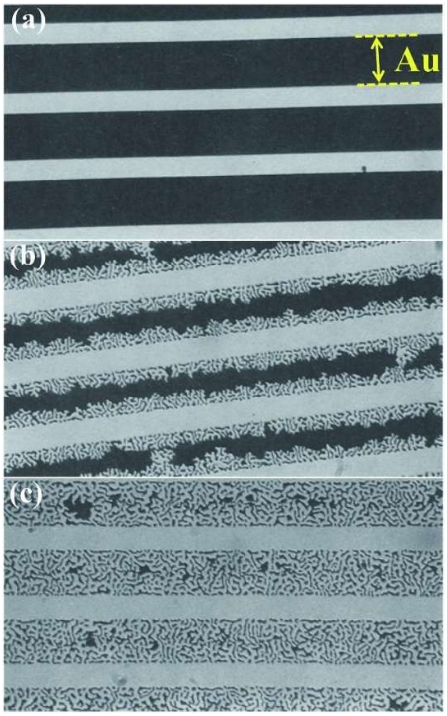

Figure 2.2 - Example of dewetting of a Au line-patterned film on a fused silica substrate: (a) before annealing; (b) partially agglomerated; (c) fully agglomerated [24]

The dewetting mechanism is reported in Figure 2.3. The solid-state dewetting process begins with the spontaneous emergence of voids or holes at specific defect sites. In the case of a policristalline film, this coincides with the grain boundaries.

This initiates a material flux (J), where atoms of the material migrate out of the dewetting zone through capillary-driven surface diffusion. The displaced metal accumulates at the dewetting front, forming a rim (Figure 2.3 A). Depending on the film's crystallographic characteristics, this rim can appear either smooth or faceted, with its height influenced by the rate of dewetting and the surface diffusion kinetics of adatoms.

As the rim retracts, a valley typically forms behind it due to Rayleigh instability. When this valley deepens enough to expose the underlying substrate, a pinch-off event occurs, leaving behind a thin line—or wire—of material (Figure 2.3 B).

Without stabilizing influences, the rim itself eventually becomes unstable over a certain length. This instability leads to the formation of large, ordered arrays of elongated features known as "fingers." Ultimately, these fingers fragment into three-dimensional islands through a beading process akin to the Rayleigh–Plateau instability (Figure 2.3 C).

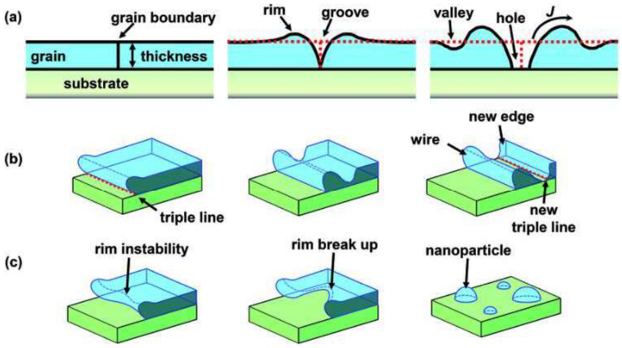

Figure 2.3 - Sketch of the mechanism of solid state dewetting of a metal thin film on a smooth surface illustrating: (a) grain boundary grooving and hole formation; (b) film edge retraction and rim pinch-off; (c) rim instability and break up

The technique is particularly versatile, and different procedures are reported in the literature to achieve the formation of nanoparticles with even more controlled size and spatial distribution: thermal heating can be coupled with laser irradiation,[25] a sacrificial polymer layer [26] or a nanostructured support can be used to guide the nanoparticles formation.

A variety of electrodes support material can be used to prepare metal nanoparticles on top, ranging from carbon and silicon-based flat surfaces [27] to glass supports like fluorine doped tin oxide (FTO) and indium tin oxide (ITO) coated glass slides, presenting higher surface roughness that could affect the dewetting process. [28]

The obtained devices are applied for a variety of applications, ranging from Surface Enhanced Raman Spectroscopy (SERS) supports[25] to plasmonic [29] and optical [30] sensors. The presence of analyte could thus cause the rise of a specific Raman peak, the shift of a Localized Surface Plasmon Resonance (LSPR) peak or the reduction of the light transmittance of the device, respectively.

Even though nanoparticles play a crucial role in electrochemical sensing, most articles related to dewetted material studies do not propose electrochemical sensing as possible application, focusing mainly on plasmonic sensors and spatially resolved catalysts.[31] Among the application in electrochemical sensing, dewetted gold is the metal that receive most attention.

Dewetted nanoparticles were studied for biosensing [32] on glass coated supports, glucose detection on graphene [33], and glyphosate detection on graphite paper. [34] Screen Printed Electrodes (SPEs) made with Boron Doped Diamond modified with Au structures, have also been used for dopamine detection, comparing the performances of different gold loadings.[35]

To enhance the reliability of electrochemical sensors, several challenges must be addressed, particularly sensor instability, caused by the loss of catalyst material, fouling and false positives.[36,37]

The first issue can be addressed by depositing a TiO_2 layer on top of the metal nanoparticles, using it to enhance the structural stability of the device. Thanks to the porous nature of the TiO_2 film, contact between the underlying nanoparticles and the solution is preserved, rather than completely isolating them.[38–40] Fouling, which can decrease sensor performance, is often mitigated by using self-renewing surfaces like titanium dioxide (TiO_2)[41]: upon irradiation, electron-hole separation occurs in the anatase semiconductor and the holes, trapped on the material's surface, can oxidize adsorbed molecules, thus cleaning the electrode's surface.[42]

While issues like catalyst loss and fouling can often be solved by improving materials or using protective layers, false positives present a more complicated challenge. These errors happen when the sensor reacts to substances that are not the target analyte but look or behave similarly, leading to incorrect results. This is especially problematic in areas like medical testing or environmental monitoring.

False positives are typically addressed through the development of advanced materials like molecularly imprinted polymers (MIPs) or bio-engineered surfaces, both of which can suffer from stability issues. As an alternative approach, a bimodal sensor, able to combine different techniques to quantify the same analyte can be designed.[43] By comparing the results of two distinct techniques, cross-validation can be achieved, enhancing the sensor's accuracy.

2.2 Target molecules

Throughout this Thesis, a variety of analytes were systematically selected and employed as model systems to investigate the electrochemical and photoelectrochemical behavior of the fabricated electrodes.

2.2.1 Ciprofloxacin

One of the fields where photo-electrochemical sensors have been applied very recently is the analysis of antibiotics[44], up to now mainly using systems with recognition elements for the analyte, such as molecular imprinted polymers, aptamers, and enzymes. These systems have the advantage of being highly selective, but facing the drawbacks of more complicated synthetic procedures and storage. Instead, thanks to the intrinsic interaction of the photoactive material with the analyte, without the need for a recognition system, more robust and simpler systems can be built.

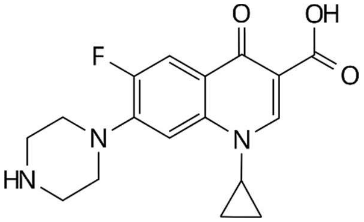

Figure 2.4 - Ciprofloxacin molecular structure

Among the antibiotics detected by PEC there is ciprofloxacin [44–49], a third-generation quinolone drug, widely applied for clinical medicine, in livestock and poultry farming, but which has been discovered to be dangerous for the environment even in small quantities, especially for toxicity problems on wastewater and surface water. Ciprofloxacin molecular structure is reported in Figure 2.4. However, these studies are few and above all based on analyses in which the drop in the photocurrent (signal-off type PEC, see Figure 2.5) is observed due to the presence of ciprofloxacin on the surface of the photoelectrode, which hinders the electron transfer [45–48]. This type of detection is more problematic for interferents than a signal-on type PEC, where there is a real chemical reaction between the photoactive material and the analyte and therefore an increase in the photocurrent signal.

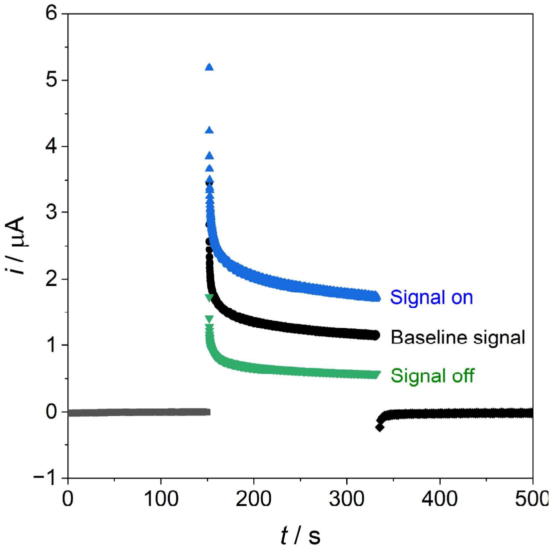

Figure 2.5 - Comparison of signal off and signal on PEC detections. Blu and green values are recorded when the analyte is present

The oxidation process, already investigated in the literature, involves the oxidation of the piperazine ring.[50] This investigation of this process is particularly important in the field of environmental remediation, as can lead to the formation of toxic byproducts.[51]

In Chapter 4, the heterojunction formed by gold nanoparticles coated with a porous titanium dioxide film is investigated for the first time for the signal-on photoelectrochemical determination of ciprofloxacin, using low power light sources. The goal is to obtain a robust system, with good analytical parameters and without interference problems. The system will be compared with titanium dioxide alone, to fully understand the key role represented by the semiconductor-metal heterojunction.

2.2.2 H_2O_2

Another molecule used to probe the response of the devices is hydrogen peroxide (H_2O_2). This molecule was selected to test uncovered Au structures due to its ability be easily detected on gold structures, while not being affected by the underlying FTO conductive support.

Furthermore, the ability to detect the molecule either via electrochemical oxidation or reduction paves the way for the development of the bimodal detection previously introduced, where two complementary techniques used on the same device allow to achieve internal cross validation and improve the reliability of the detection.

The reaction of H_2O_2 is also widely known in the literature.[52] The expected CVs are reported in Figure 2.6:

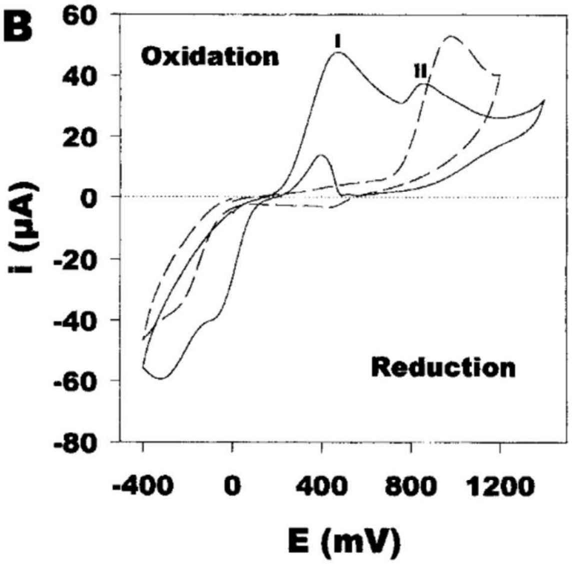

Figure 2.6 - CV of gold electrode pH 7.4 phosphate buffer in presence of 10 mM H_2O_2 before and after sonication, retrieved from the literature [52]

The continue curve reported in Figure 2.6 is recorded with a gold disk electrode in pH 7.4 phosphate buffer in presence of 10 mM H_2O_2. It clearly presents two oxidation peaks, the first one at +490 mV vs Ag/AgCl and the second one at +870 mV vs Ag/AgCl. If the solution is stirred or sonicated, the first peak decreases and the second one increases concomitantly until the first one completely disappears. The use of polishing material for the pre-treatment of the gold electrode also leads to the inhibition of the first peak. It is believed that the presence of organic compounds (like surfactants) lead to a loss of hydrophilicity of the gold surface and a competitive adsorption between hydroxide ions and any organic trace. This phenomenon dramatically affect the electrochemical oxidation of H_2O_2.[53–57]

The same effect can happen when working with solution contaminated with any soluble compound readily adsorbed on gold, like Cl^- or trace contaminations in deionized water.[56] This can justify the lack of consensus in the literature, where some works focus on the potential of + 800 mV and other notice the oxidation at + 475 mV. [58,59]

In acidic solutions (pH 4.7 acetate buffer, pH 2 sulfuric acid), only the second oxidation peak is observed.

In alkaline media (pH 10.5 borate, pH 12 NaOH) the observations reported for pH 7.4 are still valid, but a high reoxidation component in the cathodic scan can be observed, similarly to what happens with glucose on gold.[60]

CV data reported in literature show that leaving gold electrodes in air for 2 days leads to the inhibition of the first peak and extensive mechanical and electrochemical cleaning is needed in order to recover it, suggesting that a layer of gold oxide can inhibit the first peak. It is therefore suggested that the pre-oxidized form of gold (Au-OH) favors the reaction, likely because of H-bonding between -OH groups physiosorbed on the surface and H_2O_2. [61,62]

As for the reduction of H_2O_2, when the first anodic peak is observed, two cathodic signals can be observed (one related to H_2O_2 and one to the oxygen produced in the anodic scan), while this distinction could not be observed in the cases where only the second anodic peak was observed.[58] It is also possible to study the behavior of H_2O_2 using chronoamperometry. In this case, working at a constant potential is not advised. A multiple-pulse chronoamperometry leads to better results as reported in the literature.[59]

Although the study of the reaction mechanism lays outside the scope of this thesis, a list of possible reactions involving H_2O_2 is reported in Table 2.1.[63]

Table 2.1 - List of reactions involving H_2O_2 on a metal electrode

pH	Pathway	Reactions	E^0 vs. RHE[1]
<7	Direct four-electron	$O_2 + 4H^+ + 4e^- \rightarrow 2\ H_2O$	1.230
<7	two-electron	$O_2 + 2H^+ + 2e^- \rightarrow H_2O_2$	0.695
<7	-	$H_2O_2 + 2H^+ + 2e^- \rightarrow 2\ H_2O$	1.776
>7	Direct four-electron	$O_2 + 2\ H_2O + 4e^- \rightarrow 4\ OH^-$	1.230
>7	two-electron	$O_2 + H_2O + 2e^- \rightarrow H_2O^- + OH^-$	0.695
>7	-	$H_2O^- + H_2O + 2e^- \Rightarrow OH^-$	1.776

For the remainder of this thesis, sodium perchlorate ($NaClO_4$) was used as the supporting electrolyte. This choice was guided by literature reports indicating that perchlorate ions exhibit minimal interaction with gold surfaces. As a result, $NaClO_4$ provides a chemically inert background that avoids unwanted side reactions or surface modifications, ensuring that the observed electrochemical behavior is primarily due to the analytes under investigation.

2.2.3 Cetirizine

Building on the extensive and promising results achieved with the TiO_2–gold composite system, the focus of this work then shifts toward exploring a related, yet distinct, material configuration by substituting gold with silver. This modification aims to investigate how the different physicochemical properties of silver influence the overall electrochemical and photoelectrochemical performance of the TiO_2-based composite, and to assess its potential for sensing applications. Silver presents interesting electrochemical properties, e.g. excellent catalysis toward reductive dehalogenation of organic molecules. [64–66]

In fact, modification of the electrodes with silver structures received great consideration in sensing application due to their ability to increase the surface area and conductivity of the material, but also thanks to their specific catalytic properties.[67]

A specific analyte was selected to be the target of this study: cetirizine (CTZ), whose structure is reported in Figure 2.7. In this piperazine derivative, hydrogens attached to nitrogen are replaced by a (4-chlorophenyl)(phenyl)methyl and a 2-(carboxymethoxy)ethyl group, respectively. Commonly used as antihistaminic, it is widely considered a second generation drug due to its low activity on the central nervous system, which prevents side effects like drowsiness, but has different physicochemical, pharmacokinetic, and pharmacodynamic behaviour.[68]

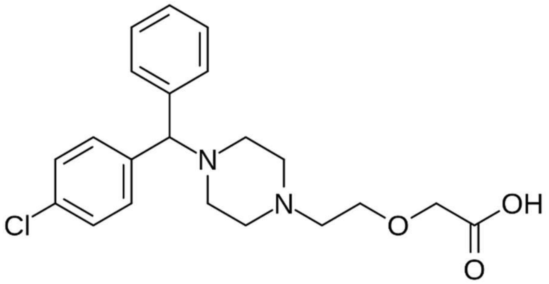

Figure 2.7 - Cetirizine molecular structure

The molecule, assumed orally, is poorly metabolized,[69] and is commonly found in wastewaters with variable concentration, depending on the incidence of seasonal allergies, and is not removed effectively by treatment plants and is stable in river water.[70,71]

Cetirizine is reported in the literature to be detected via pulsed voltammetric techniques (namely Square Wave Voltammetry – SWV) at relatively high overpotential (1.0 V vs Ag/AgCl) using disposable carbon based electrodes.[72] Oxidation of the molecule can also be carried out on carbon materials after modifications, e.g. with l-leucine,[73] poly-methyl orange,[74] graphene oxide and cholesterol, [75] graphene and ZnO NPs.[76] Carbon nanotubes, modified with silver-doped TiO_2 nanoparticles, were also used for the electrooxidation of cetirizine. [77] The mechanism of cetirizine oxidation has been widely studied and, according to the literature it starts with the N- oxidation of the sterically less hindered piperazine nitrogen.[78]

On the other hand, the molecule presents other functional groups such as a chlorine atom, which can be the site of a reductive dehalogenation catalyzed by metal structures, especially silver.

Interestingly, although it is known in the literature that silver has good catalytic activity toward the reduction of halogenated molecules,[79,80] most sensing works focus instead on the oxidation of the cetirizine molecule, and none of them exploits a bimodal electrochemical- photoelectrochemical detection.

In the final chapter of this thesis, the concept of bimodal sensing is experimentally validated by employing a single device to detect cetirizine through two distinct mechanisms: photoelectrochemical oxidation and electrochemical reduction, as schematized in Figure 2.8. By applying both detection modes to the same analyte under comparable conditions, the study enables internal cross-validation of the results. This dual-mode approach not only enhances the robustness and reliability of the sensing platform but also provides complementary insights into the analyte's electrochemical behavior, thereby strengthening the overall analytical performance of the device.

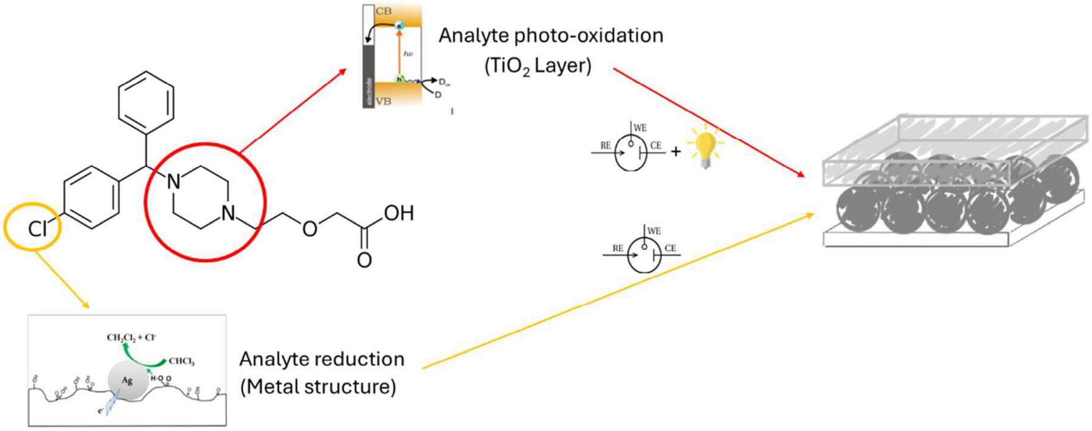

Figure 2.8 - Schematized representation of the bimodal detection performed toward cetirizine using a FTO/Ag/TiO$_2$ electrode

2.3 Aim of the Thesis

This thesis examines the preparation, characterization, and implementation of electrochemical sensors that integrate the properties of metallic structures with a titanium dioxide (TiO_2) layer. The first chapter investigates TiO_2 itself, aiming to optimize deposition parameters, especially sol aging time, and highlights its significant influence on the photoactivity of the resulting layer.

In the second chapter, a proof-of-concept device is introduced that combines the TiO_2 layer with chemically synthesized and drop-casted gold nanoparticles. While this configuration demonstrates enhanced sensing performances compared to TiO_2 alone, it also reveals the limitations of the deposition method in terms of reproducibility and control over the nanoparticle quantity. Consequently, the need for a more refined approach becomes evident.

Chapter three presents a new physical technique for nanoparticle preparation. These structures are extensively characterized and evaluated for their stability and electrochemical behavior, and tested toward the detection of H_2O_2.

The dewetted structures are subsequently coated with TiO_2. A comparative analysis between the coated and uncoated systems follows, emphasizing two major findings: the complete sensor structure exhibits increased surface stability compared to configurations with exposed metallic features, and the TiO_2 layer—while slightly reducing electrochemical sensitivity—enables the incorporation of photoactive functionality. This dual capability results in a bimodal sensing platform that can perform both electrochemical and photo-electrochemical measurements.

The final chapter explores the potential of silver-based structures as alternatives to gold. Although silver proves to be less stable, it offers promising catalytic properties. To counteract its instability, a TiO_2 coating is applied to prolong durability, and the final sensor is tested across both electrochemical and photo-electrochemical modalities, proving experimentally the concept of bimodal electrochemical and photo-electrochemical detection.

3 TiO$_2$ investigation

Titanium dioxide (TiO$_2$) layers were deposited using a conventional wet chemical method on conductive fluorine doped tin oxide (FTO) coated glass slides. The process began with the preparation of a TiO$_2$ sol from titanium (IV) isopropoxide as the precursor, which was then allowed to age, promoting the formation of TiO$_2$ in slightly acidic environment. An FTO electrode was subsequently dip-coated in the sol to deposit a thin film. Although the method required considerable operator expertise, it yielded reproducible results. Finally, the coated electrode was calcinated at high temperature to induce the formation of the anatase crystalline phase, known for its excellent photoactivity and thermal stability. The detailed procedures are reported in Chapter 10.1.

The preparation and aging of the TiO$_2$ sol used for the coating were extensively studied and optimized, continuing the development from previous works.[40–42,81,82] The sol proved to be very susceptible to temperature and humidity, and the electrochemical behavior of the TiO$_2$ changed depending on the sol aging time, probably due to a change in the film's morphology. Aging time between 7 and 60 days were selected for the sol aging time study.

As shown in Figure 3.1, cyclic voltammetry (CV) curves' shape of FTO/TiO$_2$ electrodes change with the sol aging time, suggesting that a different diffusion process takes place at the electrode surfaces.[83] In particular, the peak-like shape observed at 7 days of sol aging is compatible with linear diffusion, while the step-like signal at longer sol aging periods indicates the presence of convergent diffusion. Further information and the theoretical background of diffusion processes are presented in Section 9.1. Electrochemical Impedance Spectroscopy (EIS) measurements also confirm that the films at various aging times are characterized by a different charge transfer resistance. One possible hypothesis is that during the aging of the sol, TiO$_2$ nanoparticles increase their size, and this leads to a different morphology of the film with different pore size and different overall thickness. The higher resistance recorded for 14 days of aging is compatible with a more uniform layer.

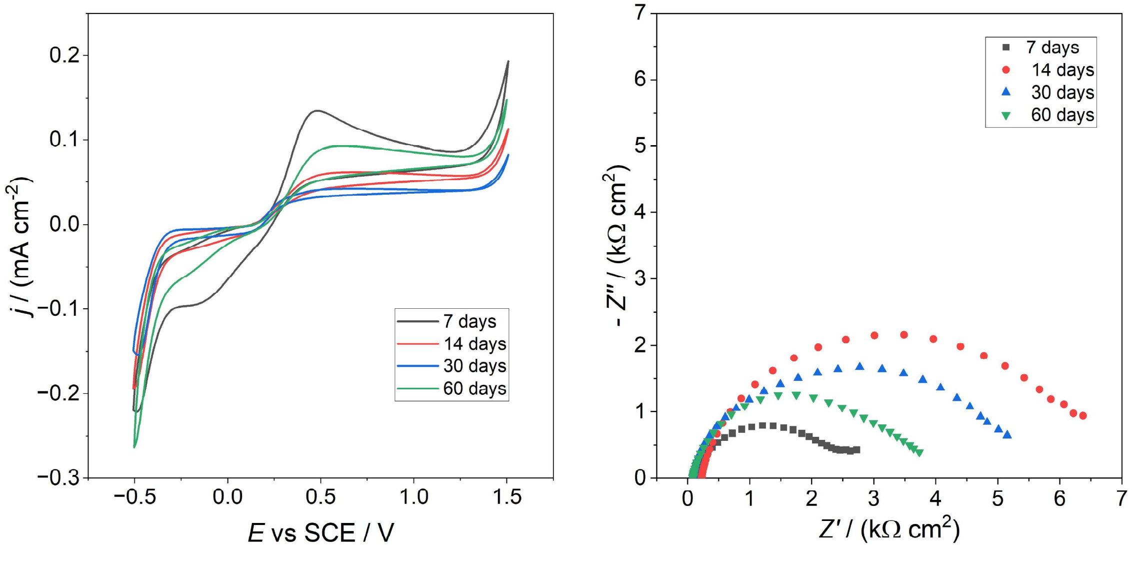

Figure 3.1 - (left) CV recorded with a FTO/TiO$_2$ electrode at 100 mV/s in NaClO$_4$ 0.1M, using 3 mM K$_4$[Fe(CN)$_6$] as probe molecule; (right) EIS measurements recorded in the same conditions

Different batches of soil were prepared, months apart, and each batch was used to prepare bare TiO_2 electrodes and composites materials, focusing in particular on the photoactive behavior of the electrodes.

Analyzing the photocurrent response of the bare TiO_2 electrode it was found that a specific trend in the photocurrent intensity could be observed, with a maximum in the signal intensity observable around two weeks of sol aging. The trend is maintained by changing the operating conditions, e.g. by moving from a high power irradiation source (Figure 3.2 A) to a low power one (Figure 3.2 B). Different batches of TiO_2 presented the same trend.

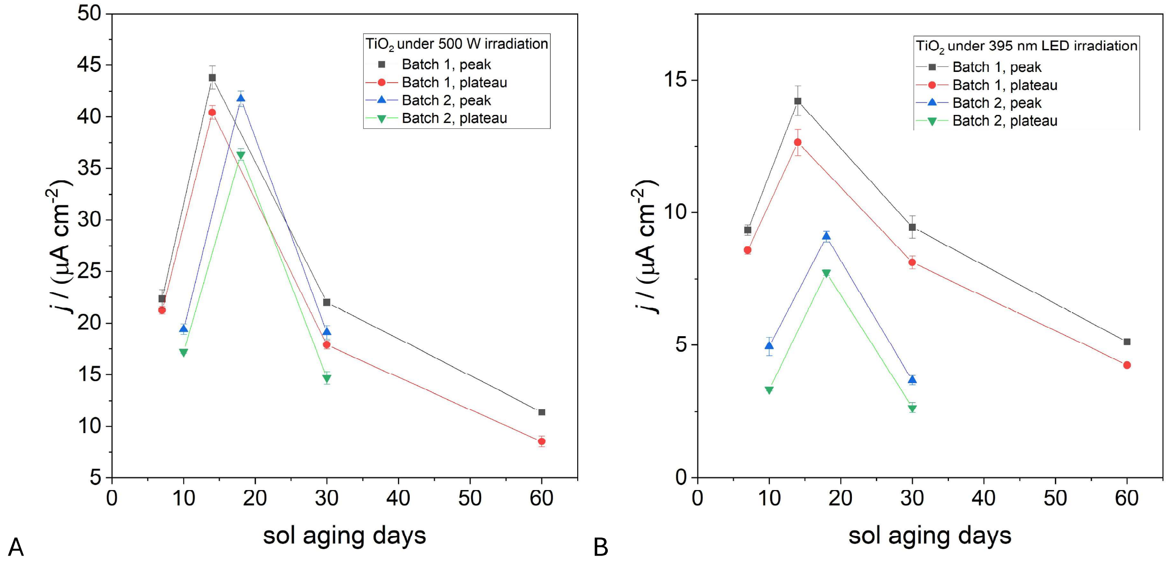

Figure 3.2 - Photocurrent intensity trend of a TiO_2 electrode under different light sources: (A) a 500W UV lamp – the emission spectra is reported in Chapter 10 - and (B) a low power LED at 395 nm

By analyzing the shape of the normalized photocurrent signal, reported in Figure 3.3 A, it is clear that the photocurrent decay happens with different electron-hole recombination times depending on the sol aging time. To get a better understanding of the occurring process, the e-h recombination times of the materials were calculated using a bi-exponential fitting of the form $y = y_0 + A_1 e^{-x/t_1} + A_2 e^{-x/t_2}$.

The obtained data confirm the trend observed with the intensity: for bare titanium dioxide, slightly higher electron-hole recombination times were obtained at 14 days of aging. This increase in recombination time indicates a reduced rate of electron-hole pair annihilation, which is beneficial for photocatalytic applications. Slower recombination allows charge carriers (electrons and holes) to survive longer, increasing the likelihood that they will participate in surface reactions before recombining.

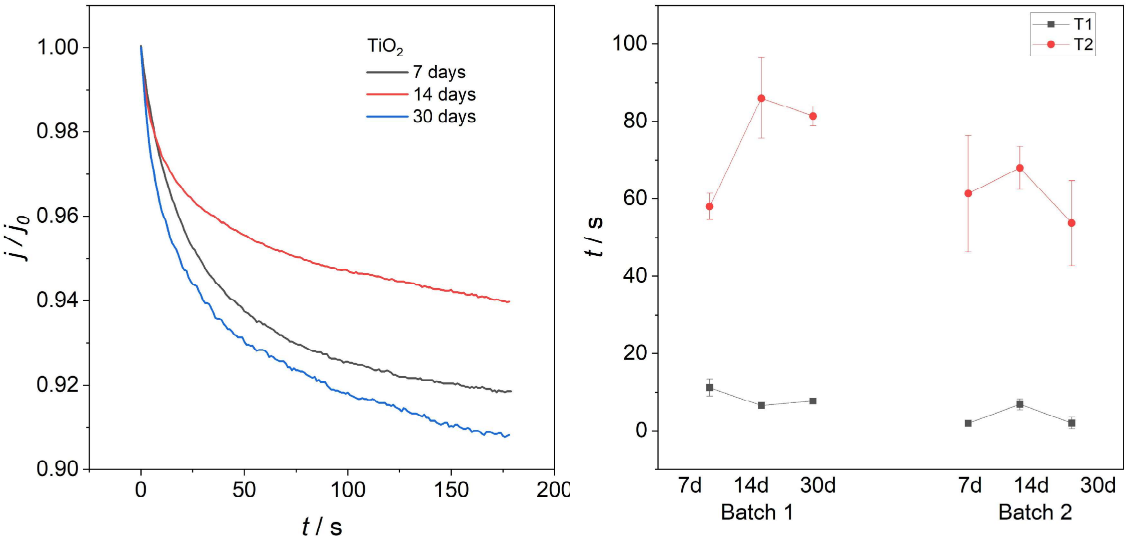

Figure 3.3 - (A) Normalized photocurrent for TiO_2 electrodes prepared with different sol ageing times and (B) TiO_2 e-h recombination times calculated for different baches of TiO_2 sol

It is clear from the tests that the best results are obtained when the TiO_2 deposition is carried out using a two weeks old sol, and therefore these conditions will be used for the rest of the Thesis.

The thickness of the TiO_2 layer was investigated in collaboration with previous member of the ELAN group.[11] Profilometry measurements were conducted using two FTO-coated glass slides partially dipped in a TiO_2 sol. One resulting graph is reported in Figure 3.4: the profilometer tip moves from the uncoated area to the coated region, and the height difference between the two was calculated. The TiO_2 layer aged for 7 days is thicker than the layer at 14 or 30 days of aging. This could lead to deeper pores on the surface of the titanium dioxide layer and thus to a different diffusion mechanism (in this case, linear diffusion), as already proven with CV.

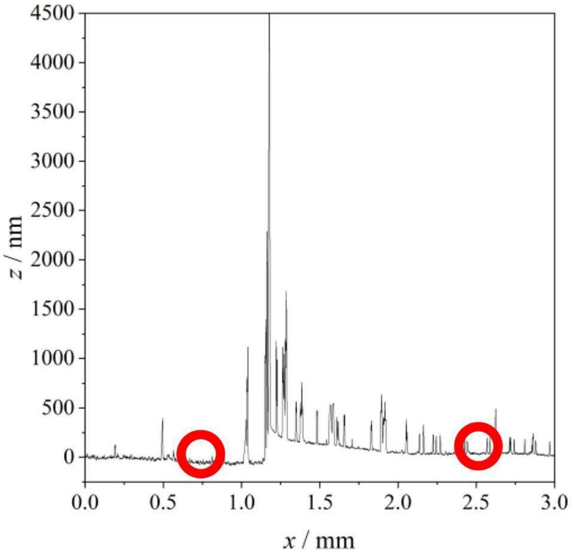

Figure 3.4 - Profilometric graph. The red circles are the point where the point s were taken for the measurement

	7 days	14 days	30 days
Sample A	(155 ±52) nm	(55 ±22) nm	(84 ±25) nm
Sample B	(99 ±19) nm	(72 ±13) nm	(81 ±13) nm

Table 3.1 - Thickness values of different FTO/TiO_2 electrodes prepared at different aging times of the sol.

It is also worth noting that although the same trends are observed in all the prepared baches of TiO_2 sol, the overall intensity varies a lot, and is highly susceptible to ambient conditions, like humidity and temperature. Unfortunately, it was not possible to work in a climate-controlled room, and this sometimes leads to non-uniform TiO_2 coverage on the electrodes, as shown in Figure 3.5. The surface is often characterized by the presence of uncovered FTO surface (light-colored regions), thicker TiO_2 deposits (the darker regions in the SEM images) and crevices that separate the more uniform TiO_2 regions.

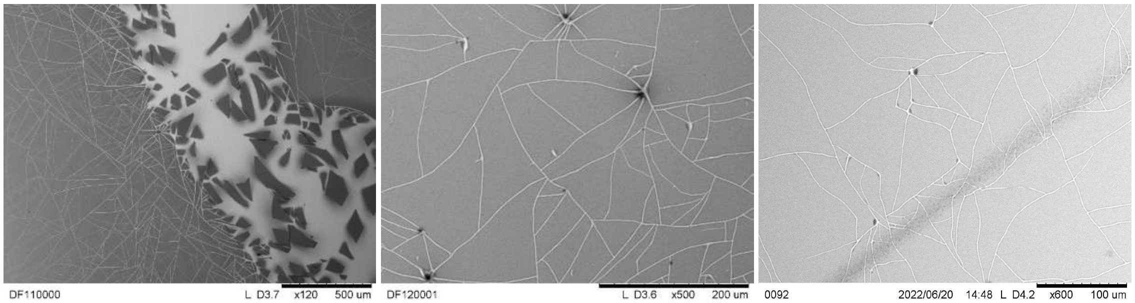

Figure 3.5 - TiO_2 layer deposited on FTO glass slides

This non-uniformity can greatly affect the analysis, especially when metal structures are present below the TiO_2 layer. One extreme example is reported in Figure 3.6, where it is possible to observe uncovered FTO surface as the light grey region, TiO_2 deposits (grey and black, depending on the thickness) and exposed gold structures (white points). The composition of the different regions was identified using SEM-EDX point-measures.

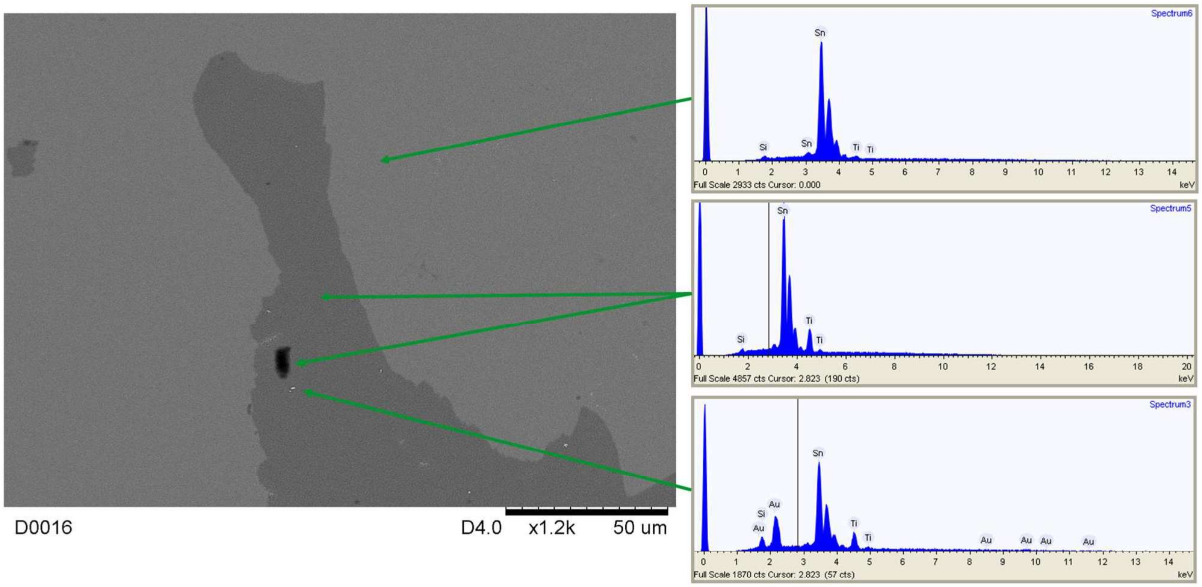

Figure 3.6 - SEM image of a FTO/Au/TiO_2 electrode with EDX spectra recorded at specific points

X-Ray Diffraction (XRD) measures, reported in Figure 3.7, indicate the presence of the crystal structure of anatase, confirming previous reports present in the literature,[40] although a component of amorphous TiO_2 is also present, covering most of the 101 anatase signal at 25.08°. The intense lines at 27.18°, 34.36°, 38.36°, and 52.12° are attributed to the 110, 101, 200 and 211 planes of the SnO_2 crystal structure cassiterite, respectively. The presence of high crystallinity SnO_2, already discussed in the literature for these electrodes, is required to achieve the low electronic resistance of the FTO-coated glass slides.[84]

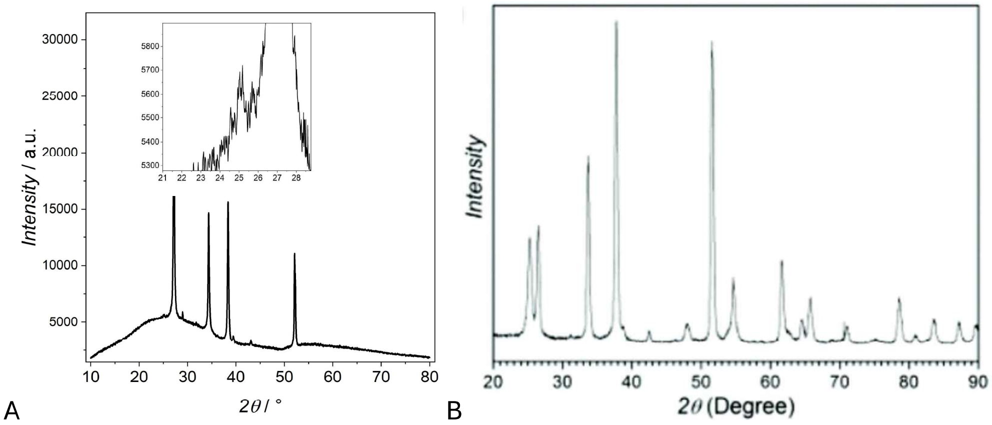

Figure 3.7 - XRD pattern of (A) one of the prepared devices and (B) TiO_2 prepared using the same procedure, according to the literature

4 Hybrid AuNPs/TiO_2 electrode

In this chapter, the previously introduced TiO_2 layer will be used to cover drop-casted gold nanoparticles. The main goal is to understand how the properties of this new "hybrid" material compare to those of a bare TiO_2 film, especially regarding the photo-electrochemical (PEC) performances.

4.1 Electrodes Preparation and characterization

The preparation of the device is schematized in Figure 4.1 and its experimental details are reported in Section 10.1 (preparation of the TiO2 sol), 10.2 (preparation of the gold nanoparticles) and 10.3 (gold nanoparticles deposition).

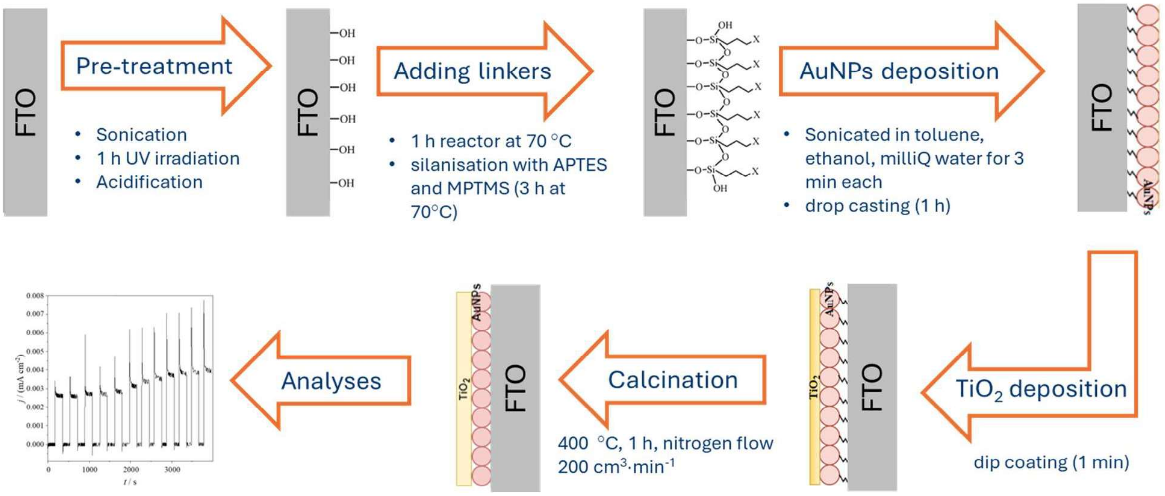

Figure 4.1 - Preparation of a TiO_2/AuNPs/FTO electrode

The final device is composed of gold nanoparticles (AuNPs) covered by a titanium dioxide (TiO_2) layer, as presented in the scheme of Figure 4.2 A.

The nanoparticles were obtained with a Turkevic synthesis and were characterized by UV-vis spectroscopy, obtaining the classic 520 nm plasmon band (Figure 4.3 A), and by DLS measurements, showing an average size for the nanoparticles of 10 nm (Figure 4.3 B). After synthesis, gold nanoparticles were immobilized on a Fluorine doped Tin Oxide conductive glass (FTO), through the use of silanes. The TiO_2 layer was subsequently placed by dip coating in a previously prepared sol and the electrode was thus calcined.

EDX measurements were perfromed on the electrode's surface. The peaks without labelling at 3 and 4.2 keV are attributed to Sn, while no peak could be observed for Au due to its low concentration. (Figure 4.2). From the SEM image it can be observed that the electrode surface is very uniform Figure 4.2 (inset B) and the average roughness obtained at the AFM is (8.6 ± 0.9) nm (Figure 4.2 inset C).

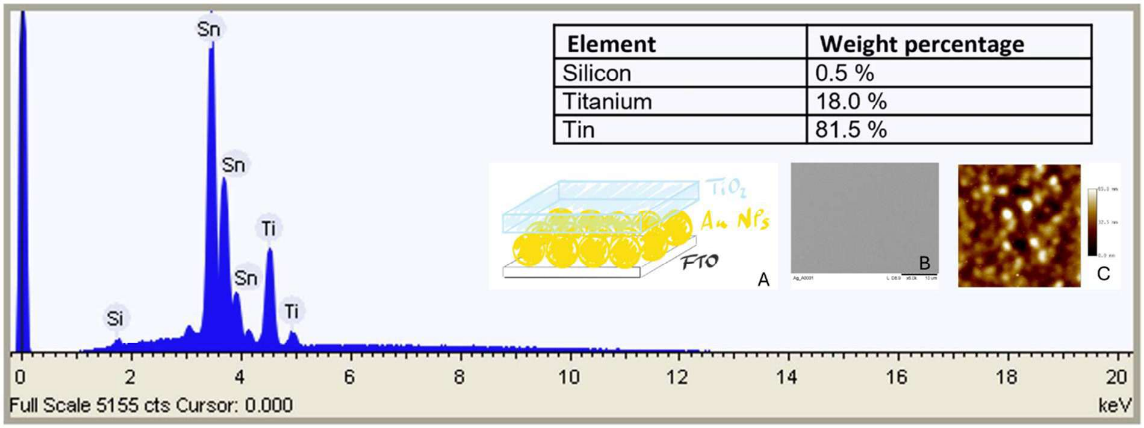

Element	Weight percentage
Silicon	0.5 %
Titanium	18.0 %
Tin	81.5 %

Figure 4.2 – EDX spectra of the obtained electrode. The device's structure (A), SEM (B) and AFM (C) images of the surface are reported as insets

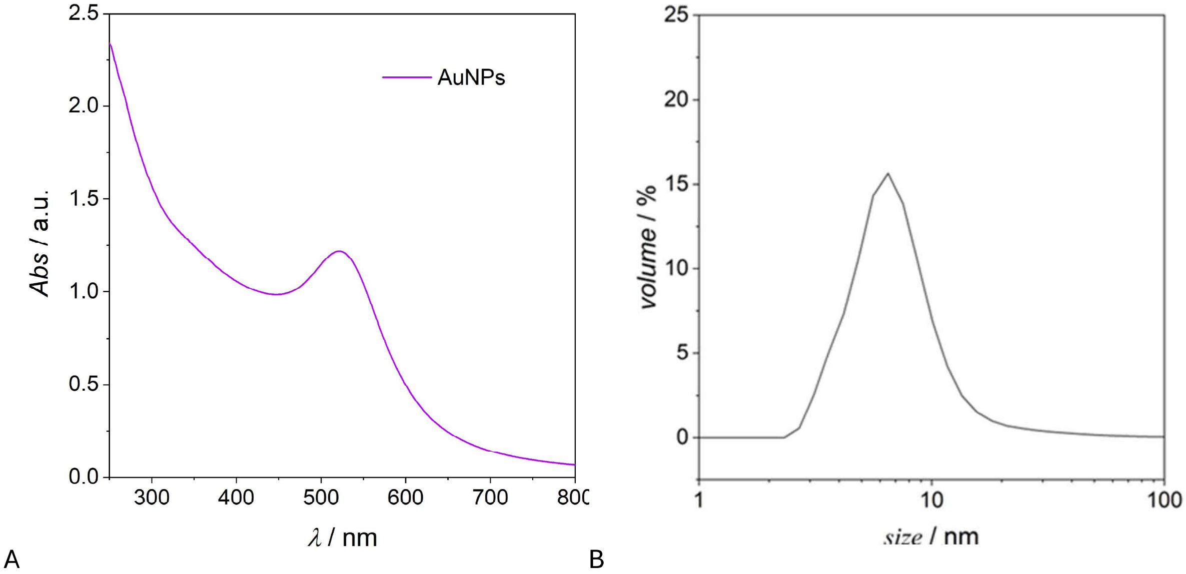

Figure 4.3 - UV-vis spectra (A) and DLS measurements (B) of the prepared nanoparticles

The device (TiO_2/AuNPs) was electrochemically characterized by Cyclic Voltammetry (CV) and Electrochemical Impedance Spectroscopy (EIS), also considering the comparisons with the individual components: only conductive glass (FTO), gold nanoparticles deposited on FTO (AuNPs) and titanium dioxide deposited on FTO (TiO_2).

Cyclic voltammetry performed on the electrolyte solution without the presence of molecular probe (Figure 4.4 A, inset) shows that FTO and TiO_2 present no signal, as expected, while AuNPs and TiO_2/AuNPs show the typical oxidation plateau and the reduction peak of gold. The latter are evident, especially for TiO_2/AuNPs, indicating a stabilization and a better electrochemistry of gold nanoparticles after coverage with titania layer. It is also important to consider that this coverage inhibits the loss of gold in solution during the analyses, as instead happens for AuNPs (Figure 4.4 B).

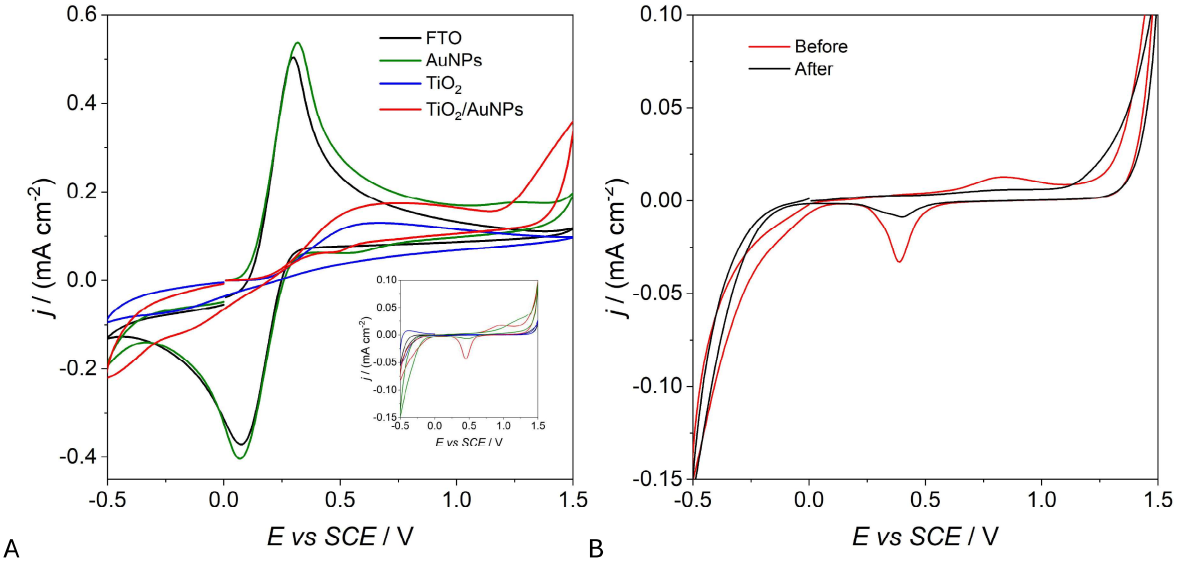

Figure 4.4 – (A) CV recorded in $NaClO_4$ 0.1 M with and without (inset) ferrocyanide. (B) Evolution of the CV shape of exposed gold nanoparticles on FTO

Cyclic voltammetry performed in the presence of $Fe[CN_6]^{4-}/Fe[CN_6]^{3-}$ as probe molecule (Figure 4.4 A) shows the typical peak signals for FTO and AuNPs, slightly more intense when gold nanoparticles are present. For TiO_2 and TiO_2/AuNPs, on the other hand, the signal appears to be a step, indicating that a different diffusion mechanism is present when the titania layer covers the electrode. In fact, it appears to be porous, and confirms the presence of a convergent diffusion mechanism.

The convergent diffusion is also confirmed by the study of the scan rates [83], which shows a slope of the logarithmic graph (Table 4.1, 2nd column) that deviates from the typically planar diffusion value of 0.5 for the two samples covered by titania. Moreover, the faradic current is higher for TiO_2/AuNPs than for TiO_2, since the presence of gold helps the probe reaction.

	ln(j) VS ln(v)	CPE_{DL} / µF cm^{-2} $s^{\alpha-1}$	α_{DL}	R_{CT} / Ωcm^2	R_W/ Ωcm^2	α_W
FTO	0.46	17.4	0.86	56.8	2380	0.500
AuNPs	0.416	1240	0.44	91	8670	0.52
TiO_2	0.38	10.3	0.850	2836	2852	0.19
TiO_2/AuNPs	0.20	15.9	0.860	2836	356	0.11

Table 4.1 - CV and EIS parameters for FTO, AuNPs, TiO_2 and TiO2/AuNPs in the presence of $[Fe(CN)_6]^{4-}/[Fe(CN)_6]^{3-}$ 3 mM in 0.1M $NaClO_4$

Electrochemical impedance spectroscopy performed in the presence of the probe molecule shows a similar trend in the complex plane plot for all samples (Figure 4.5 A), with a semicircle at high frequencies and a line at low frequencies. This trend is also confirmed by the presence in the Bode plot (Figure 4.5 B) of a peak for all samples.

The equivalent circuit employed to fit experimental data is the typical Randles circuit (Figure 4.5, inset), composed by the cell resistance R_W in series with the electrical double layer capacitance CPE_{DL} and the charge transfer resistance R_{CT} (in series with an open Warburg element, Z_W), respectively in parallel. The electric double layer capacitance was fitted with a constant phase element (CPE), since the electrode surface is not completely homogeneous, and it is higher and more inhomogeneous (α_{DL} further from 1) for AuNPs (Table 4.1, 3rd and 4th columns), as expected.

The R_{CT} values are instead very low for FTO and AuNPs, since they are completely conductive surfaces, while they obviously increase for TiO_2/AuNPs and TiO_2, recording the highest value for TiO_2. These results are also visible by observing the diameter of the semicircle in the complex plane plot (Figure 4.2 A) and the frequency of the peaks in the Bode plot (Figure 4.2 B), since the higher the frequency, the easier the reaction, and confirm the trend of the peaks in CV (Figure 4.4). The analysis of the mass transfer, instead, shows the presence of a very strong convergent diffusion (as previously observed by CV), especially for TiO_2/AuNPs. In this case the lowest value of resistance to mass transfer R_W and a_W are recorded (Table 4.1, 5th and 6th columns), further from 0.5 (typical of a planar diffusive controlled system), as can also be seen from the Bode graph.

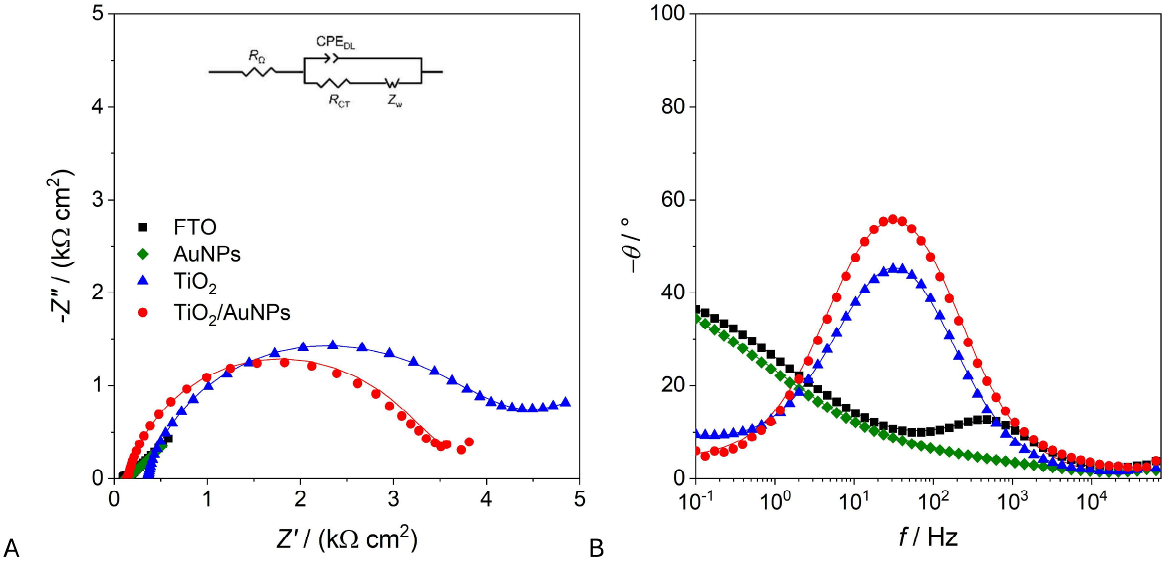

Figure 4.5 - Complex plane plots (A) and Bode phase plots at + 0.25 V (B) registered in 0.1 M $NaClO_4$ in the presence of 3 mM $[Fe(CN)_6]^{4-}$/$[Fe(CN)_6]^{3-}$ for FTO, AuNPs, TiO_2 and TiO_2/AuNPs

4.2 PEC characterization

Considering that the aim of this chapter is to try to use the complete device for photo-electroanalysis, it is also important to carry out a photoelectrochemical characterization by means of electrochemical impedance spectroscopy and photocurrent analysis, comparing especially the samples containing titania.

From the impedance analyses carried out on the electrolyte in the dark or under irradiation, semicircles in the entire frequency range are obtained for all cases in the complex plane plot (Figure 4.6 A). The corresponding equivalent circuit (Figure 4.6, inset) is composed by the cell resistance R_W in series with the electric double layer capacitance CPE$_{DL}$ and with the film resistance R_F, respectively in parallel.

From a first analysis it can be seen that for both TiO_2 and TiO_2/AuNPs systems the diameter of the semicircles and the film resistances (Table 4.2, 5th column) decrease when they are irradiated. This is possible because under illumination the number of charge carriers increases, decreasing the film resistance. However, TiO_2/AuNPs already has an order of magnitude lower film resistance in the dark than TiO_2, considering the higher conductivity of gold nanoparticles.

Furthermore, this resistance drops more strongly, since in this system the charge carriers are more facilitated by the presence of gold. Instead, it is possible to observe how the capacitance of the electric double layer (Table 4.2, 1st column) under irradiation tends to increase in an identical manner for both samples, since the amount of charges in the capacitor increases in an equal manner, due to titania layer, and is not influenced by the presence of the metal.

The major change under illumination for TiO_2/AuNPs can also be seen from the Bode plot (Figure 4.6 B), where the peak becomes very evident and moves to higher frequencies, indicating an increasingly favored process.

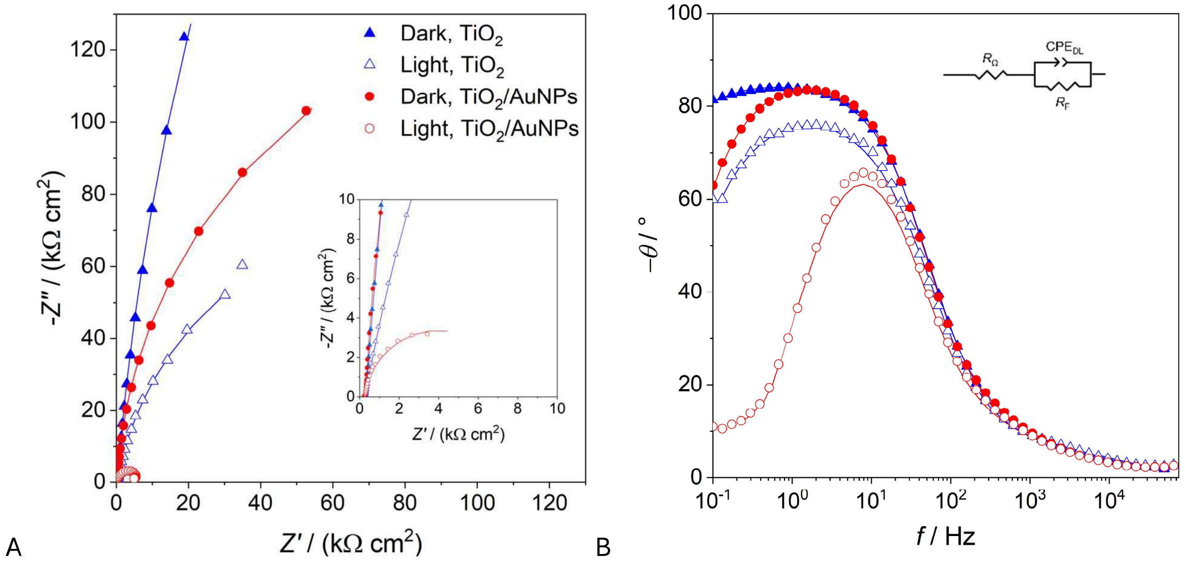

Figure 4.6 - Complex plane plots (A) and Bode phase plots (B) registered at + 0.1 V in 0.1 M $NaClO_4$ for TiO2 and TiO_2/AuNPs in the dark or under UV irradiation with 500 W UV lamp; magnification of complex plane plots and equivalent circuit are shown in insets

	CPE_{DL} / μF cm^{-2} s$^{\alpha-1}$		α_{DL}		R_F / kΩ cm^2	
	Background	Ciprofloxacin	Background	Ciprofloxacin	Background	Ciprofloxacin
TiO_2/ Dark	12.0	12.6	0.95	0.95	1560	1220
TiO_2 Light	17.8	17.8	0.89	0.89	174	162
TiO_2/AuNPs Dark	11.9	13.7	0.97	0.96	279	48.0
TiO_2/AuNPs Light	18.1	22.3	0.94	0.92	7.38	8.61

Table 4.2 - EIS parameters of TiO_2 and TiO_2/AuNPs with and without irradiation, in the absence or in the presence of ciprofloxacin 10^{-5} M in $NaClO_4$ 0.1 M.

The photocurrent tests carried out with the same illumination source employed for EIS (Figure 4.7 A) confirm the results obtained with EIS, showing a current about three times more intense for TiO_2/AuNPs compared to TiO_2, again showing the excellent conducting action performed by gold.

Moreover, the tests carried out with LEDs at lower power and different wavelengths (Figure 4.7 B) show the best results for TiO_2/AuNPs in comparison with TiO_2, confirming the responses obtained with a more powerful illumination source. The highest photocurrent is clearly obtained with the 395 nm LED, while the current is approximately halved for the 455 nm LED.

Considering all the results obtained from the photoelectrochemical characterization, TiO_2/AuNPs can therefore be defined as an excellent candidate for photo-electroanalytical measurements.

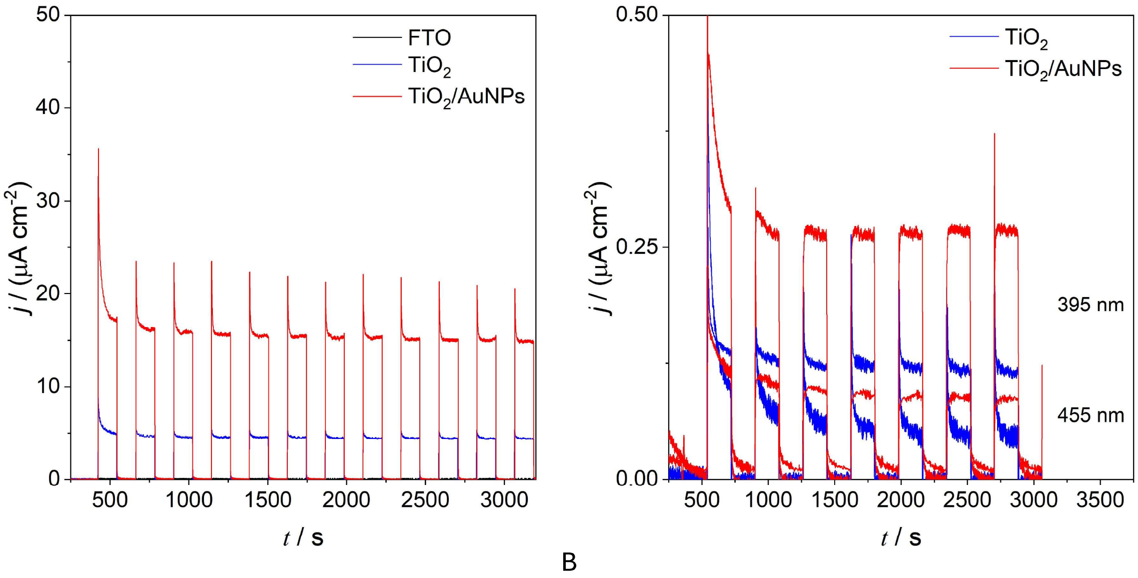

Figure 4.7 - Photocurrent measurements registered at + 0.1 V under intermittent irradiation with UV lamp (A) and with LEDs at 395 nm and 455 nm (B)

Electrochemical impedance spectroscopy was also recorded in the presence of an analyte molecule, ciprofloxacin (introduced in section 2.2.1), to fully understand the interaction that the molecule can have with the electrodes and with the light. All the samples maintain a trend of the complex plane plot (Figure 4.8 A) and of the Bode plot (Figure 4.8 B) very similar to the behavior recorded on the background, showing that it is the absence or the presence of irradiation that strongly influences the electrochemical performances. Moreover, the equivalent circuit (Figure 4.8 - inset) remains the same showed in Figure 4.6 (inset).

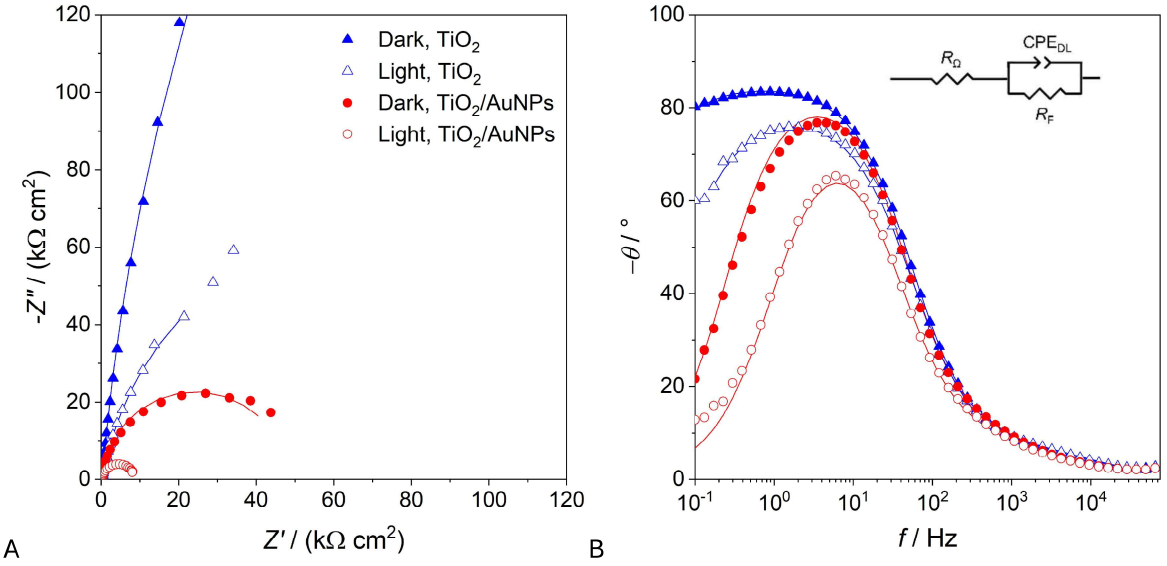

Figure 4.8 - Complex plane plots (A) and Bode phase plots (B) registered at + 0.1 V in 0.1 M $NaClO_4$ in the presence of 10^{-5} M ciprofloxacin for TiO_2 and TiO2/AuNPs in the dark or under UV irradiation with 500 W UV lamp; equivalent circuit is shown in inset

However, small variations in the graphs and fitting values can be observed especially for TiO_2/AuNPs in the presence of the target molecule. In fact, TiO_2 shows identical values of the elements of the equivalent circuit in the dark in the presence and in the absence of ciprofloxacin (Table 4.2), indicating that in the dark TiO_2 at the applied potential is not affected by the presence of the molecule. When this sample is irradiated, only a slight decrease in film strength can be observed, while the other parameters remain unchanged.

This demonstrates that light aids the determination of ciprofloxacin, as the film resistance decreases. This fact is also demonstrated by observing the values and behavior of TiO_2/AuNPs in the dark: the resistance of the film also decreases in this case, but much more markedly. This demonstrates that ciprofloxacin can also be determined in the dark, if the resistance of the film is lower, as in this last case.

Furthermore, for this sample a small increase in the capacitance of the electrical double layer can also be observed in the presence of ciprofloxacin, which therefore interacts with the electrode surface. When the sample is placed under irradiation there is then a further increase in this capacity, while the resistance remains constant, since it is already a very low resistance.

4.3 Ciprofloxacin detection

The previous results confirm the detection tests of ciprofloxacin obtained under irradiation in amperometry (Figure 4.9 A). First, dark tests yielded no results on both electrodes, as the resistances are too high and the applied potential too low for the ciprofloxacin reaction to occur. Under irradiation, on the other hand, an increase in the photocurrent is obtained with each addition of ciprofloxacin only for TiO_2/AuNPs, demonstrating that only the low resistance of the film obtained by combining gold nanoparticles with titanium dioxide can make the molecule detectable at such low potential. The calibration lines (Figure 4.9 B) confirm the trend observed in photocurrent, showing a relevant increase in the current for consecutive additions of ciprofloxacin only for TiO_2/AuNPs.

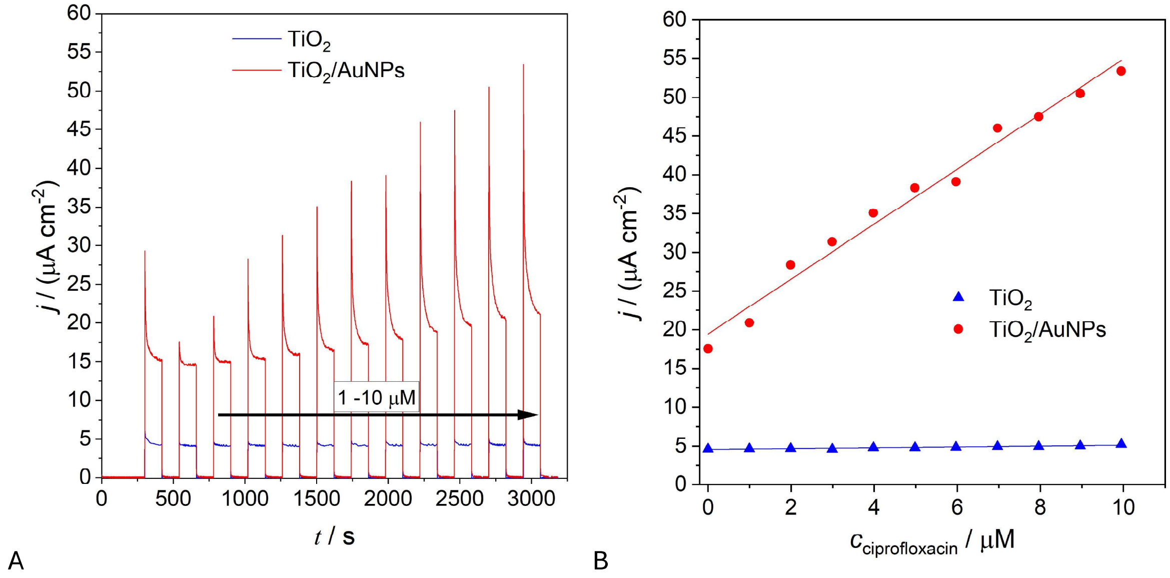

Figure 4.9 - Photocurrent measurements registered at + 0.1 V under intermittent irradiation with UV lamp for consecutive additions of ciprofloxacin (A) and correspondent calibration plot (B) for TiO$_2$ and TiO$_2$/AuNPs

To increase the applicability of the photo-electroanalytical technique, a less powerful but more manageable light was chosen: LED sources. Different wavelengths and powers were studied (395 nm, 455 nm and 530 nm) and the best signal was clearly obtained for the LED in the UV at maximum power, even if it is possible to obtain a good signal even at the medium wavelength. The irradiation from the conductive or non-conductive front does not alter the value of the generated photocurrent (Figure 4.10 A), while the distance of the source from the electrode is very important, since the generated photocurrent decreases if the distance increases (Figure 4.10 B), as expected. It is also important to note that ciprofloxacin does not absorb light and does not degrade due to irradiation at the selected wavelengths (Figure 4.10 C).

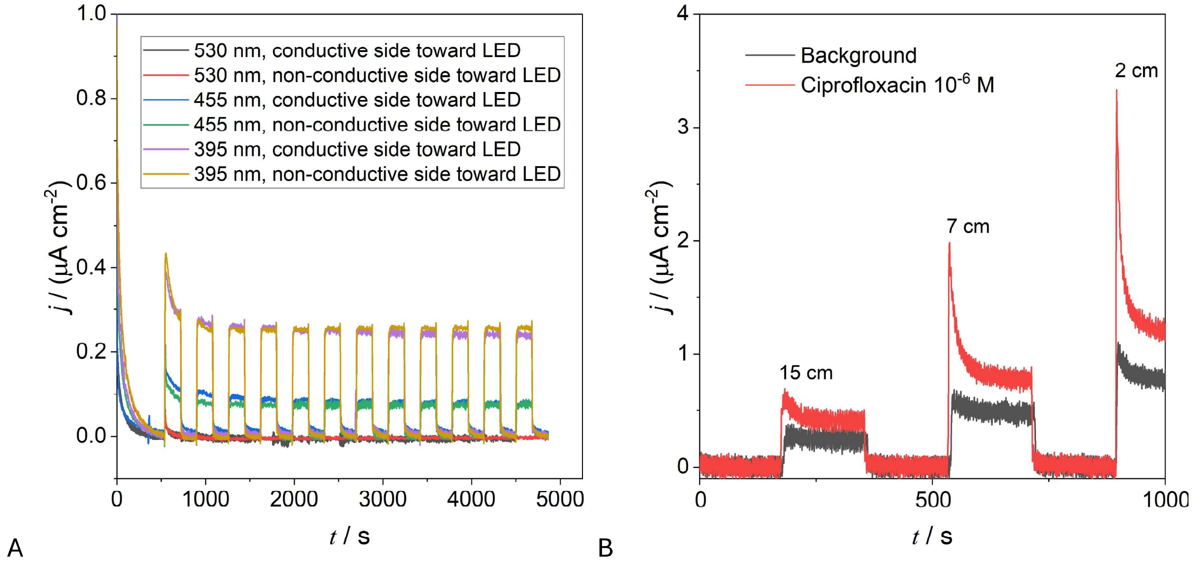

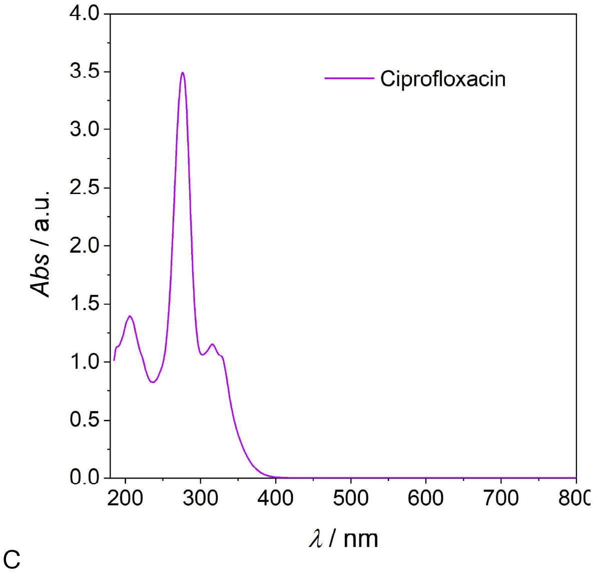

Figure 4.10 - (A) Effect of the electrode's orientation and distance from LED (B) on the obtained signal; UV-Vis spectra of Ciprofloxacin (C)

In Figure 4.11 A the photocurrent obtained under the best conditions is shown and the calibration line obtained several times and on different electrodes is shown in the inset. The analytical parameters are very good and in particular the sensitivity is 1.81 ± 0.04 (µA cm^{-2} µM^{-1}), the limits of detection and quantification (obtained with S/N=3 and S/N=10 respectively) are (0.32 ± 0.08) µM and (1.06 ± 0.08) µM, respectively. The precision of the method is very good with a low RSD % (< 5%) and the trueness is also excellent, with apparent recovery factors of 99.8 %.

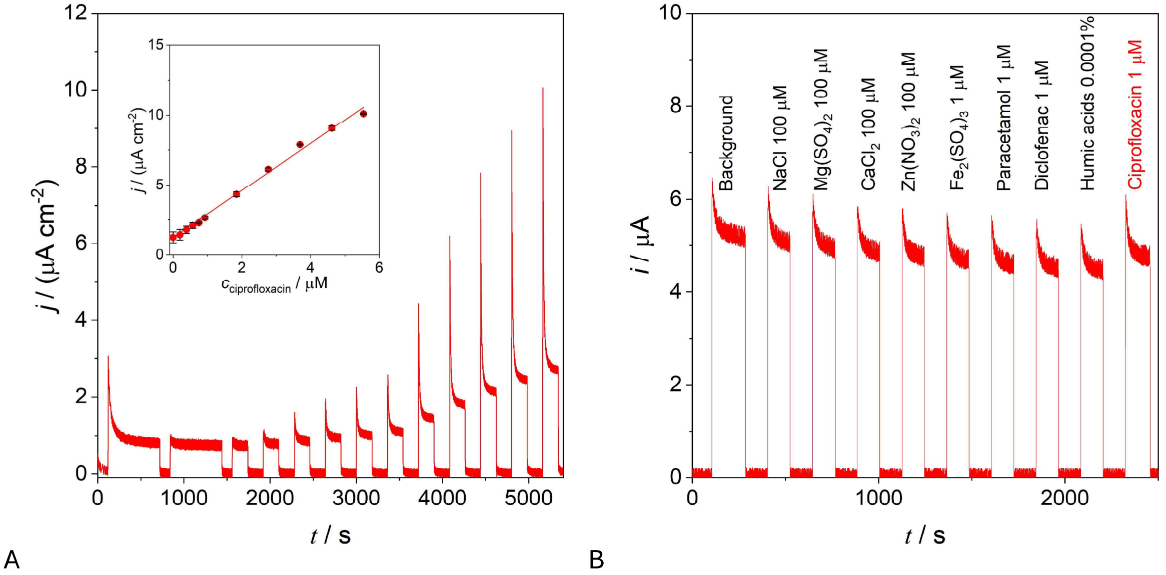

Figure 4.11 - Photocurrent measurements registered at + 0.1 V under intermittent irradiation with a LED at 395 nm for consecutive additions of ciprofloxacin (A) with the correspondent calibration plot in inset and (B) interference study for TiO$_2$/AuNPs

The study of the interferents has considered the possible inorganic and organic contaminants present in surface waters [45–47] where ciprofloxacin can be detected and, as can be seen from the photocurrents obtained under the same operating conditions of detection of the target molecule (Figure 4.11 B), no detectable interferences were registered.

From the comparison with the literature for the photoelectrochemical determination of ciprofloxacin, reported in Table 4.3, it emerges that the device presented here is the only one based on a heterojunction formed by nanoparticles of gold and titanium dioxide and above all on a signal-on type PEC obtained through a simple synthesis. Although the detection limits still have to be improved, it is important to underline that the robustness of the photoelectrode as well as the use of low power LEDs compared to other systems [45–49], paves the way for the construction of miniaturized systems that can be used for continuous and onsite analysis.

Table 4.3 - Comparison with other PEC devices for the detection of ciprofloxacin

Material	Irradiation	Potential	Signal Type	LOD	Range	Reference
AuNPs/ITO	350W Xe lamp	0.2V	Signal-off	0.08 nM	0.1 nM–10 μM	[45]
g-CN/BiOCl	150W Xe lamp	0V	Signal-off	0.6 nM	1.5 nM - 5.5 μM	[46]
Bi/BiOBr	150W Xe lamp	0V	Signal-off	16 nM	50 nM - 15 μM	[47]
Bi/BiOCl	150W Xe lamp		Signal-off	0.15 μM	0.5 μM - 30 μM	[48]
ND-g-CN/ITO	300W Xe lamp	0V	Signal-on	0.06 nM	0.18 nM – 57.61 nM	[49]
AuNPs/TiO_2	395 nm LED	0.1V	Signal-on	0.32 μM	0.2 μM – 5 μM	This sensor

4.4 Conclusions

A photoelectrode for photoelectrochemical analysis applications based on a titanium dioxide – gold nanoparticle heterojunction was obtained through a simple and reproducible synthesis. It was characterized by SEM, AFM, CV, and EIS with the presence of a probe molecule and compared with single systems, showing superior electrochemical performances.

Subsequently, it was photoelectrochemically characterized by EIS and photocurrent measurements, showing better results than titanium dioxide alone. The presence of metal nanoparticles has in fact proved to be essential to limit the recombination of the photogenerated charges, showing a higher photocurrent and a decreased resistance of the film. In the presence of ciprofloxacin, it has been shown that exclusively the heterojunction allows its detection even using low-power and visible LED light sources, thanks to the low film resistance and to the presence of nanoparticles with localized surface plasmon resonance properties, obtaining good analytical performances and good resistance to interferences. Given the great robustness of the device and the use of more accessible light sources, the application of these systems in integrated circuits for online and onsite analysis is expected in the future.

5 Metal structure optimization

5.1 Wet methods

As the presence of gold nanoparticles proved to play a crucial role in the electrodes' performances, it became clear that a better way to deposit them was necessary. The main goal was to be able to increase its quantity to study how it would affect the TiO_2 layer, and on the other hand it was necessary to obtain a reliable and reproducible synthetic procedure.

The first tests were conducted by modifying the silanes deposition procedure. A new procedure was developed that aimed to use a DIY reactor and an oven to deposit the linkers using physical vapor deposition on the FTO glass slide.

This unfortunately leads to unconclusive results: the amount of linkers deposited could not be easily quantified, but the layer clearly presented a lack of uniformity, possibly due to the difficulty of controlling key environmental parameters such as temperature, humidity and air flow. Furthermore, a hydrophobic layer formed on the surface, making it impossible to add the AuNPs via drop casting.

A different procedure was investigated, namely gold electrodeposition from a $HAuCl_4$ solution. As reported in the literature[85,86] and described in Chapter 10.4, gold could be effectively deposited by briefly applying a positive bias to the cell (+ 1.1 V vs SCE for 5s) and subsequently reduce the gold precursor (-0.1 V vs SCE, with time between 15 s and 60s depending on the desired concentration).

Figure 5.1 compares the FTO/AuNPs electrodes obtained using the "classical" silane-based method and the new electrochemical synthesis. It is clear that the latter allowed to deposit a greater amount of gold, as the coloration is way more intense. By monitoring the charge during the electrodeposition it was possible to calculate the rate of gold deposition to be 3.5 ng cm^{-2} s^{-1}.

A change of colour could be observed for the electrodeposited samples after few hours from the electrodeposition, from blue to pink, wich indicated a structural change of the gold structures, thus stability issues. This change was also not uniform.

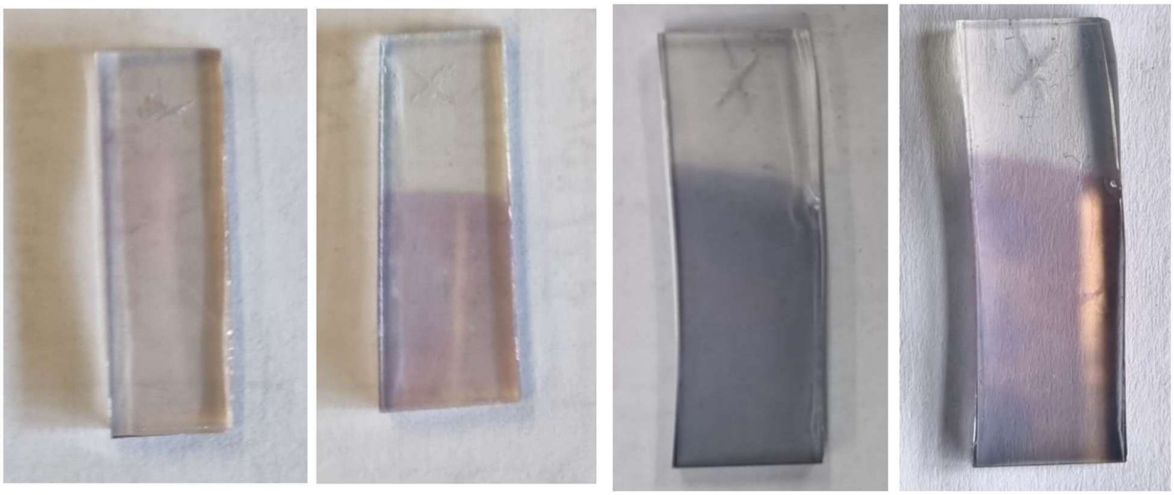

Figure 5.1 - (A) FTO electrode functionalized with gold nanoparticles using silanes as linkers (B) FTO covered with electrodeposited gold (C) freshly deposited gold on FTO and (D) same electrode after 48 hours

One hypotesis is that the metastable gold structures could migrate on the surface. This process could also be affected by the presence of perchlorate crystals, that was used as supporting electrolyte during the electrodeposition. A possible solution was a cleaning of the surface by dipping the electrode in water. Unfortunately, as shown in Figure 5.2 A, this lead to a loss of gold that could not be reliably quantified, highlighting at the same time the need for a protective structure, like the TiO_2 layer, on the gold structures.

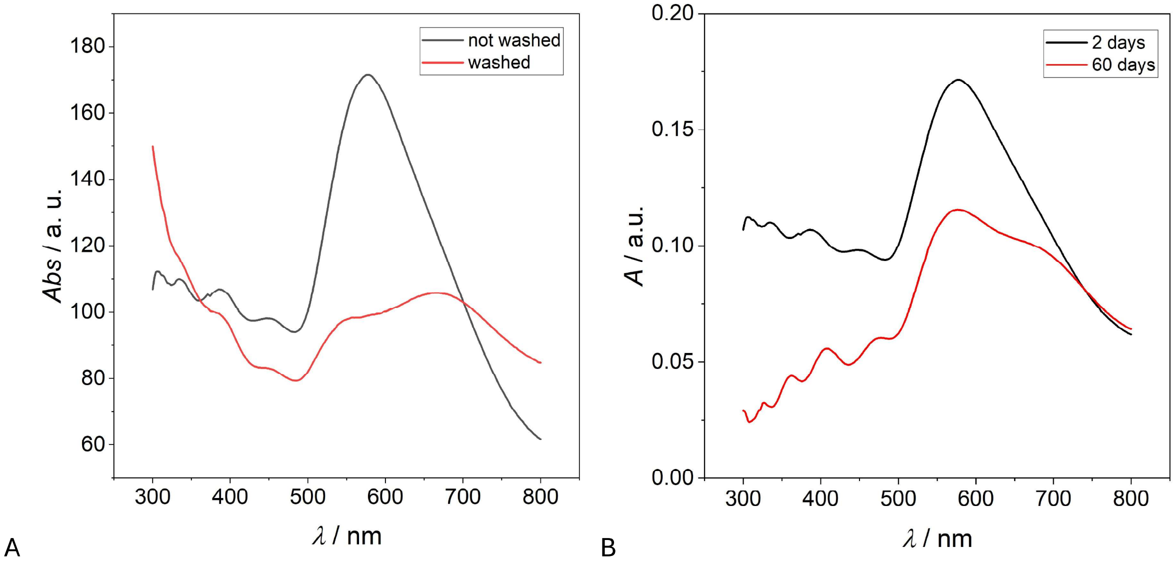

Figure 5.2 - UV-Vis spectra of (A) FTO electrodes washed and non-washed after Au electrodeposition and (B) non-washed FTO/Au electrodes at different ageing time

SEM images recorded for a non-washed electrode clearly showed that the surface is not uniform, as gold can be present either as distributed nanoparticles or larger clusters.

By increasing the magnification and using EDX point-measurement, the morphology of the surface can be further investigated. As shown inFigure 5.3, some gold is present as small 1 µm clusters, some is present as smaller structure that could not be observed due to the instrument limitation, and some even larger exagonal structures can be observed.

Overall, the use of the electrodeposition was considered less than ideal because it did not allowed to obtain uniform deposition, and the need for further washing of the electrode removed the possibility to accurately monitor the amunt of deposited gold.

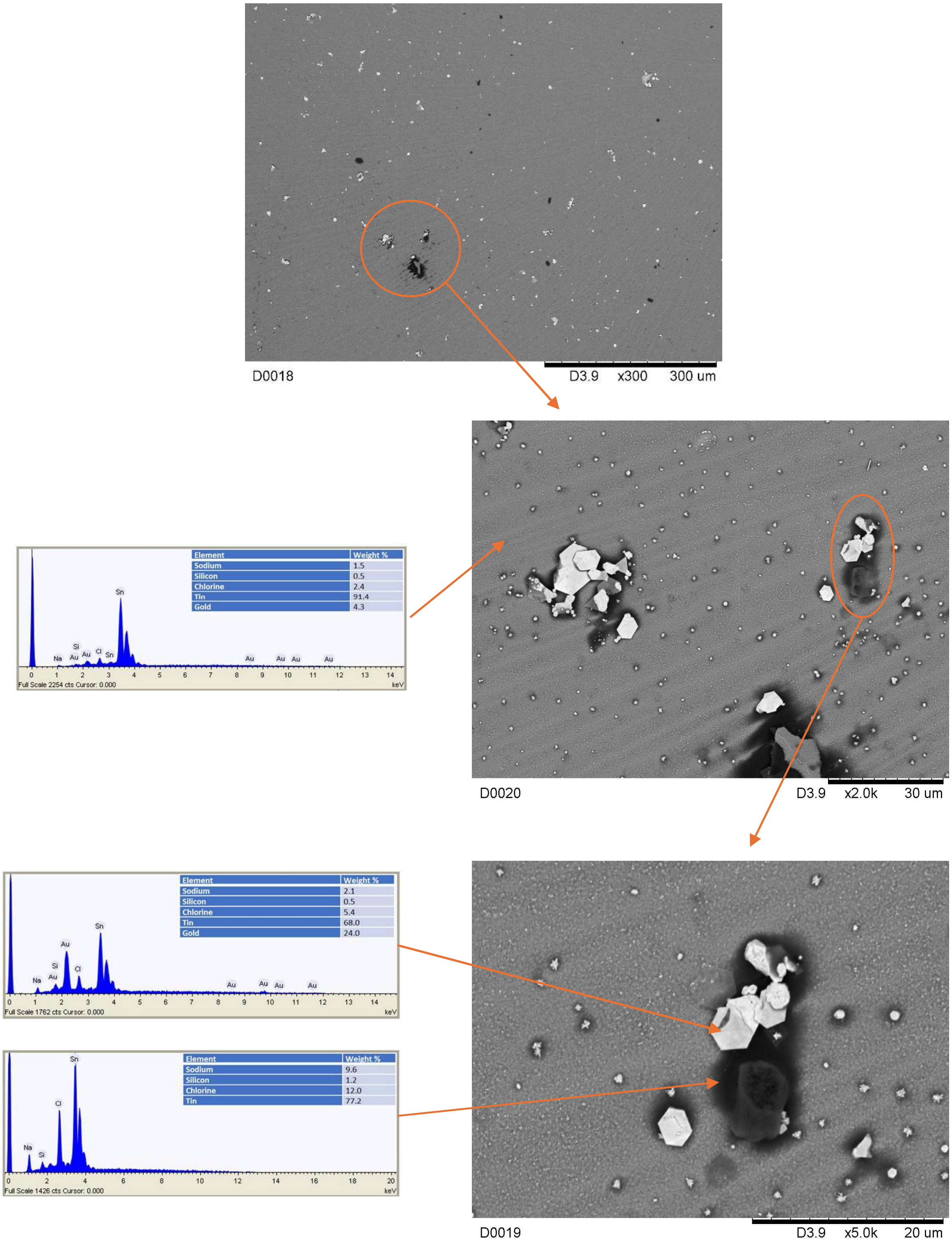

Element	Weight %
Sodium	1.5
Silicon	0.5
Chlorine	2.4
Tin	91.4
Gold	4.3

Element	Weight %
Sodium	2.1
Silicon	0.5
Chlorine	5.4
Tin	68.0
Gold	24.0

Element	Weight %
Sodium	9.6
Silicon	1.2
Chlorine	12.0
Tin	77.2

Figure 5.3 - SEM-EDX recorded with a FTO/Au electrode at different magnification

5.2 Dewetting preliminary tests

As wet chemical methods proved to be ineffective, solid state dewetting was used for the preparation of metal nanoparticles, exploiting the knowledge provided by Photocatalytic Synthesis Group (PCS group) of the University of Twente.

The first tests with dewetted thin films were conducted using platinum deposited on FTO. Such metal was used by the group to investigate hydrogen evolution and presents peculiar advantages, such as the ability to easily and reliably quantify the electrochemically active surface area of the catalyst. As shown in Figure 5.4 A, a clear difference could be obtained when comparing a Pt film and the corresponding dewetted structures.

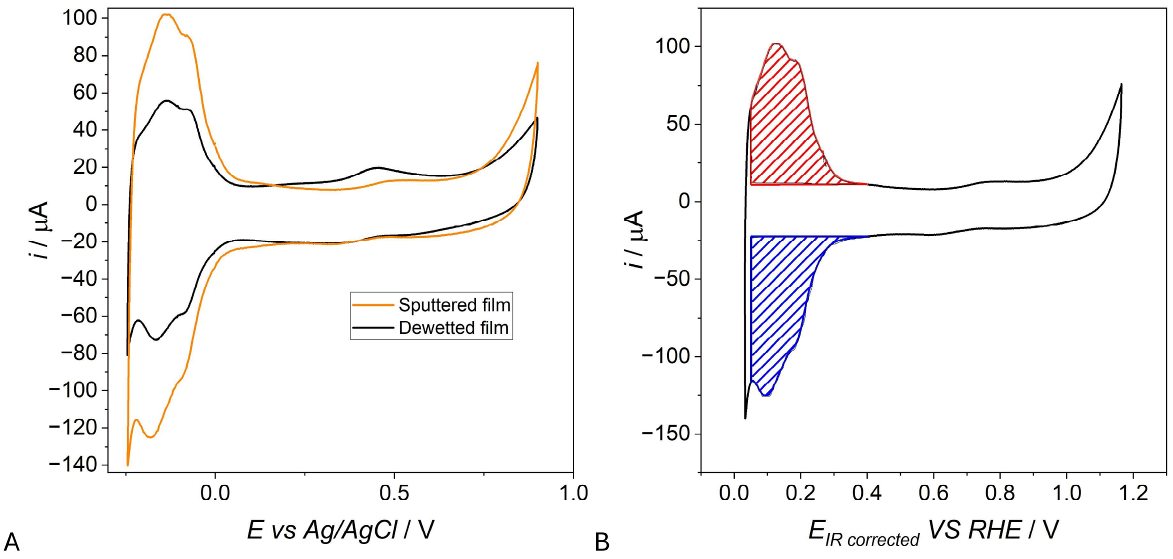

Figure 5.4 - (A) CV recorded in $HClO_4$ 0.1 M with Pt-based electrodes and (B) area integrated for the ECSA evaluation

This difference can be explained with a reduction of the surface area, as part of the metal initially present on the surface of the film forms the bulk of the nanoparticle, were it cannot interact with the solution.

The area reduction can be estimated by integrating the Hydrogen Under Potential Deposition (HUPD) regions of the electrodes, as shown in Figure 5.4 B, and converting them to a value of area using Equation 5.1. Assuming the geometric area equal for all the samples (3.14*0.3 cm *0.3 cm = 0.2826 cm^2). Rugosity was also calculated according to Equation 5.2.

Equation 5.1

$$ECSA = \frac{Integrated\ Area\ (A\ V)}{scan\ rate\ (V\ s^{-1})}\ x\ \frac{1000000}{210}$$

Equation 5.2

$$Rugosity = \frac{ECSA\ (cm^2)}{Geometric\ Area\ (cm^2)}$$

The obtained results are summarized in Table 5.1:

		Integrated Value (mA V)	ECSA (cm^2)	Geometric Area (cm^2)	Rugosity	Reduction (%)
Pt FILM	Absorption	0.01539	0.732857143	0.2826	2.593267	-
	Desorption	0.01513	0.72047619	0.2826	2.549456	-
Pt NPs	Absorption	0.00782	0.372380952	0.2826	1.317696	-49.1878
	Desorption	0.00794	0.378095238	0.2826	1.337917	-47.5215

Table 5.1- Area reduction of Pt samples upon dewetting

A decrease of nearly 50% is observed, similar to what is reported in the literature.[20]

Repeating the dewetting with different film thickness, it is possible to observe that while the morphology is clearly different from that of a film, the obtained nanoparticles are not isolated spheres but resemble finger-like structures (Figure 5.5).

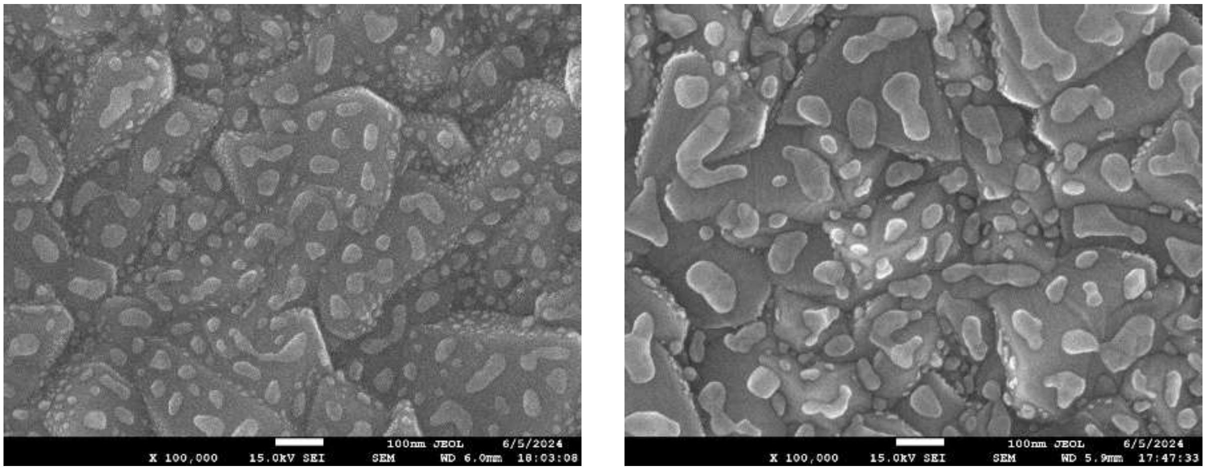

Figure 5.5 - SEM images of dewetted 2.5 nm Pt film (left) and 5 nm Pt film (right)

Although platinum is a widely used electrocatalyst, known especially for its activity in H_2 evolution, gold presents some advantages compared to platinum: its lower melting points (1064°C for Au versus 1772°C for Pt) is closer to the temperature used in the dewetting process of 500°C. Furthermore, gold presents a more inert surface. The formation of chemical bonds on the metal, like surface oxide, can reduce the atom mobility of the metal ions and negatively affects the dewetting. Lastly, the presence of a LSPR peak of gold nanoparticles in the visible regions allowed to assess the dewetting via fast and non-destructive methods, like UV-Vis spectroscopy.

From a practical point of view, the deposition of gold using sputtering technique can be performed using direct current instead of alternate current, which makes the procedure easier.

The use of platinum as a material for the synthesis of nanoparticles has allowed us to leverage the expertise of the PCS group at the University of Twente, where these tests were conducted, and demonstrate that the controlled preparation of metallic nanoparticles is indeed possible.

However, platinum presents some challenges compared to other metals. In particular, its high melting temperature makes it more difficult to achieve dewetting with very thick layers. Furthermore, platinum can form surface oxide layers. These layers reduce the mobility of the atoms and make the formation of nanoparticles more difficult. The use of gold, which has a lower melting temperature and less tendency to oxidize, solves these problems.

An ad-hoc procedure was developed to simulate the electrode wear by cycling in ferrocyanide solution, which, combined with the application of anodic potentials,[87] is known in the literature to facilitate gold dissolution,[88] and was used to compare the stability of the electrodes prepared with gold film of different thickness and nanoparticles of different dimensions.

As for the sensing performances, H_2O_2 was selected as probe molecule. H_2O_2 was not detected on the bare FTO support, thus any difference between the analyzed samples was only due to the different gold deposition.[52]

5.3 Electrodes Preparation and Characterization

The FTO-coated glass electrodes, prepared as shown in Figure 5.6 and discussed in detail in Section 10.5, were weighed with an analytical balance to quantify the loading of gold. The sputtered mass is linear with the deposition time (and thus film thickness), with a slope of (0.00164 ± 0.00004) $mg_{gold}\ cm^{-2}_{area}\ nm^{-1}_{thickness}$. (Figure 5.7 A) The linear increase of gold loading was also observed using EDX analysis (Figure 5.7 B).

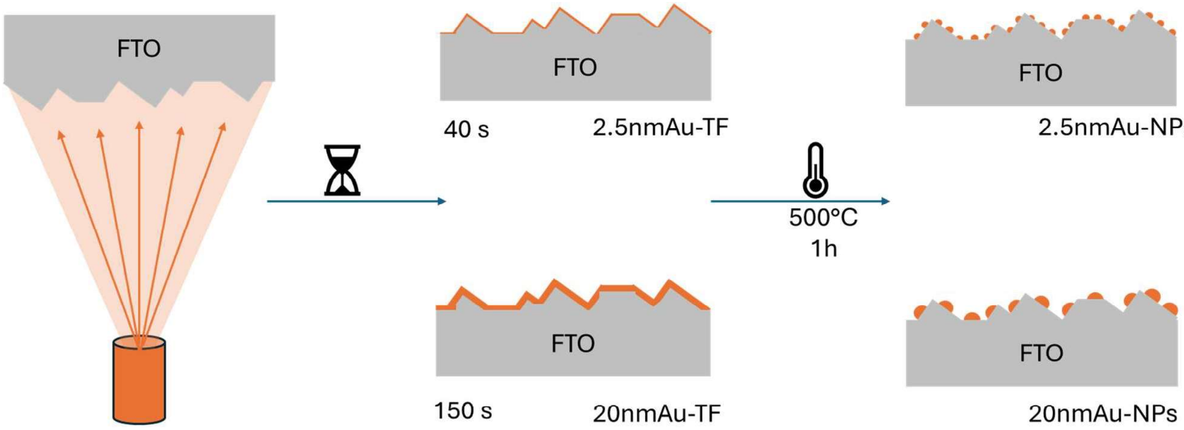

Figure 5.6 - Preparation of the samples: Gold was sputtered on FTO-coated glass slides, obtaining thin films of various thickness X (XnmAu-TF), proportional to the sputtering time. Upon heating, dewetting of the film is achieved, producing nanoparticles with dimensions related to the initial film thickness X (XnmAu-NPs) and partially exposing the underlying FTO surface

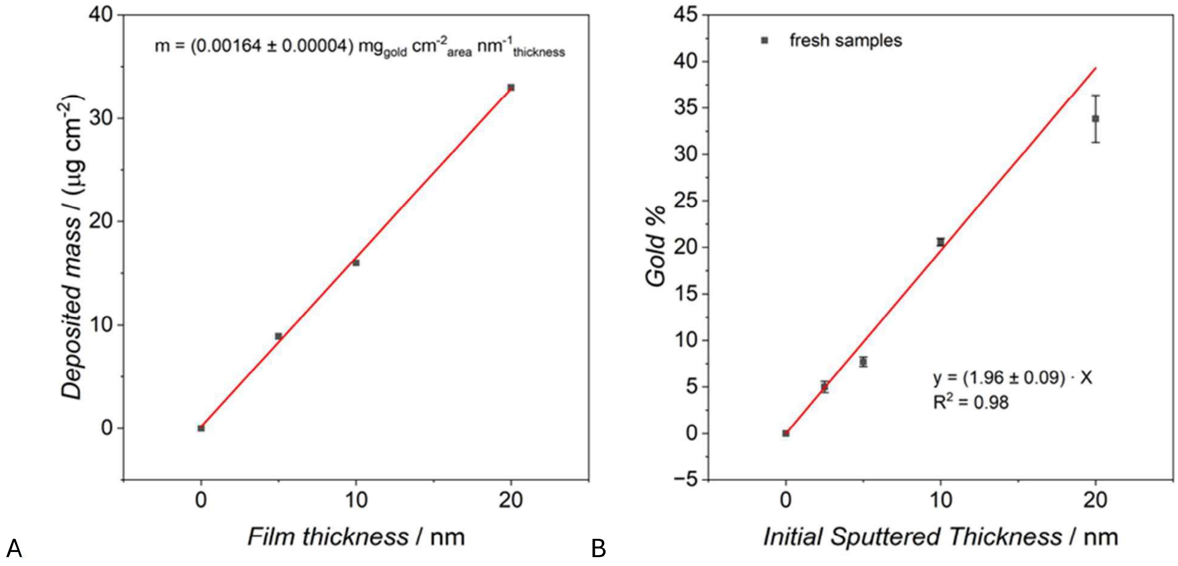

Figure 5.7 - (A) Relation between sputtered mass and deposition time and (B) EDX analysis of the prepared samples

The dewetted samples were characterized using scanning electron microscopy, as reported in Figure 5.8 A with the same magnification, observing a complete dewetting of the sputtered film to form nanoparticles. A pristine FTO surface is also reported as comparison, showing the characteristic polycrystallinity and roughness of the electrode surface. The particle size, as shown in Figure 5.8 B and Figure 5.8 C, is closely related to the initial sputtered film thickness.

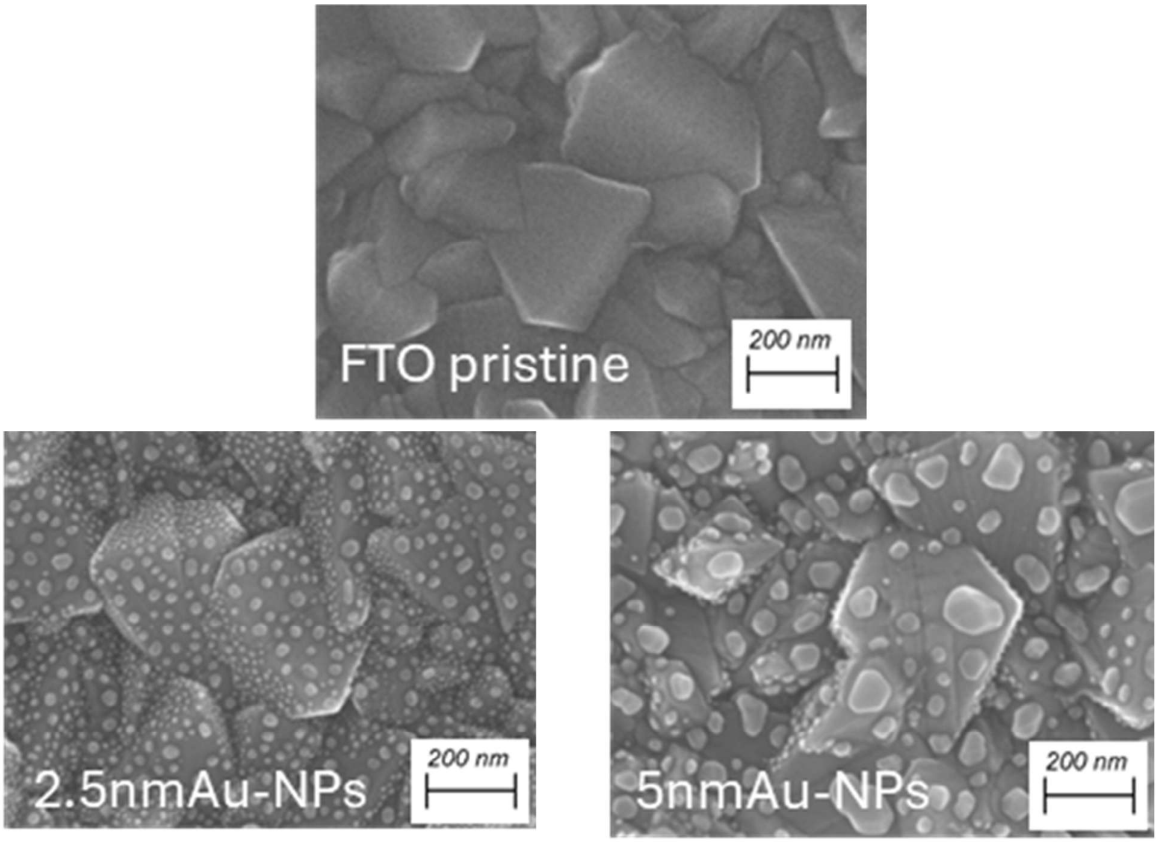

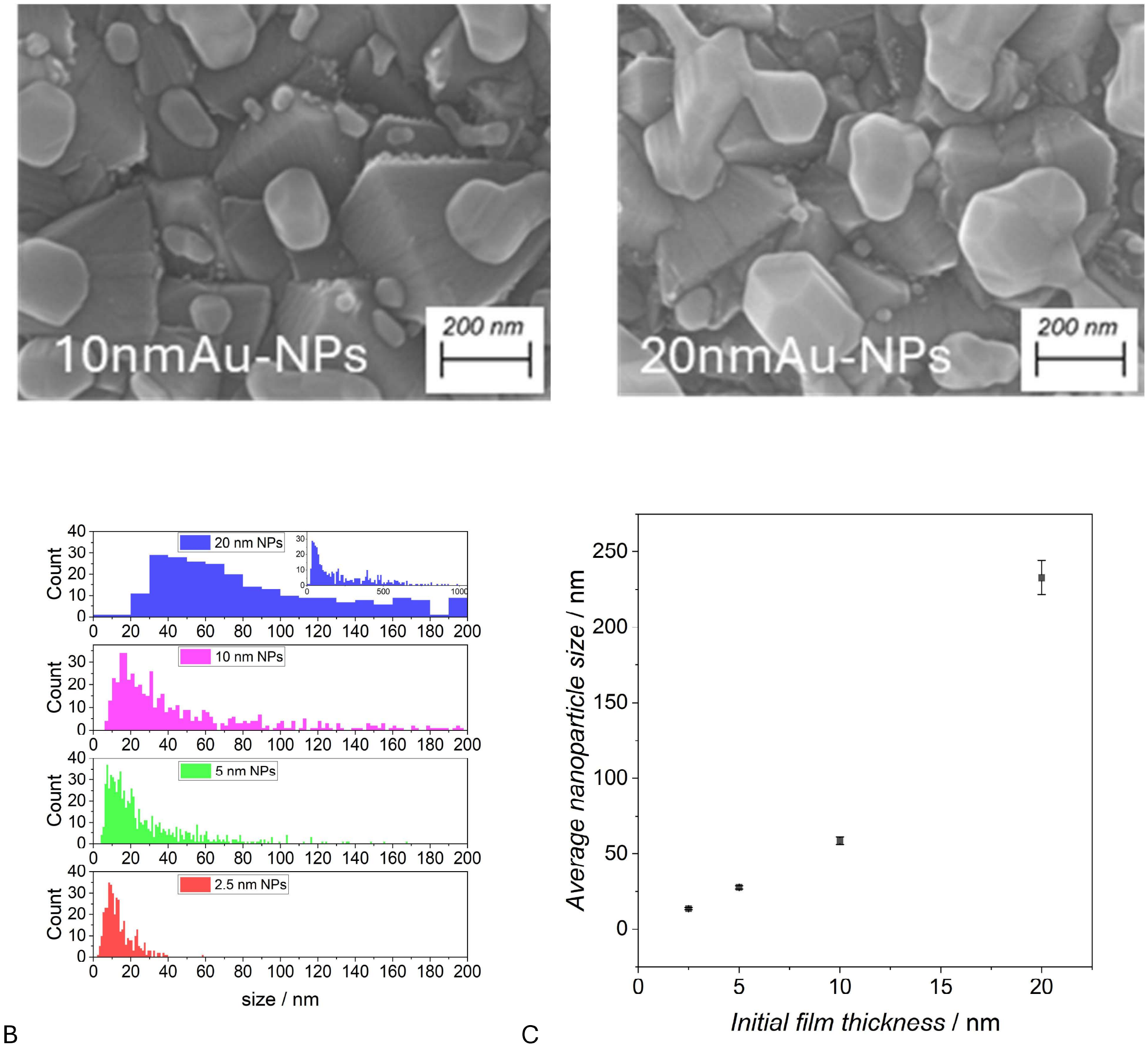

Figure 5.8 - SEM images of annealed (dewetted) films of 2.5, 5, 0 and 20 nm of gold on FTO (A), particles size distribution of the obtained nanoparticles (B) relation between initial film thickness and nanoparticle size (C)

The desired film nominal thickness was obtained from the calibrated Au sputter rate under the conditions reported in Section 10.5 by tuning the sputter-deposition time. Particles of (13.6 ± 0.7), (28 ± 1), (59 ± 2), (233 ± 11) nm are obtained from 2.5, 5 ,10 and 20 nm-thick films, respectively. It can also be noted that while the smaller nanoparticles maintain a good circularity, the larger ones tend to have a more elongated shape. The evaluation of the nanoparticles' circularity, reported in Figure 5.9, is in line with the observations reported in the literature.[23]

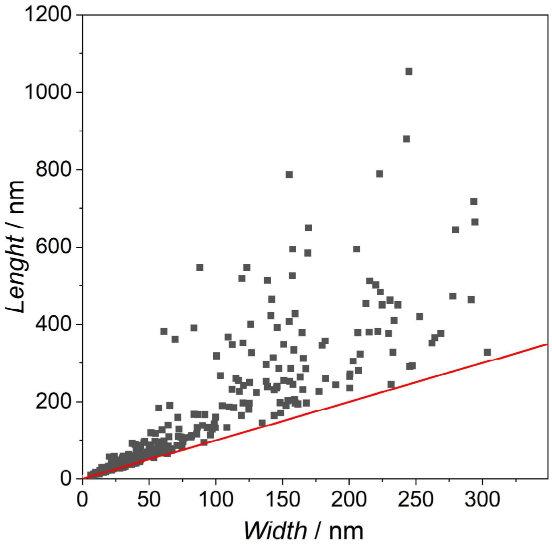

Figure 5.9 - Evaluation of the circularity of the nanoparticles. Red line represents perfect circularity

The visual color of the samples changed significantly both by increasing the gold loading and upon annealing, suggesting the formation of specific plasmon resonance peaks in the visible light region (Figure 5.10 A). UV-vis spectra of the samples show the presence of such characteristic LSPR peak related to the size of gold nanoparticles. A single peak located at 559 nm and 606 nm is obtained for the nanoparticles derived from 2.5 and 5 nm films. Wider peaks, due to a broader particles size distribution, are observed at higher wavelength for the nanoparticles derived from thicker films (Figure 5.10 B). On the other hand, UV-vis spectra recorded before the annealing procedure are significantly different, only showing peaks above 800 nm due to the thickness of the thin films (Figure 5.10 C).[89]

2.5 nm film		2.5 nm dewetted
5 nm film		5 nm dewetted
10 nm film		10 nm dewetted
20 nm film		20 nm dewetted

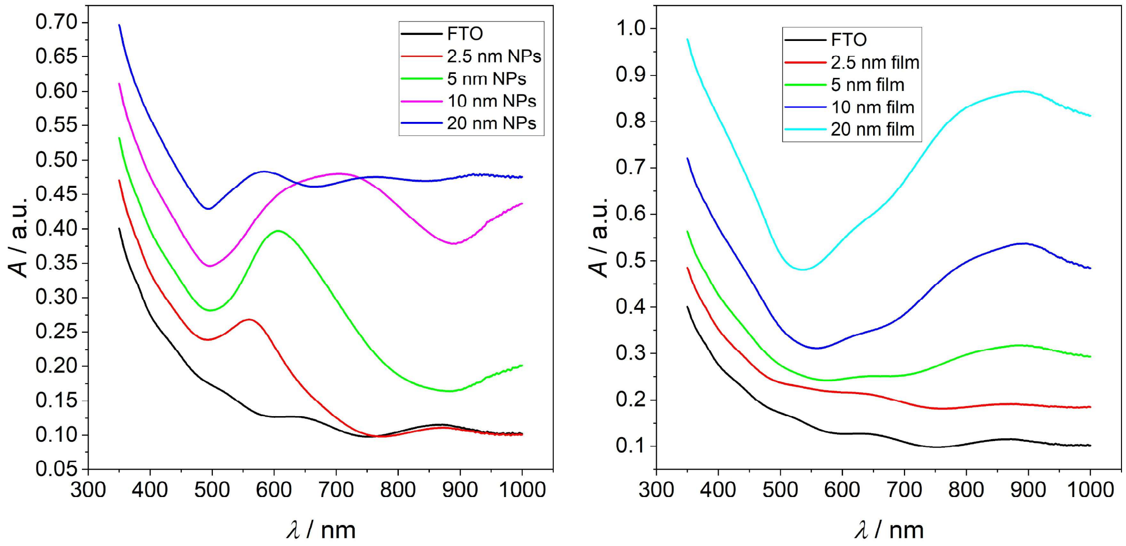

Figure 5.10 - (A) Image of the obtained electrodes, UV spectra of obtained (B) nanoparticles and (C) films

The electrodes were also characterized using electrochemical techniques. In particular, to understand how different Au morphologies affect electrochemical behavior, the sensing performance of the smallest (2.5nmAu-NP) and biggest nanoparticles (20nmAu-NP) were compared. A thin film electrode (20nmAu-TF) is also included in the comparison as bulk gold electrode (where the FTO substrate is not surface exposed). This choice was made to highlight the different behavior of the electrodes and reduce the influences of the experimental errors, whose effect would be important if testing similar samples.

CVs recorded in $NaClO_4$ 0.1 M show the characteristic features of gold: between + 0.2 V and 0.8 V (*vs*. Ag|AgCl), an oxide layer is formed on the gold surface. On the reverse scan, at +0.15 V, the oxide layer is reduced to metallic gold. In the case of gold, the quantification of the surface area was carried out by integrating the gold reduction peak located at + 0.15 V vs Ag/AgCl, as shown in Figure 5.11 A for a 2.5nmAu-NP electrode. The area of the peaks changed between different electrodes, as reported in Figure 5.11 B. The decrease of the metal surface area upon annealing is a process already described in the literature.[20]

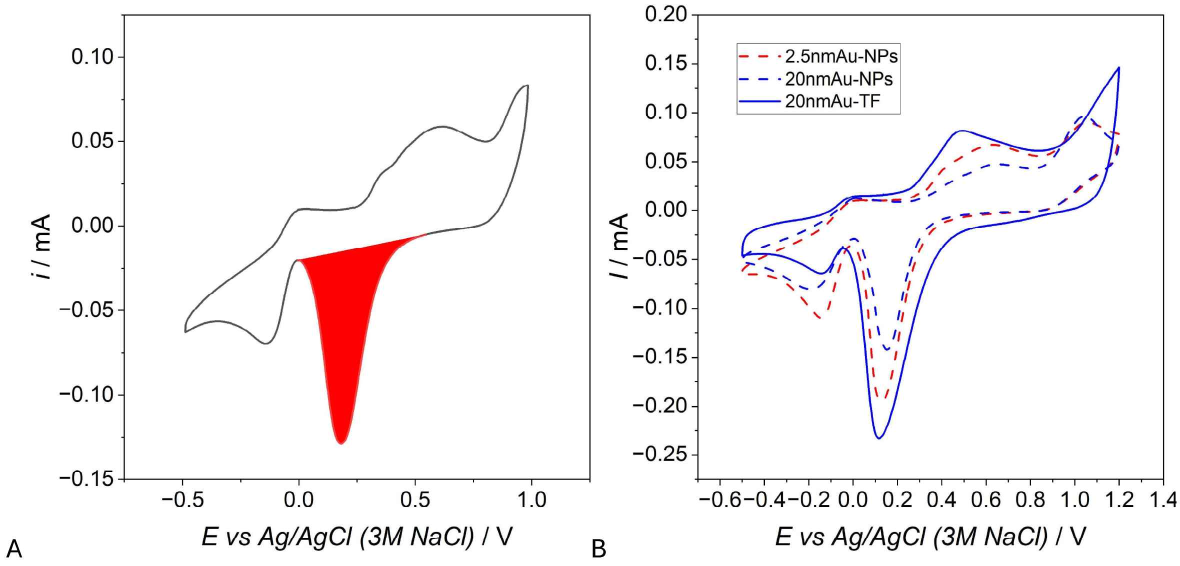

Figure 5.11 - (A) CV recorded in NaClO4 O.1 M with a FTO/Au NPS electrode. The highlighted area is integrated to calculate ECSA. (B) comparison of CVs of different electrodes

The obtained value of peak area was converted to ECSA (Electrochemical Active Surface Area) value using Equation 5.3 where A is the integrated area of the reduction peak in mA V, *v* is the scan rate in V s^{-1} and 390 µC cm^{-2} is the charge required for the desorption of the adsorbed oxygen monolayer as reported in the literature.[90] Surface roughness (R_f) was also calculates according to Equation 5.4, by dividing the ECSA by the geometric area of the electrode. The results are reported in Table 5.2. As expected, the surface area is larger for the film. After the annealing process, part of the gold will form the bulk of the particle, no longer being able to take part in the surface electrochemical processes, and this will cause a decrease of ECSA. This phenomenon is expected, as the agglomeration of the film is driven by minimization of the surface area, and widely discussed in the literature.[20,21] The area reduction is proportional to the volume of the nanoparticles.

Equation 5.3 - ECSA determination $ECSA / cm^2 = \frac{(A/v) \times 1000}{390}$

Equation 5.4 - Surface roughness determination $Rf = ECSA / A_{geom}$

Table 5.2 - Values of charge obtained via cyclic voltammetry and corresponding ECSA and R_f (roughness) values for different tested electrodes..

Sample	Charge / µC	ECSA / cm^2	Rf
2.5nmAu - NPs	284 ± 12	0.74 ± 0.03	2.6 ± 0.1
20nmAu - NPs	202 ± 21	0.53 ± 0.05	1.9 ± 0.2
20nmAu - TF	458 ± 29	1.19 ± 0.07	4.2 ±0.3

5.4 Electrode Stability

An *ad-hoc* procedure was developed to test selected electrodes and evaluate their stability by cycling in $K_4[Fe(CN)_6]$, as described in Section 10.8, to accelerate the electrodes' degradation processes. In addition to the previously selected nanoparticle-modified electrodes, films with the same gold loadings, and bare FTO electrodes, were tested for the sake of comparison (2.5nmAU-TF, 20nmAu-TF, and FTO). Bare FTO electrodes were also tested, showing no significant change before and after the test

(Figure 5.12). The anodic peak at + 0.3 V and the cathodic one at -0.1V correspond to the redox processes of the iron probe.

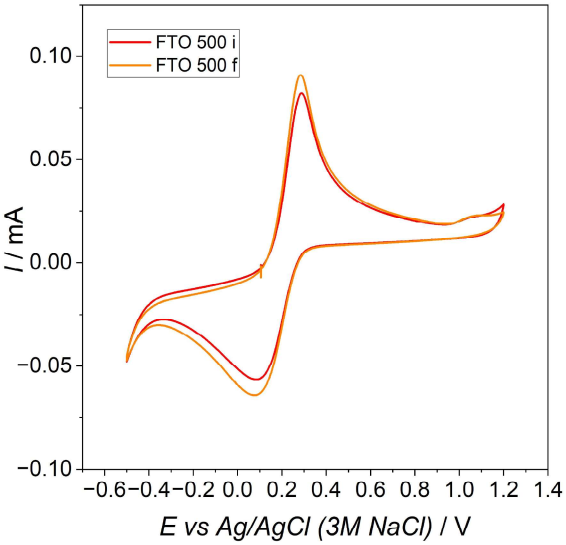

Figure 5.12 - FTO electrode tested with $K_4[Fe(CN)_6]$ 1 mM

By comparing the CVs recorded before and after the stability test for a gold-modified FTO glass slide, a clear change can be observed. In particular, as shown in Figure 5.13 A, by comparing the large nanoparticles (20nmAu-NPs) and the smaller ones (2.5nmAu-NPs), it can be observed how the nanoparticles with larger dimensions maintain a similar CV shape after the tests, while the performances of the smallest nanoparticles drastically worsen, as can be observed by the reduction of the anodic peak at + 1.3V. A similar test was conducted with gold films (Figure 5.13 B). In this case, the 20 nm film appears more stable than the 2.5 nm film. This was expected, considering that thin metal films are inherently unstable and prone to morphological changes.

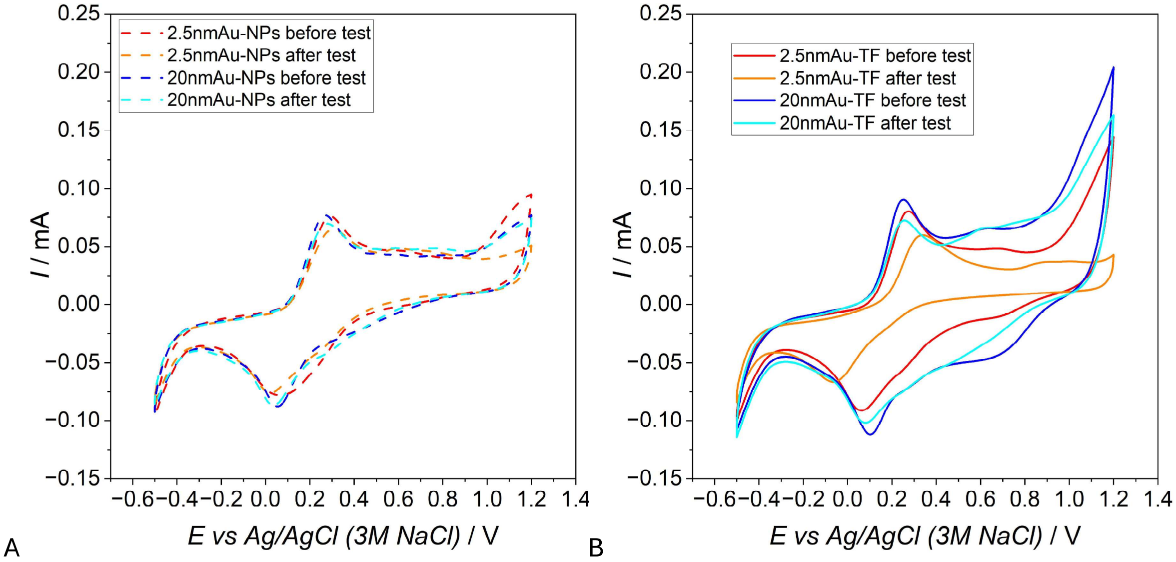

Figure 5.13 - CV of FTO/AuNPs (A) and FTO/Au FILMS (B) electrodes before and after cycling in $K_4[Fe(CN)_6]$ 1 mM

The same observations were also confirmed using EIS. Nyquist and Bode phase plots could both be used for the qualitative description of the systems, but the small changes could be more easily distinguished in the latter.

An example of the obtained graph is reported in Figure 5.14. Bare FTO and a gold film (20nmAu-TF) are shown as benchmarks, representing the situations where the FTO substrate is either completely exposed or completely covered. As-prepared nanoparticles (20nmAu-NPs) have an intermediate behavior between that of FTO and the gold film, which is expected as only part of the surface is covered by gold, and the FTO support is exposed. After testing, the charge transfer resistance of the nanoparticle electrode increases significantly.

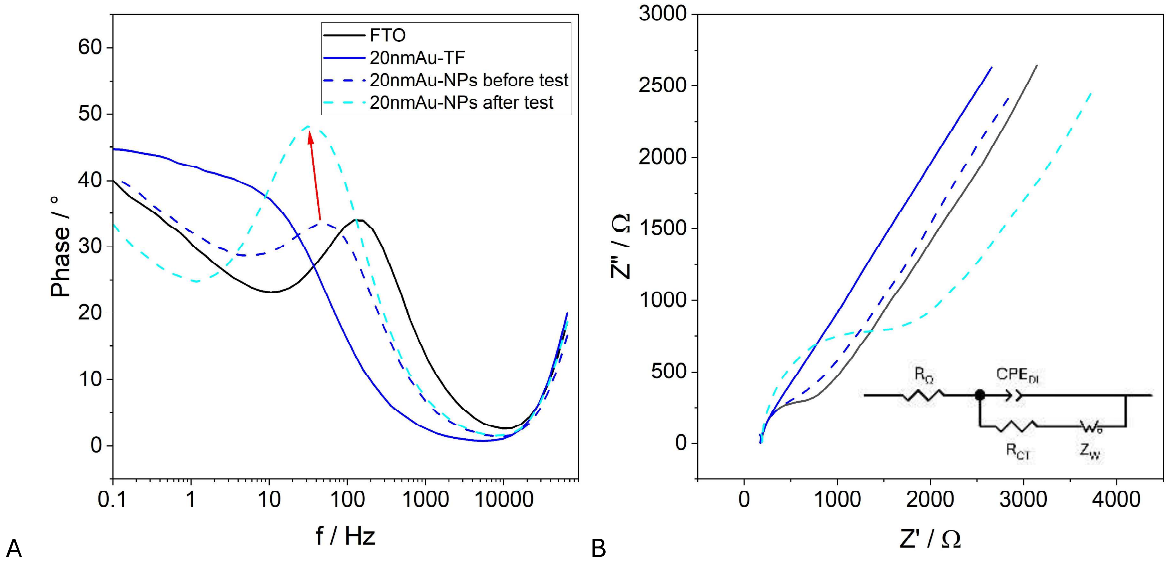

Figure 5.14 - Typical EIS response of the tested electrodes (A) Bode and (B) Nyquist plots. The corresponding equivalent circuit is reported as inset

All the obtained curves were fitted with ZView using the equivalent circuit in Figure 5.13 B where:

- R_Ω represents the resistance of the electrochemical cell;
- CPE_{DL} (constant phase element) represents the double layer capacitance
- R_{CT} is the charge transfer resistance
- Z_W (Warburg element) is related to the mass transfer

The resistance of the system R_Ω slightly decreases for FTO, probably due to cleaning of the surface that happens upon cycling, and remains almost constant for all the other samples. (Figure 5.15).

In the following graphs, for each sample (x asis), the bar on the left refers to the initial condition and the one on the right to the condition after cycling in $K_4[Fe(CN)_6]$ 1 mM. The error bars are obtained from the fitting function.

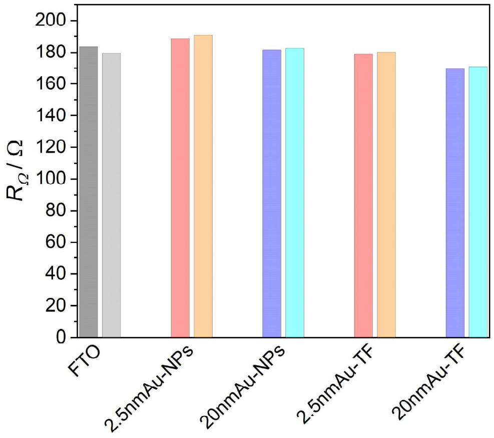

Figure 5.15 - R_Ω values

The constant phase element can be modelled as CPE = $[(Ci\omega)^{\alpha}]^{-1}$, were the value of α is equal to 1 in the case of a pure capacitor, or between 0.5 and 1 if the surface is not uniform.[91] α_{DL} increases for all the samples after the electrochemical tests in $K_4[Fe(CN)_6]$. This indicates that the electrodes get closer to a pure capacitor possibly due to a change of surface morphology that leads to more uniformity. The double layer capacitance value (CPE_{DL}) decreases for the FTO/Au samples, while it remains almost the same for FTO as its surface is not affected by the CVs. Before the tests, the samples with gold nanoparticles present capacitance values between those of FTO and the gold thin film. This phenomenon ca be related to a change in Au coverage and surface area, i.e., the Au ECSA decreases upon dewetting and exposes the underlying FTO surface. After the test, the values decrease drastically for the small nanoparticles and the thinner film, indicating that the surface get closer to that of FTO. This can be explained with a loss of gold that happens upon cycling. The change for the 2.5 nm film is much more pronounced, suggesting that for samples with the same gold loading (in terms of mass per unit surface), the nanoparticles are more stable than the film. (Figure 5.16 A, B)

A possible explanation is that the thermal treatment makes the NPs strongly attached to the FTO, with a relatively large FTO/AuNPs interfacial area.[20] Furthermore, as-deposited thin films have a larger surface to volume ratio and volumetric defect density compared to dewetted NPs, which makes the films more prone to electrochemical instability and thus less stable than dewetted NPs.

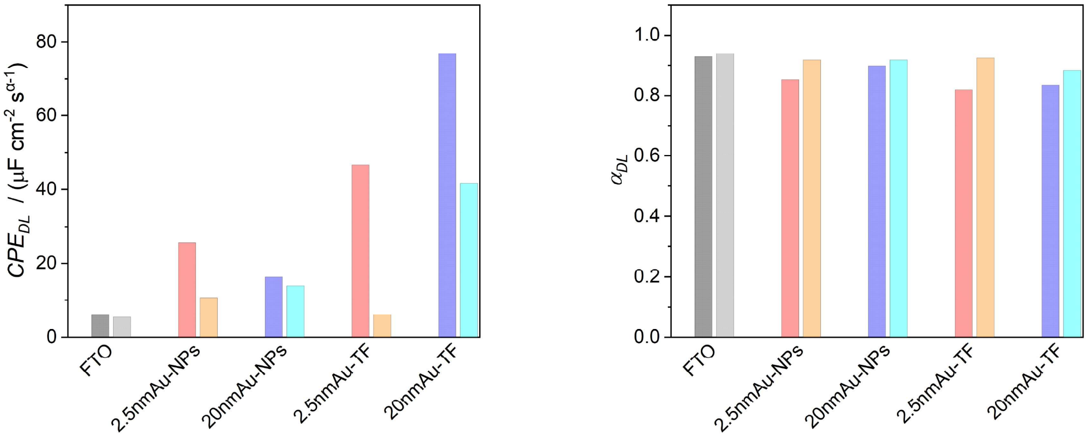

Figure 5.16 - Variation of (A) CPE_{DL} and (B) α_{DL}

Figure 5.17 shows that the value of charge transfer resistance is initially the same for all electrodes. Post-testing, the measured value remains stable for FTO electrodes but increases for gold-FTO electrodes. This change is more pronounced in samples with 2.5 nm films and their corresponding nanoparticles compared to those with 20 nm films and larger nanoparticles, suggesting potential stability concerns associated with reduced dimensions.

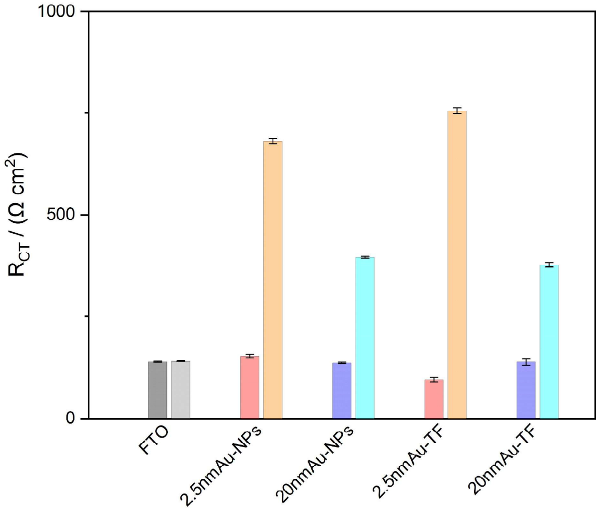

Figure 5.17 - Variation of R_{CT}

The evaluation of the Warburg element (Z_W) (Figure 5.18 A) allowed to obtain the mass transfer resistance R_W and the time constant τ, as $Z_W = R_W \mathrm{cth}[(\tau i\omega)^{\alpha_W}](\tau i\omega)^{-\alpha_W}$, where $\alpha_W < 0.5$.[91] The trend of R_W for different electrodes highlights that the mass transfer resistance decreases after the tests for FTO and all the nanoparticle electrodes, while the behavior of film-coated FTO is unclear as the error associated to the values obtained by the fitting is much higher. Similar conclusions can be drawn for the mass transfer time, while the value of α_W (the exponential factor) is constant for all the electrodes, equal to 0.5. This suggests that the same transport phenomenon is occurring and thus any difference in electrode's performances must be due to an intrinsic property of the material. (Figure 5.18 B)

Harsha et Al. reached a similar conclusion regarding this critical point while investigating the hydrogen evolution reaction (HER) activity of model Pt thin films versus dewetted Pt nanoparticles under both static and hydrodynamic conditions.[21] The observed differences in activity were found to be intrinsic rather than attributable to variations in mass transport arising from differences in electrode morphology (thin films *vs*. nanoparticles).

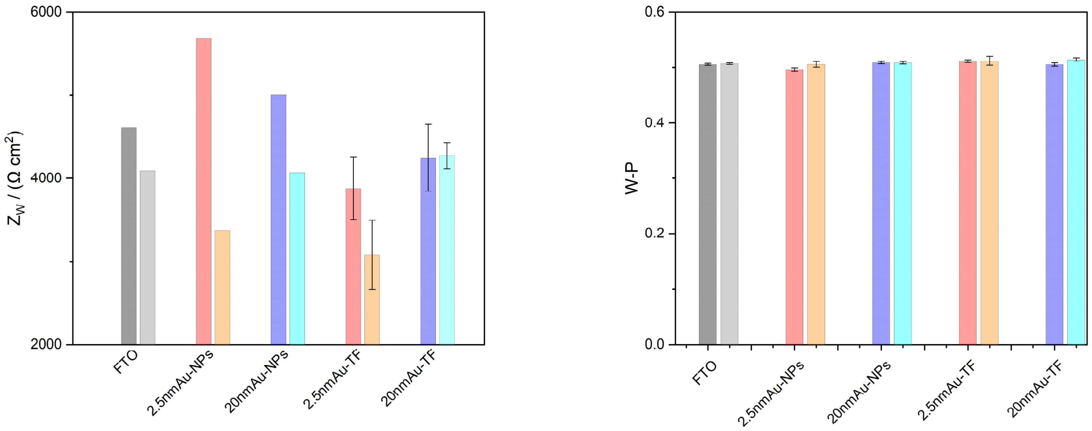

Figure 5.18 - Variation of Zw and W-P

SEM images were also recorded after the test with ferrocyanide, showing significant changes in the 2.5nmAu-NPs sample's morphology. The average particle size after the tests changes from (14 ± 2) nm to (19.4 ± 0.5) nm for the exposure toward $K_4[Fe(CN)_6]$. It is possible to observe that the smaller nanoparticles, initially present on the sloped sides of FTO, were lost during the process. Overall, the particle size analysis changes as shown in Figure 5.19 C-D. It is also noticeable that the morphology of the remaining nanoparticles changed, being rougher and with some dendrites on the surface. This phenomenon can particularly be observed in the 20 nm dewetted nanoparticles, where the diameter increases to (316 ± 34) nm and the roughness also increases, as shown in Figure 5.19 B.

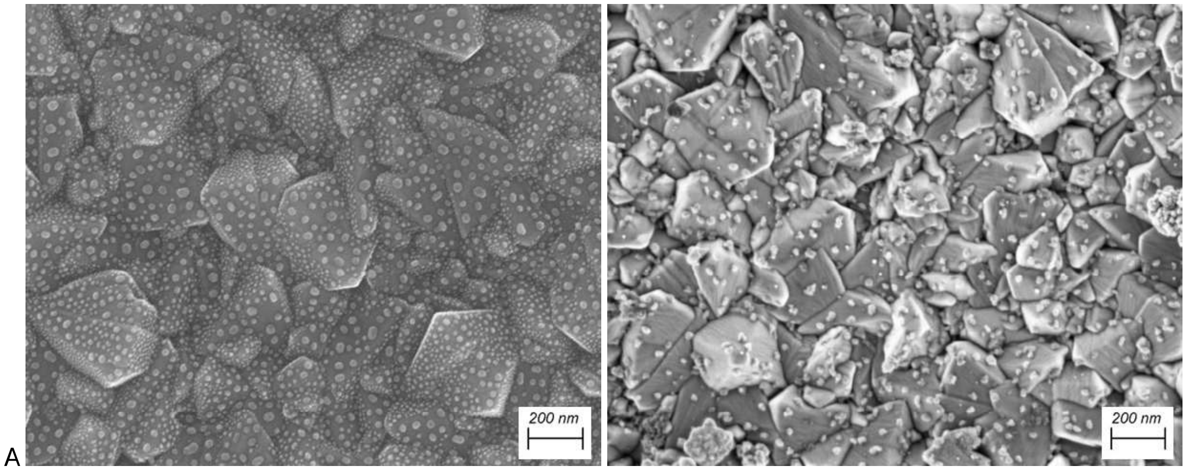

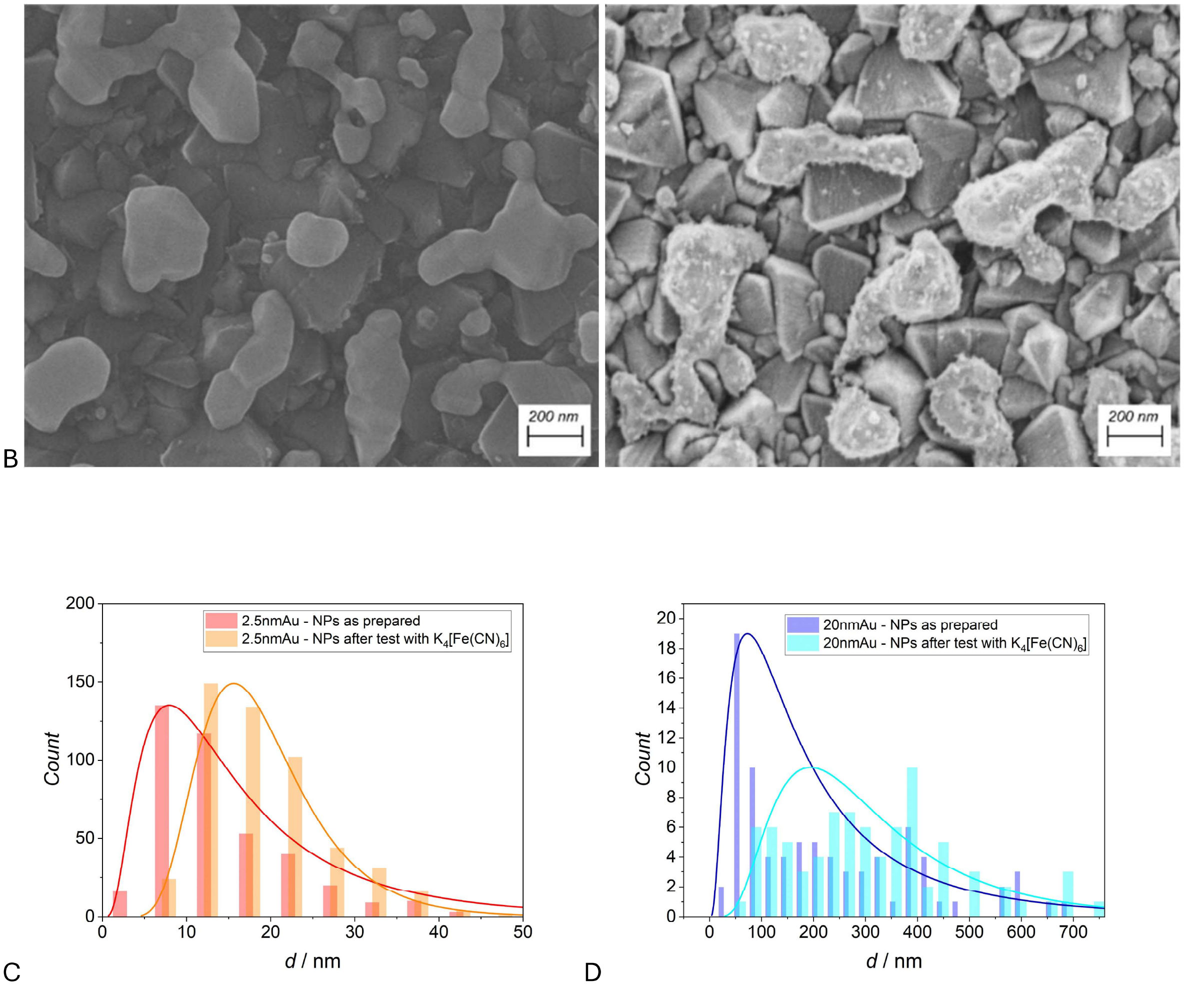

Figure 5.19 - SEM images of (A) 2.5 nm NPs and (B) 20 nm NPS before and after tests in $K_4[Fe(CN)_6]$ 1 mM, with their particle size distribution change (C and D, respectively)

EDX measurements showed a reduction of gold content of 72% for the 2.5nmAu NPs sample and of 20% for 20nmAu - NPs (Table 5.3). The loss of gold can also be observed visually and via UV-Vis spectroscopy (Figure 5.20). It is interesting to note that the UV-spectra recorded on three different spots of the sample overlay before the tests but after the test there is more variability, suggesting that the surface become less even. It is also worth noting that the LSPR resonance peak shifted to shorter wavelengths.

Table 5.3 - Values of EDX measurements

Conditions	NP size (initial film thickness) / nm	Gold percentage
Fresh samples	0	0 ± 0
	2.5	5.0 ± 0.6
	5	7.7 ± 0.5
	10	20.6 ± 0.4
	20	34 ± 2
After $K_4[Fe(CN)_6]$ test	2.5	1.4 ± 0.1
	20	27 ± 1

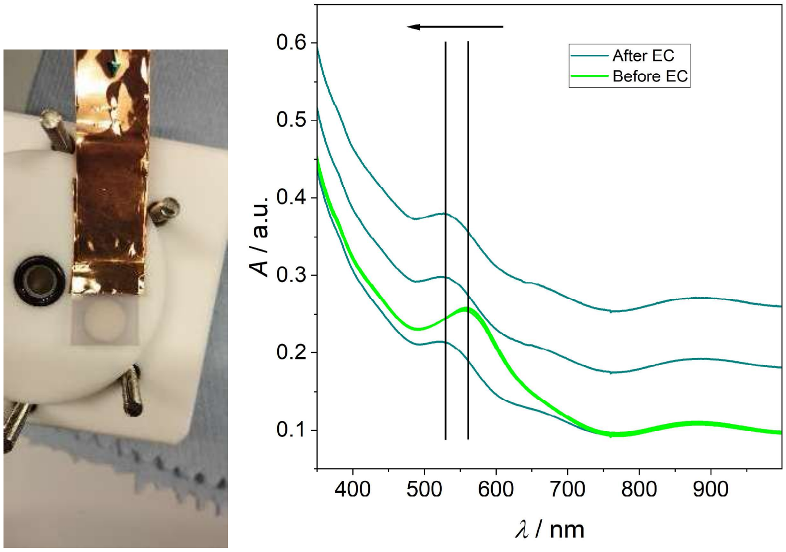

Figure 5.20 – (A) Images of the electrode after test with $K_4[Fe(CN)_6]$ 1 mM and (B) Uv-Vis spectra of a used electrode

Moving to the films, it is clear that a big difference is present in the 2.5nmAu-TF treated with the iron probe, as shown in Figure 5.21 A-B. In this case, the as-deposited film is not uniform as it presents spontaneous dewetting, due to its high surface energy and high surface mobility of Au atoms, which makes the film partially agglomerating.[92] As for the thicker film (Figure 5.21 C-D) before treatment, the FTO electrode is almost completely covered. After the tests, the film is still intact, but the morphology of the surface is much different and rougher. The bigger particles formed on the surface are (25 ± 3) nm sized.

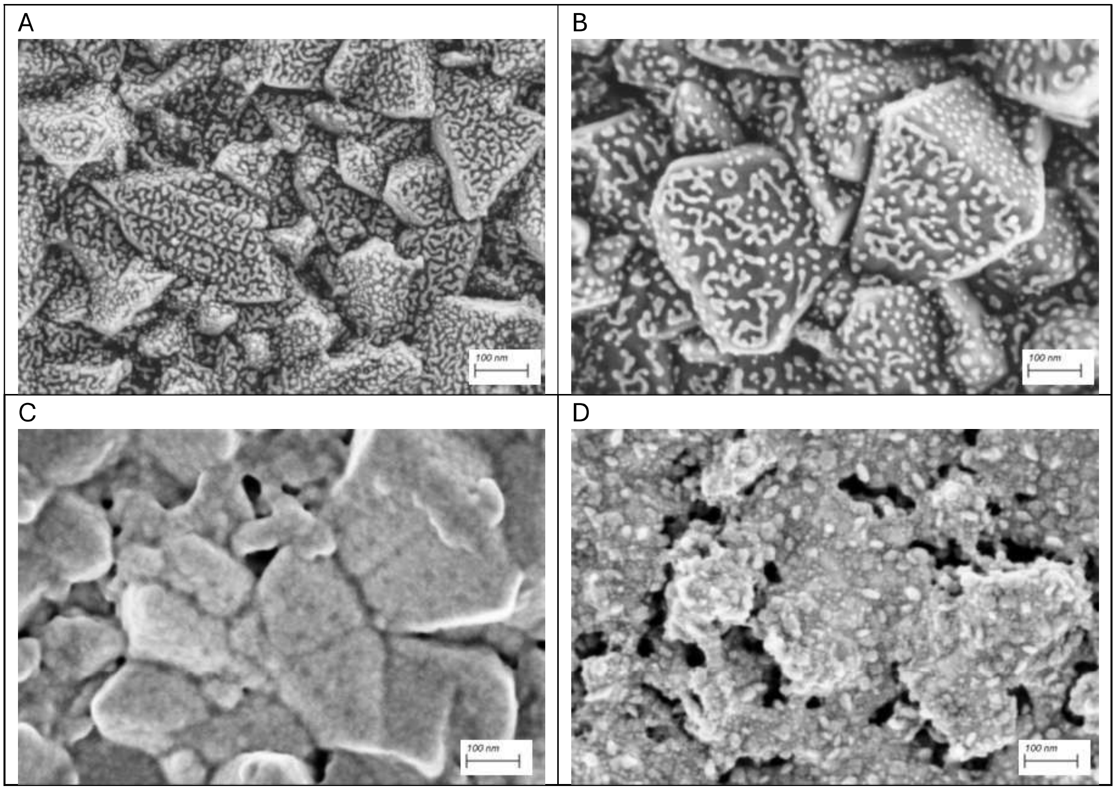

Figure 5.21 - SEM images of 2.5 nm gold film before (A) and after (B) the test in $K_4[Fe(CN)_6]$ 1 mM and of 20 nm gold film before (C) and after (D) the test in $K_4[Fe(CN)_6]$ 1 mM

The changes of the various tested electrodes are summarized in Figure 5.22.

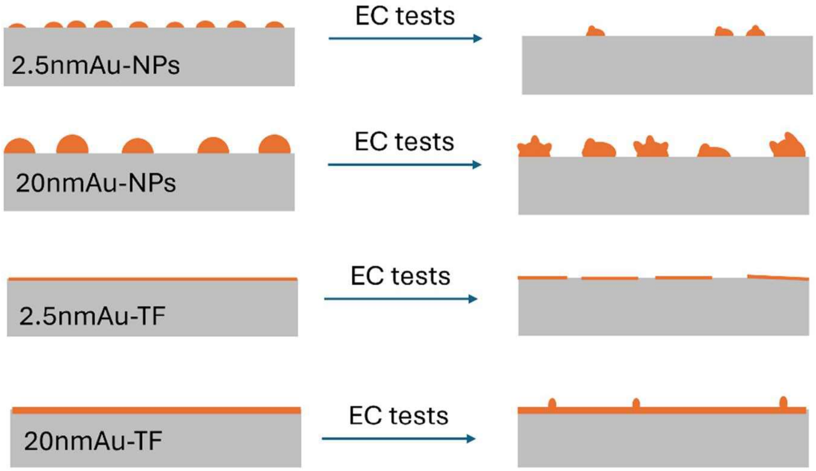

Figure 5.22 - Changes observed for the tested electrodes after cycling in 1 mM $K_4[Fe(CN)_6]$.

5.5 H_2O_2 Detection

In order to test the sensing performances of the selected electrodes, different analytes were considered. The main goal was to find a molecule that could selectively react with the gold structure, without being influenced by the presence of the conductive FTO support. The first one is dopamine. It is known in the literature that it behaves as inner sphere molecule, thus it was considered useful to investigate the morphology dependent behaviors of the devices. Unfortunately, as shown in Figure 5.23, It quickly polymerized on the Au nanoparticles thanks to their excellent catalytic activity.

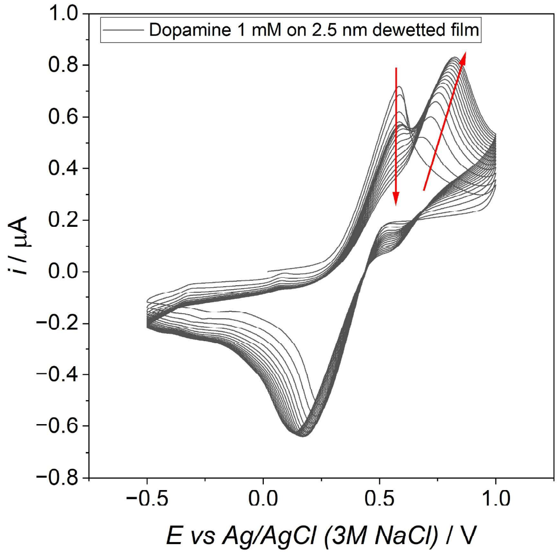

Figure 5.23 - CV recorded on a FTO/Au electrode in $NaClO_4$ 0.1M and dopamine 1 mM

Another molecule that was considered is glucose. Glucose mechanism is widely studied in the literature,[93] and lead to a characteristic CV signal, as reported in Figure 5.24 A. In order to facilitate glucose oxidation, a alkaline pH is needed. Ash shown in Figure 5.24 B, this drastically accelerated the dissolution of gold.

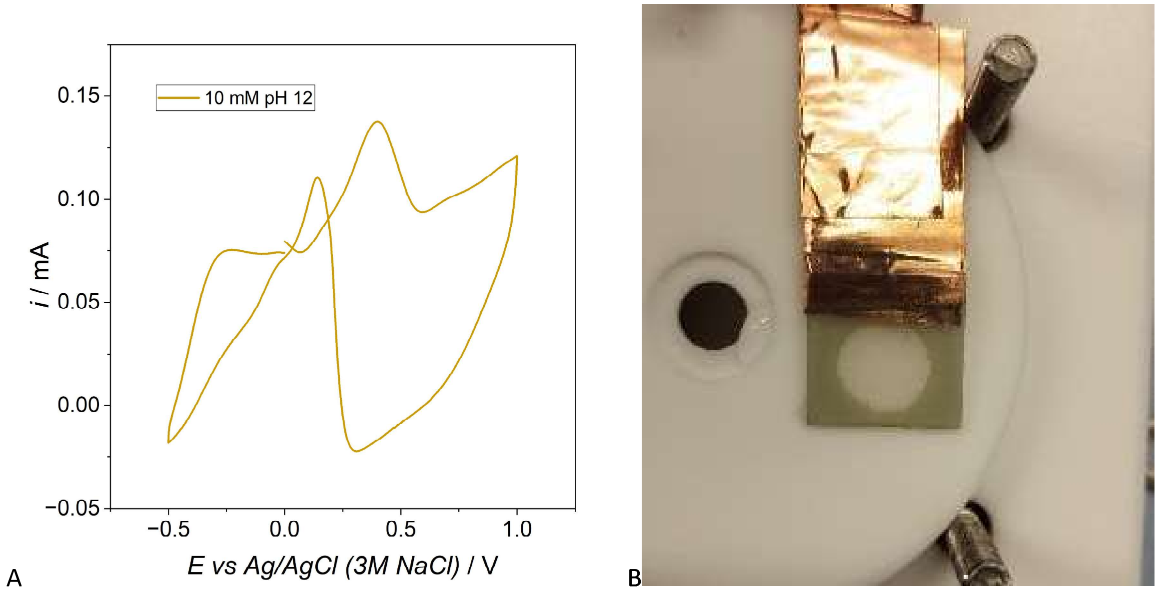

Figure 5.24 - (A) Cv recorded with a FTO/Au electrode in presence of 10 mM glucose at pH 12 and (B) discolouration of the used electrode

Finally, H_2O_2 was selected because of its selectivity toward gold and the possibility to work with pH close to neutral. In order to better understand the behavior of gold in a solution of supporting electrolyte and with H_2O_2, preliminary studies were conducted using a bulk gold electrode. In particular, a gold tip from Metrohm with a 2mm diameter was used.

The behavior of a gold electrode was first investigated without the addition of H_2O_2. When the anodic potential is increased, a gold oxide layer is formed on the electrode and a proportional gold oxide reduction peak is observed at + 0.2 V, as shown in Figure 5.25. Initially, the lower vertex potential of the CV scan was kept at -0.5 V vs SCE and the upper vertex was progressively increased. When working up to + 0.4 V, no oxide layer is formed and thus only a cathodic peak is observed, due to the reduction of dissolved oxygen in solution.

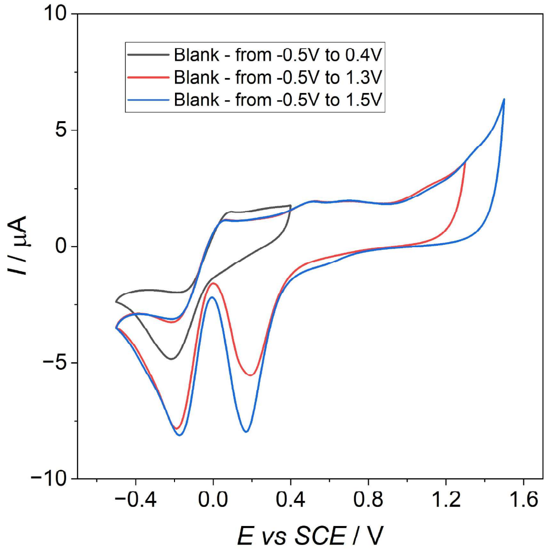

Figure 5.25 - CV recorded between -0.5 V and 0.4, 1.3 and 1.5 V, showing how the increase of the upper vertex potential influenced the cathodic peak at 0.2V

The anodic region was studied by keeping the lower vertex potential at 0V, and progressively increasing the upper one as shown in Figure 5.26 A. When the potential is increased above + 1.2 V, a second reduction peak is obtained at + 0.6V vs SCE.

As for the cathodic region, it was investigated by keeping the upper vertex potential at + 0.4 V and scanning at progressively lower potential values (Figure 5.26 B). As the lower vertex potential is lowered, the characteristic signal for H_2 evolution become evident. Two more peaks can be identified, one anodic at + 0.1V and one cathodic at 0V, whose intensities increases as the lower vertex potential is shifted to lower values.

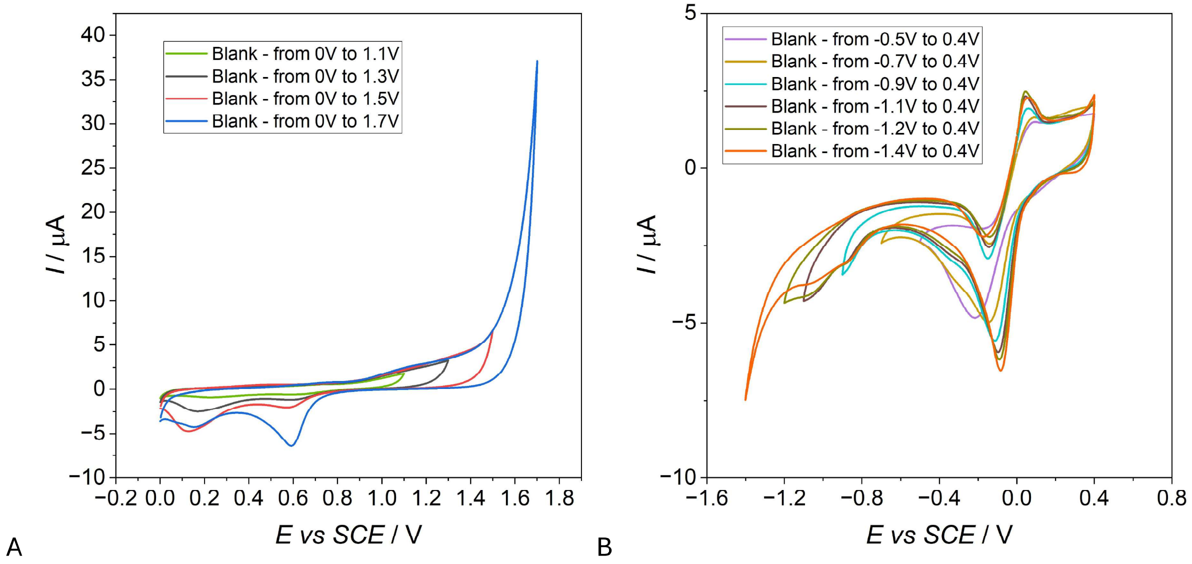

Figure 5.26 – Cv study of the (A) anodic and (B) cathodic region of the gold electrode

Then, H_2O_2 was added to understand whether the molecule could be detected in both regions. As shown in Figure 5.27, the presence of the molecule could be detected both as reduction, with an increase of the cathodic peak at -0.1V, and as oxidation, above + 1V.

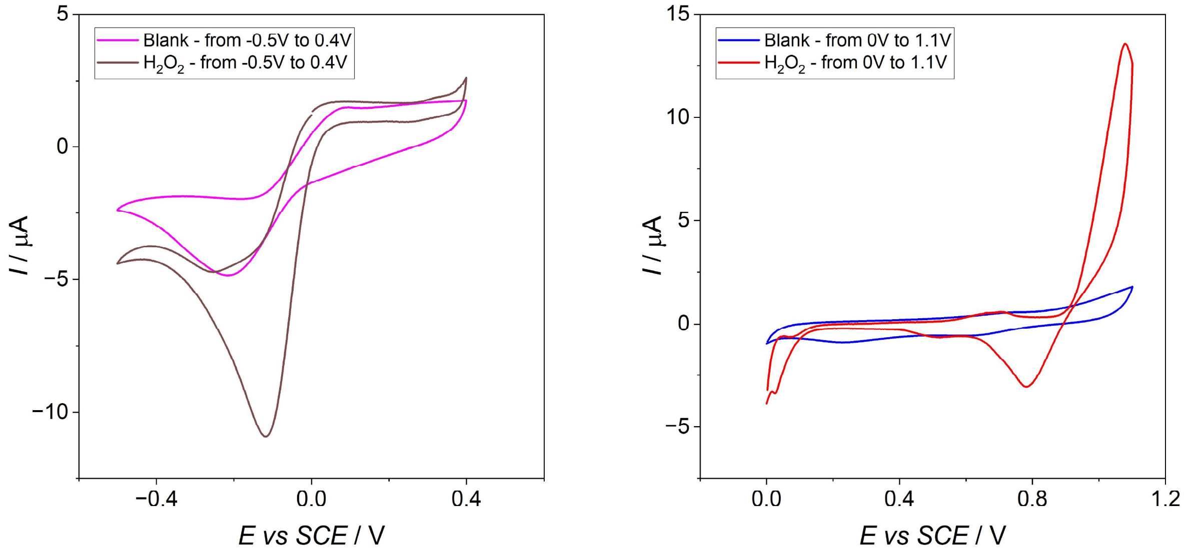

Figure 5.27 - Behavior of the gold electrode in presence of 1 mM H_2O_2 in 0.1M $NaClO_4$

The detection was performed using cyclic voltammetry, by monitoring both the H_2O_2 oxidation reaction and the H_2O_2 reduction reaction, using freshly prepared electrodes. A 20nmAu-TF electrode was used as "gold film reference", as previous data showed it had good stability, and was compared with the 2.5nmAu-NPs and 20nmAu-NPs, to highlight how different size of nanoparticles could affect the sensing performances.

For all the samples, multiple cycles are recorded until stabilization is achieved at the 15th cycle. Such curves are reported in Figure 5.28, and are consistent with the behavior that is reported in the literature for H_2O_2 in a slightly acidic environment. H_2O_2 oxidation and reduction signals can be observed at + 1 V and -0.2 V (vs. Ag/AgCl), respectively.[52] The characteristic signals of gold are also present: gold oxidation occurs between +0.4 and +0.8 V, while the gold oxide reduction is located at +0.2 V. These processes are slightly affected by the presence of oxygen and H_2O_2 in solution, with the oxidation current increasing with the concentration of H_2O_2 and the cathodic one following the opposite trend.

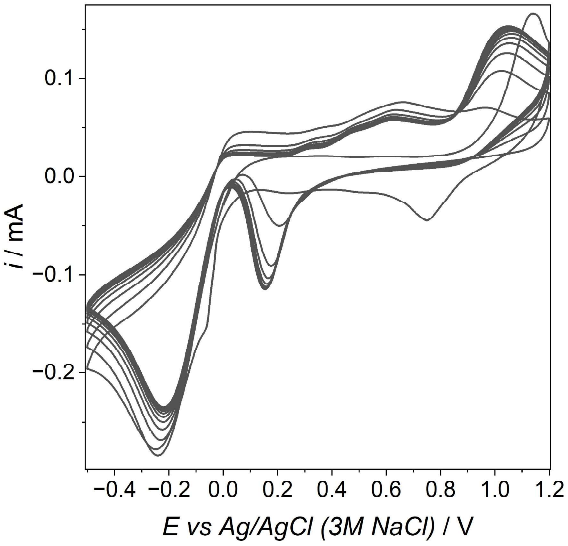

Figure 5.28 - Consecutive CV recorded for the addition of H_2O_2 in $NaClO_4$ 0.1 M

Both the H_2O_2 reduction and oxidation peaks were used to prepare a calibration plot, as shown in Figure 5.29, in a concentration range of 0 – 5 mM.

The calibration was performed using the intensity of the signal, corrected by subtraction of the baseline. The obtained sensitivity data were also normalized by the ECSA per unit mass of Au of each electrode (data discussed in Table 1). The results are shown in Figure 5.29 B-C. It is clear that the small nanoparticles present the best performances as they allow to obtain a good sensitivity while being made with one tenth of the quantity of gold. This can be explained with a different diffusion process occurring at the electrode surface, as small nanoparticles behaves as a microelectrode array.[94]

The presence of both anodic and cathodic signals, each exhibiting good sensitivity, can be particularly valuable in the quantitative analysis of real-world samples. A discrepancy between the two quantification results may suggest the existence of an interfering species. By conducting a more in-depth investigation of the sample solution, it may be possible to determine which of the two electrochemical reactions is more reliable under the given conditions. This selective approach would allow for accurate quantification of hydrogen peroxide (H_2O_2), even in the presence of potential interferents.

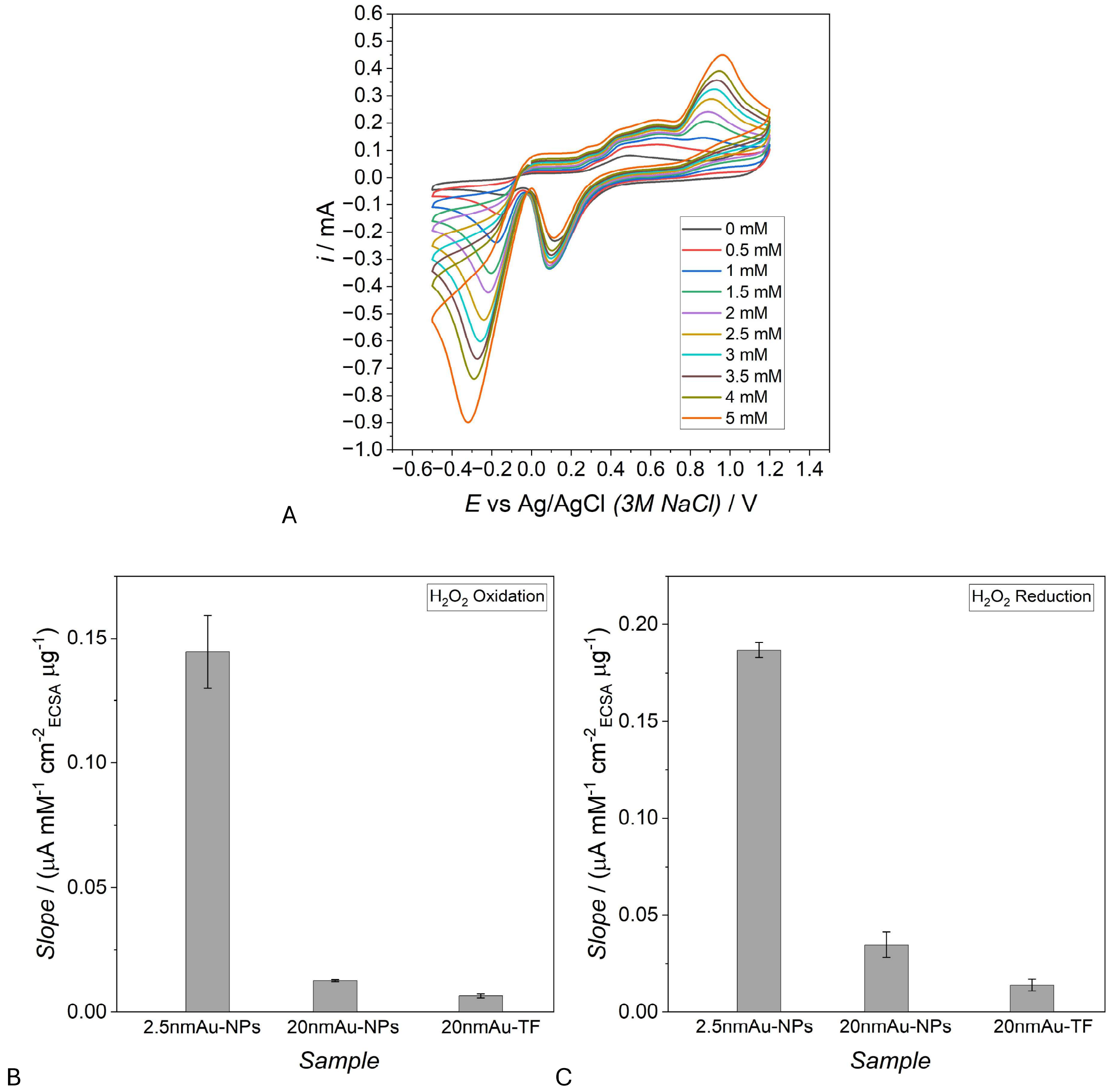

Figure 5.29 - (A) CV recorded in NaClO4 0.1 M with increasing concentrations of H2O2. Sensitivity obtained in the anodic (B) and cathodic (C) peaks

5.6 Conclusions

This study demonstrates the possibility to use solid state dewetting as reliable method for the preparation of controlled nanoparticles of various sizes. The trade-off between stability and performance in gold nanoparticle-based electrodes was investigated: while small nanoparticles exhibited superior H_2O_2 detection capabilities and present a cost-effective option, their reduced stability compared to larger nanoparticles and thick films poses a limitation for long-term applications.

The findings highlight the importance of optimizing nanoparticle size and film thickness to balance sensitivity and durability. Future research will focus on addressing this issue by developing protective coatings, such as a thin TiO_2 layer,[95] to enhance the longevity of small nanoparticles while maintaining their excellent performance characteristics.

6 Dewetted AuNPs/TiO_2 electrode

In the previous chapter, the sensing performance and long-term stability of gold nanoparticles (AuNPs) of various sizes synthesized via thermal dewetting of thin gold films were investigated. The study revealed a critical trade-off: while smaller nanoparticles often exhibited enhanced sensing capabilities, they suffered from reduced structural stability, highlighting the need for a balanced design strategy of the final device.

To address this challenge, one promising approach involves the introduction of a protective layer made with a different material. This strategy aims to preserve the high performance intrinsic to gold-based electrodes while enhancing their durability under operational conditions. Such a concept is well-established in the field of electrocatalysis, where precious metal catalysts are often supported or encapsulated to optimize both efficiency and lifespan—particularly in demanding applications such as fuel cell technology and other electrochemical conversion systems.

In this context, titanium dioxide (TiO_2) was selected as the protective material of choice. TiO_2 not only serves as a physical barrier to prevent degradation of the gold nanostructures, but also introduces new functional attributes to the electrode system. As already discussed, TiO_2 exhibits unique photoactive and photo-renewable properties that can be harnessed to enhance the overall performance and versatility of the electrode platform. This dual functionality—structural protection and photoactivity—positions TiO_2 as a valuable component in the design of next-generation, multifunctional electrochemical devices.

6.1 Electrodes preparation and characterization

For the preparation of the electrodes, FTO-coated glass slides functionalized with dewetted gold nanoparticles were covered with TiO_2 via dip coating in a TiO_2 sol. The detailed experimental conditions are reported in sections 10.1and 10.5, and the procedure is schematized in Figure 6.1.

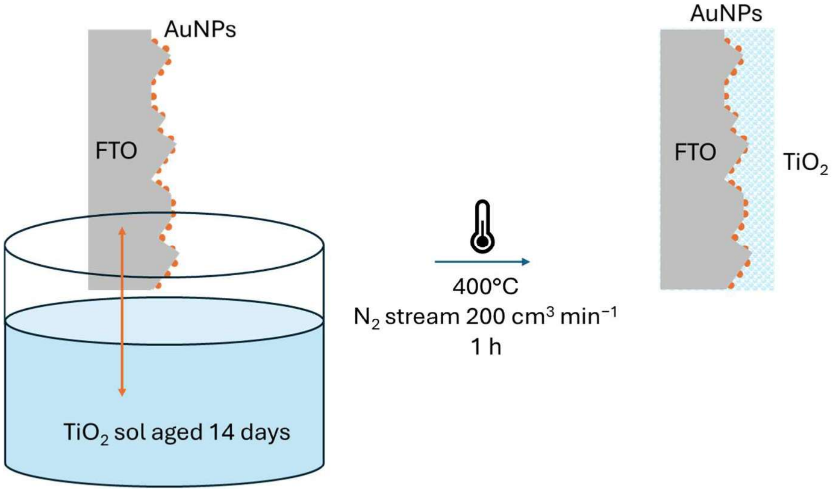

Figure 6.1 - Preparation of the TiO_2-coated dewetted gold electrodes

A calibration line was prepared by using EDX measurements, as reported in Chapter 5.3. As shown in Figure 6.2, a typical spectra shows the percentages of gold, silicon, tin, and titanium. The detection of all constituent materials within the sample confirms that an accelerating voltage of 15 kV provides sufficient electron penetration to traverse the entire multilayer structure.

Due to the presence of titanium, a different calibration line was required compared to the previous chapter. The obtained calibration plot is reported in Figure 6.3. As expected, it is characterized by a good linear relationship between obtained gold percentage and the initial amount of sputtered gold.

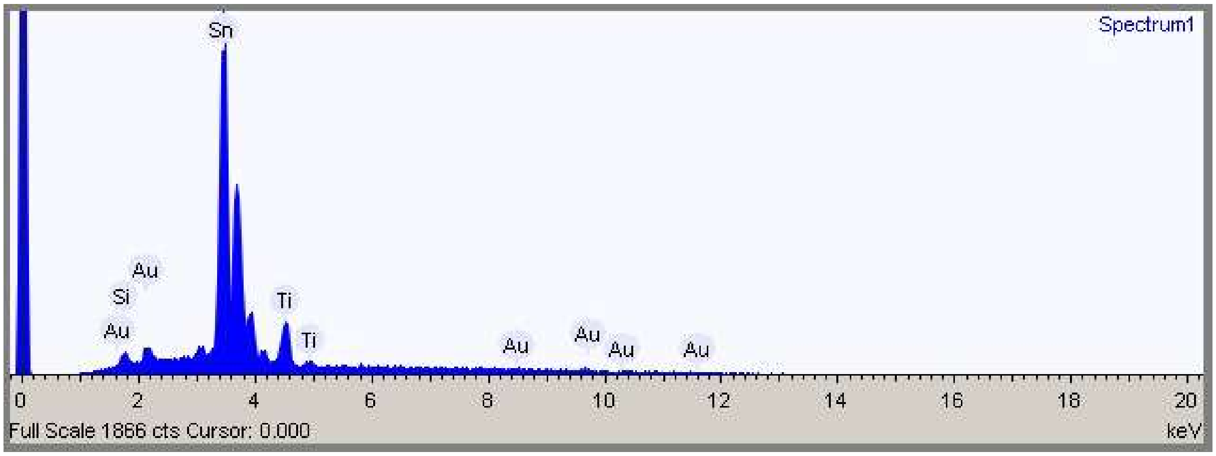

Figure 6.2 - Typical EDX spectrum obtained for TiO_2/Au/FTO electrodes

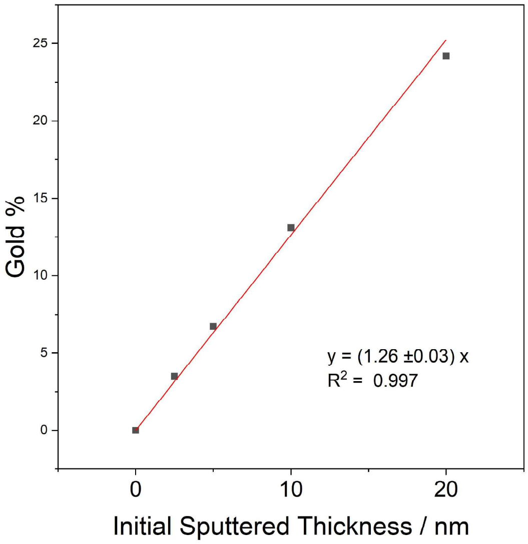

Figure 6.3 - EDX calibration plot for gold content in the samples

SEM images were recorded for the electrodes after TiO_2 covering. The layer seems to be uniform, with some larger grains of TiO_2 clearly identifiable as darker marks. When comparing the samples with the smallest amount of gold (Figure 6.4 A) and highest amount of gold (Figure 6.4 B), a clear change of surface conductivity is observed.

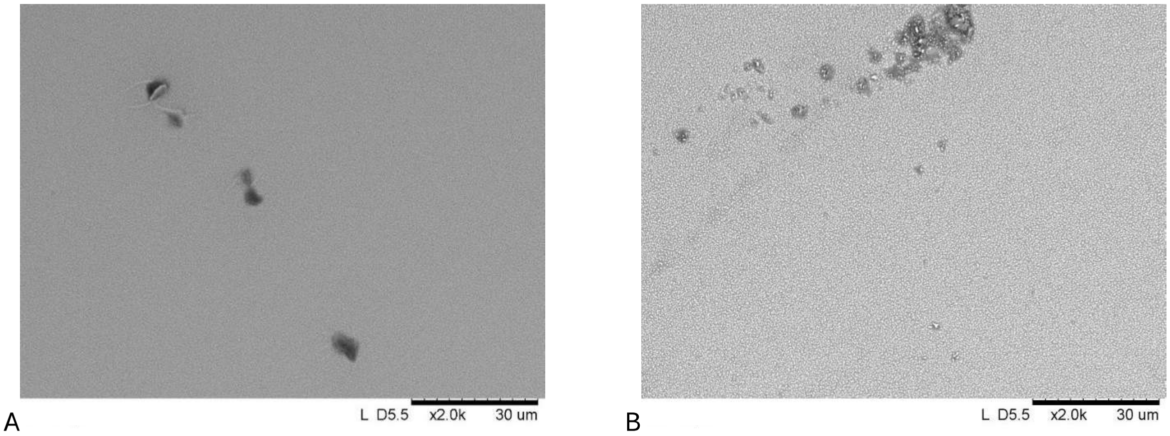

Figure 6.4 - SEM images of the TiO_2 layer covering (A) 2.5 nm dewetted film and (B) 20 nm dewetted film

The UV spectra of the prepared electrodes were also recorded, as shown in Figure 6.5. the LSPR peaks of the nanoparticles shift slightly compared to those recorded before TiO_2 deposition (Figure 5.10), indicating a possible interaction with the TiO_2 layer or a change of distribution that takes place during the TiO_2 annealing process.

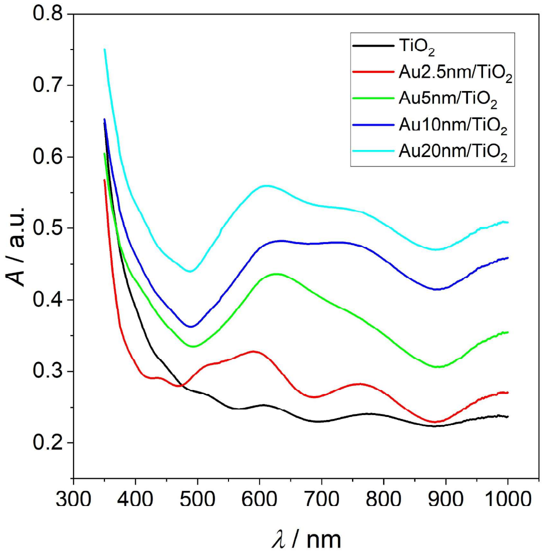

Figure 6.5 - UV-Vis spectra of the prepared electrodes

Cyclic voltammetry was used to investigate the behavior of the electrodes. The CVs, recorded in 0.1M $NaClO_4$, are reported in Figure 6.6. Here, a major difference can be observed relative to the behavior of uncovered gold nanoparticles: all the samples present very similar area of the gold oxide reduction peak at + 0.4 V vs SCE. Furthermore, the scale of the intensity is only a fraction of that observed with uncovered particles, since the TiO_2 layer insulate the surface. The deposition of a conformal layered structure leads to an apparent homogenization of the accessible surface area. This suggests that the coating effectively masks the intrinsic surface heterogeneity, resulting in a uniform interface regardless of particle size.

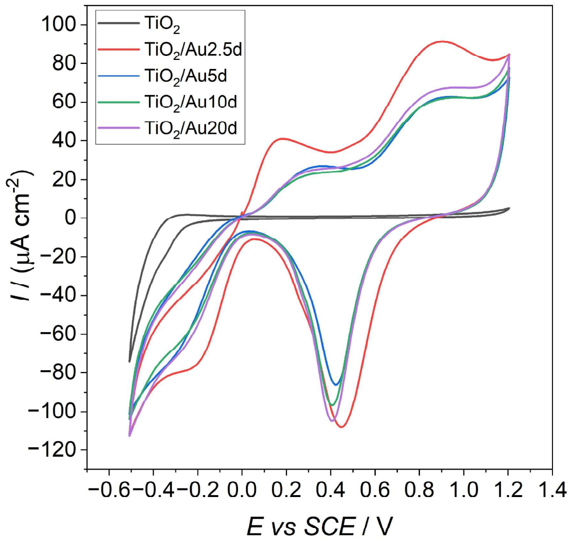

Figure 6.6 - CVs recorded in NaClO$_4$. Scan rate = 100 mV/s

As expected, the gold ECSA values, calculated according to Equation 5.1, are much lower compared to the one of uncovered gold structures. The obtained values, similar for all the prepared samples, are reported in Table 6.1.

Sample	Charge / μC	ECSA / cm^2	Rf
2.5	0.315	$8.20\ 10^{-4}$	0.0029
5	0.208	$5.42\ 10^{-4}$	0.0019
10	0.221	$5.77\ 10^{-4}$	0.0020
20	0.239	$6.23\ 10^{-4}$	0.0022

Table 6.1 - Values of Charge, ECSA and Rf calculated for gold functionalized FTO electrodes covered with the TiO$_2$ layer

Interestingly, the characteristic gold peaks appear to be shifted compared to the exposed gold structure, as reported in Figure 6.7 for the electrode prepared with the largest nanoparticles. The same trend is also observed for smaller nanoparticles. Such difference can be attributed to the interaction with TiO$_2$.

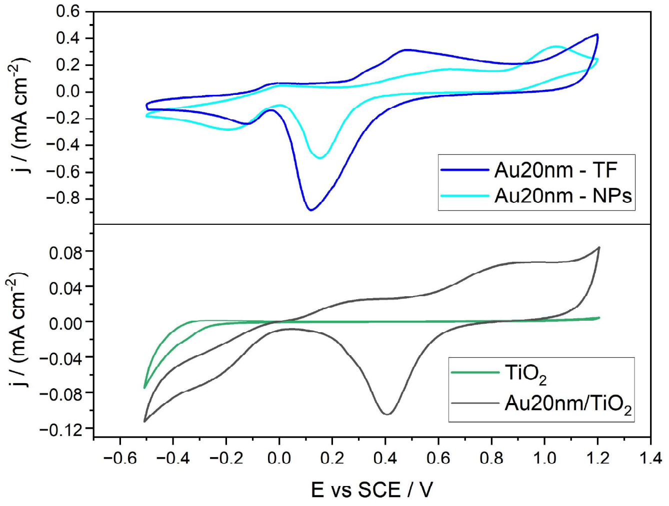

Figure 6.7 - CVs recorded in NaClO$_4$ 0.1M at 100 mV/s with exposed gold structures (Above, thin films and nanoparticles), and the nanoparticles covered by the TiO$_2$ layer (below, reported with a bare layer of TiO$_2$)

As explained in Section 5.4, further studies were conducted investigating the stability of the electrodes, focusing on the one with the smallest and higher amount of gold.

6.2 Stress tests

The stability of the obtained electrodes was evaluated by cycling multiple times in 1 mM $K_4[Fe(CN)_6]$, using $NaClO_4$ 0.1 M as supporting electrolyte and recording EIS every 10 cycles. First a layer of TiO_2 on FTO was tested to evaluate its stability. As shown in Figure 6.8 no significant changes are observable, indicating its good stability.

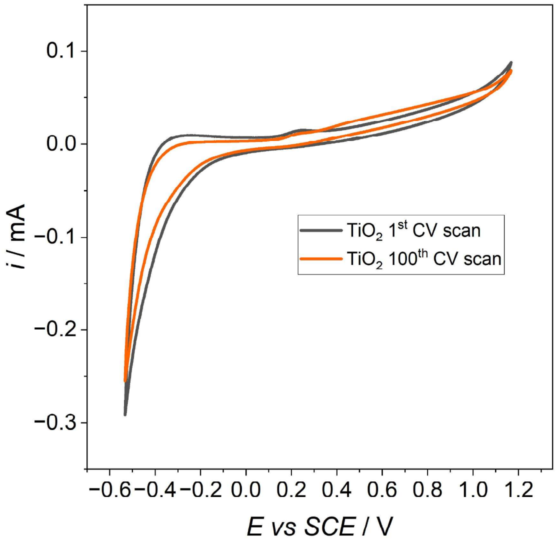

Figure 6.8 - CV of TiO_2 layer on FTO before and after 100 scans in $K_4[Fe(CN)_6]$

Stability of the TiO_2 layer was also confirmed by EIS spectroscopy, reported in Figure 6.9 . A decrease in the resistance can be attributed to the slow diffusion of the probe molecule in the TiO_2 pores, which facilitates the reaction.

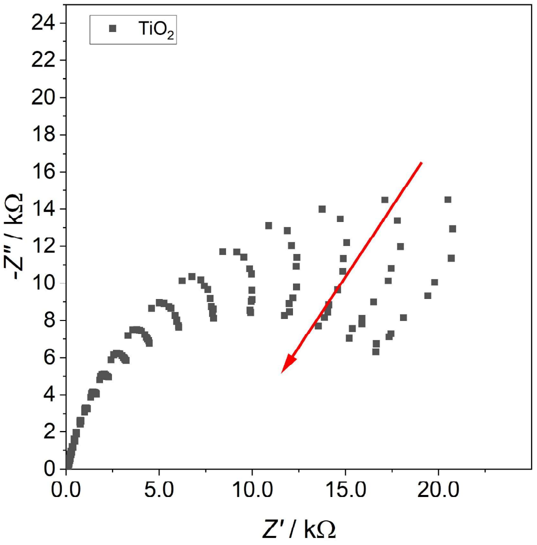

Figure 6.9 - EIS recorded every 10 CV cycles in $K_4[Fe(CN)_6]$ 0.1 M with a FTO/TiO_2 electrode

Although the sample's resistance varies significantly throughout the test, the disparity compared to a bare FTO electrode remains considerable. This is especially clear in Figure 6.10.

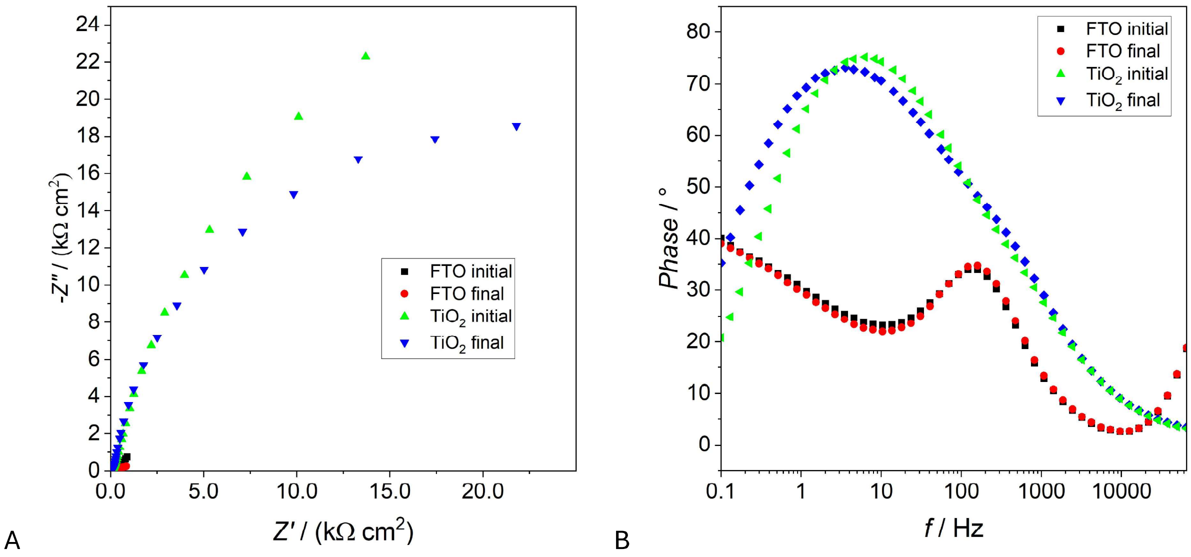

Figure 6.10 - (A) Nyquist and (B) Bode Phase EIS plots of FTO and FTO/TiO_2 electrodes before and after the treatment with $K_4[Fe(CN)_6]$

A different behavior is observed for the electrodes containing gold. It is clear from Figure 6.11 B that the amount of gold in the Au20nm/TiO_2 sample remained almost constant (no significant changes in the gold reduction peak at + 0.4 V is observed). The apparent increase of the gold oxidation signal between 0.2 an 1 V can be attributed to a cleaning of the electrode surface that takes place upon cycling. On the other hand, the 2.5nm /TiO_2 showed a decreased intensity, possibly due to loss of gold during the test.

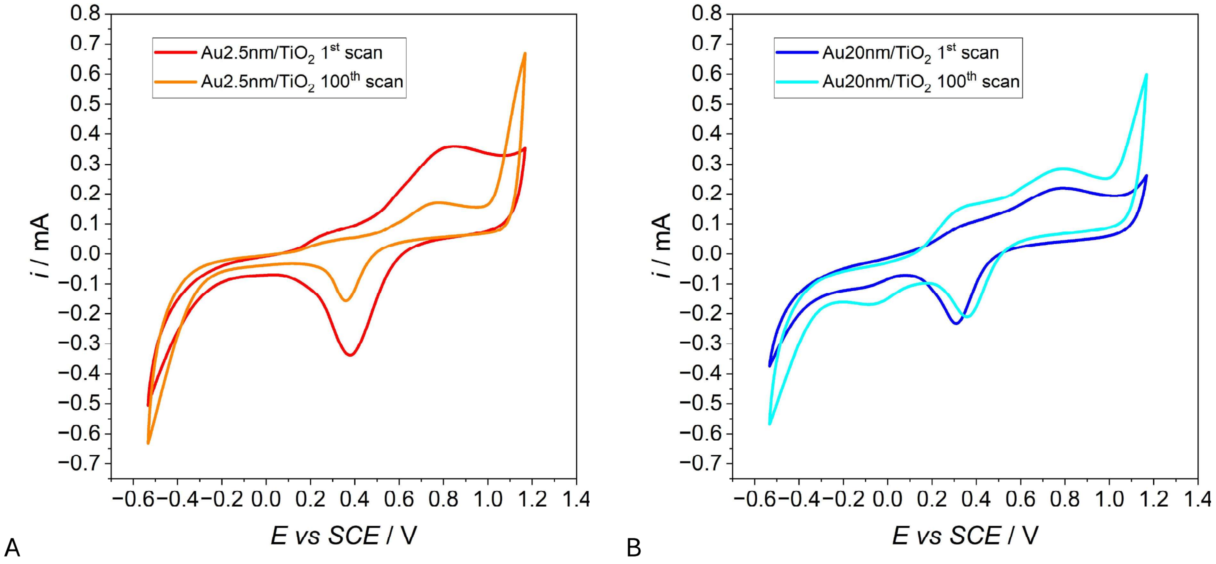

Figure 6.11 - CV recorded before and after the tests with $K_4[Fe(CN)_6]$ 1 mM for (A) 2.5nm-NPs/TiO_2 and (B) 20nm-NPs/TiO_2

This observation was confirmed by EDX analysis: Au2.5nm/TiO_2 showed a reduction of gold quantity from (3.5 ± 0.1)% to (1.5 ± 0.1)%, while Au20nm/TiO_2 remained virtually unchanged, from (24.2 ± 0.3)% to (24.55 ± 0.07)%.

EIS measurements highlight that during the stability test the semicircle for the Au2.5nm/TiO_2 electrode increase (Figure 6.12). This behavior is similar to that observed for uncovered nanoparticles, and indicated a progressive wearing of the electrode. On the other hand, the value for the Au20nm/TiO_2 electrode decreases. This is more similar to the behavior of the TiO_2 layer.

The results suggest that in the first case the phenomenon that prevails is the electrode degradation, possibly due to the loss of gold, while in the second and in the case of the bare TiO_2 layer, the change is related to a better diffusion of the probe toward the active surface.

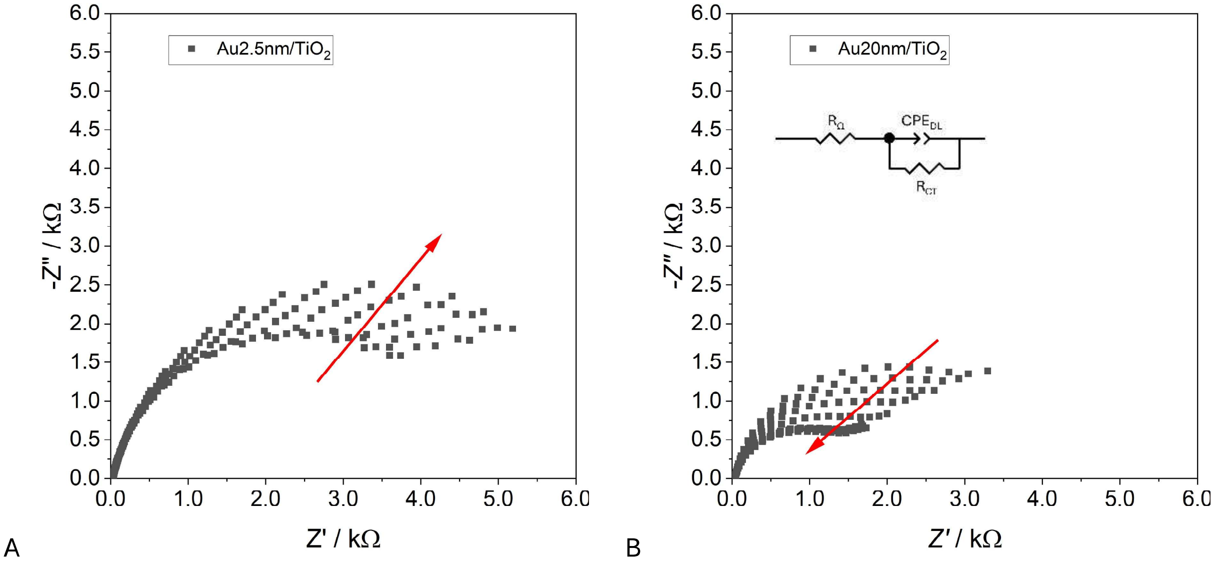

Figure 6.12 - Nyquist's plot change during the test for (A) Au2.5nm/TiO_2 and (B) Au20nm/TiO_2 electrodes

This explanation is also supported by the absence of mass transport resistance (Warburg element) in the Au2.5nm/TiO_2 electrode, and by its progressive appearance in the Au20nm/TiO_2 electrode. Unfortunately, the number of points recorded at low frequencies were not enough to fit such parameter. The fitted values, obtained using the circuit reported in Figure 6.12 B, are reported in Table 6.2.

Sample		R_Ω / (Ω cm^2)	CPE_{DL} / (µF cm^{-2} $s^{\alpha-1)}$	α_{DL}	R_{CT} / (kΩ cm^2)
TiO_2	initial	57.30	25.7 ± 0.7	0.793 ± 0.005	77 ± 7
	final	56.51	22.4 ± 0.7	0.827 ± 0.006	37 ± 2
Au2.5nm/TiO_2	initial	83.76	49.1 ± 0.4	0.880 ± 0.002	13.1 ± 0.1
	final	80.23	30.0 ± 0.2	0.861 ± 0.001	17.6 ± 0.1
Au20nm/TiO_2	initial	84.84	44.7 ± 0.6	0.860 ± 0.003	8.7 ± 0.1
	final	80.40	60.0 ± 0.8	0.822 ± 0.003	4.0 ± 0.1

Table 6.2 - Fitted parameters for the TiO_2-covered electrodes

6.3 Photo-electrochemical behavior

Chronoamperometry recorded under intermittent LED irradiation and Electrochemical Impedance Spectroscopy – both under irradiation and in darkness – were recorded to study the photoactive behavior of the electrodes.

EIS was recorded at two different values of applied potential, 0V and + 0.3V. These values were selected to highlight how the material response changed in more anodic conditions, similar to those required for the successive detection applications.

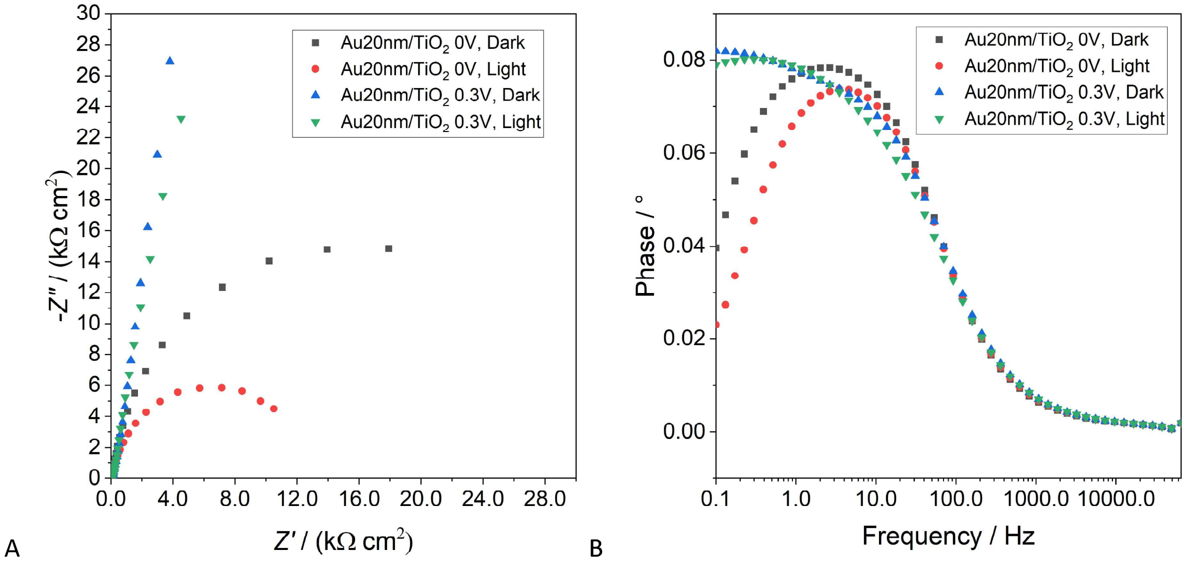

Figure 6.13 - Nyquist (left) and Bode Phase (right) plots for a Au20nm/TiO_2 electrode in $NaClO_4$ 0.1 M, highlighting how different conditions of applied potential and irradiation affect its behavior

An example of the recorded plots is reported in Figure 6.13, for the Au20nm/TiO_2 electrode. It is clear that at relatively high applied potential the electrode behaves as a capacitor, while a faradaic reaction was present at lower applied potential. It is possible that at 0.3V the anodic reaction of gold oxidation and the cathodic gold oxide reduction coexists, thus only the capacitive behavior emerges. At 0V, only the onset on gold oxidation takes place. Based on these results, the data were fitted using the equivalent circuits reported in Figure 6.14, depending on which behavior was observed.

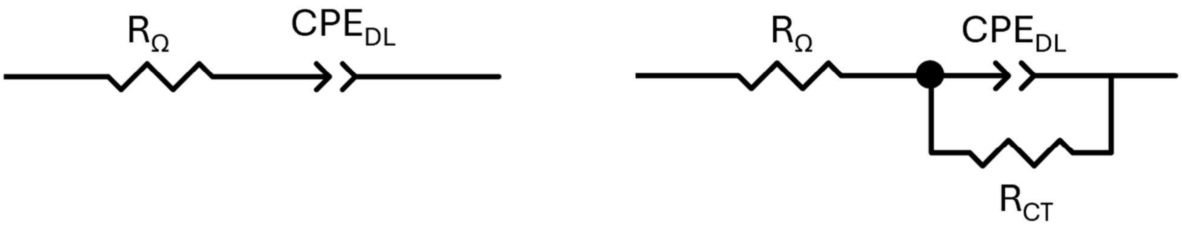

Figure 6.14 - Equivalent circuit for non-ideal capacitive behavior (left) and Randles model (right)

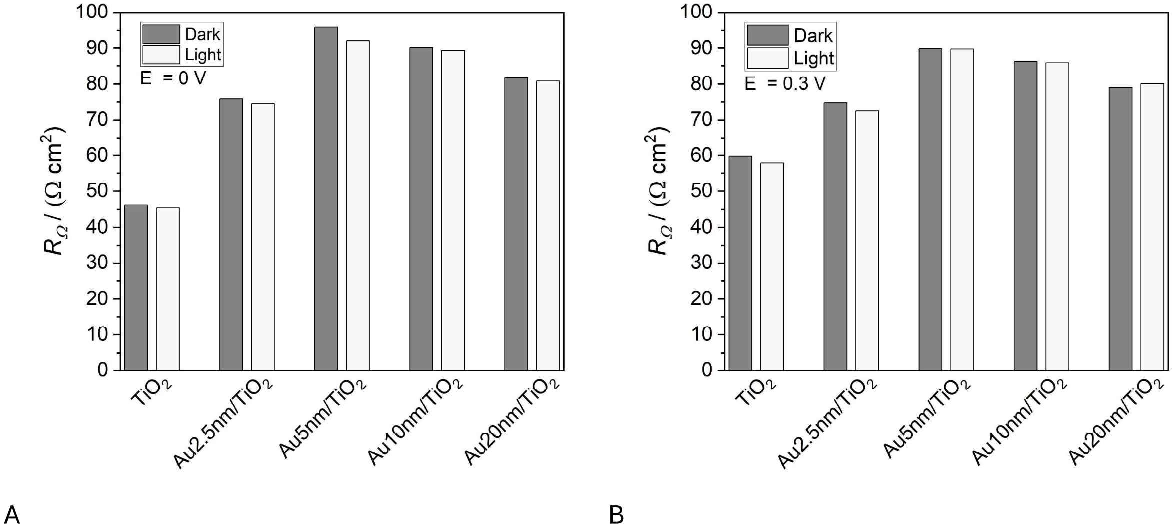

Figure 6.15 - Values of R_{Ω} recorded at 0V (A) and 0.3V (B) in $NaClO_4$ 0.1 M

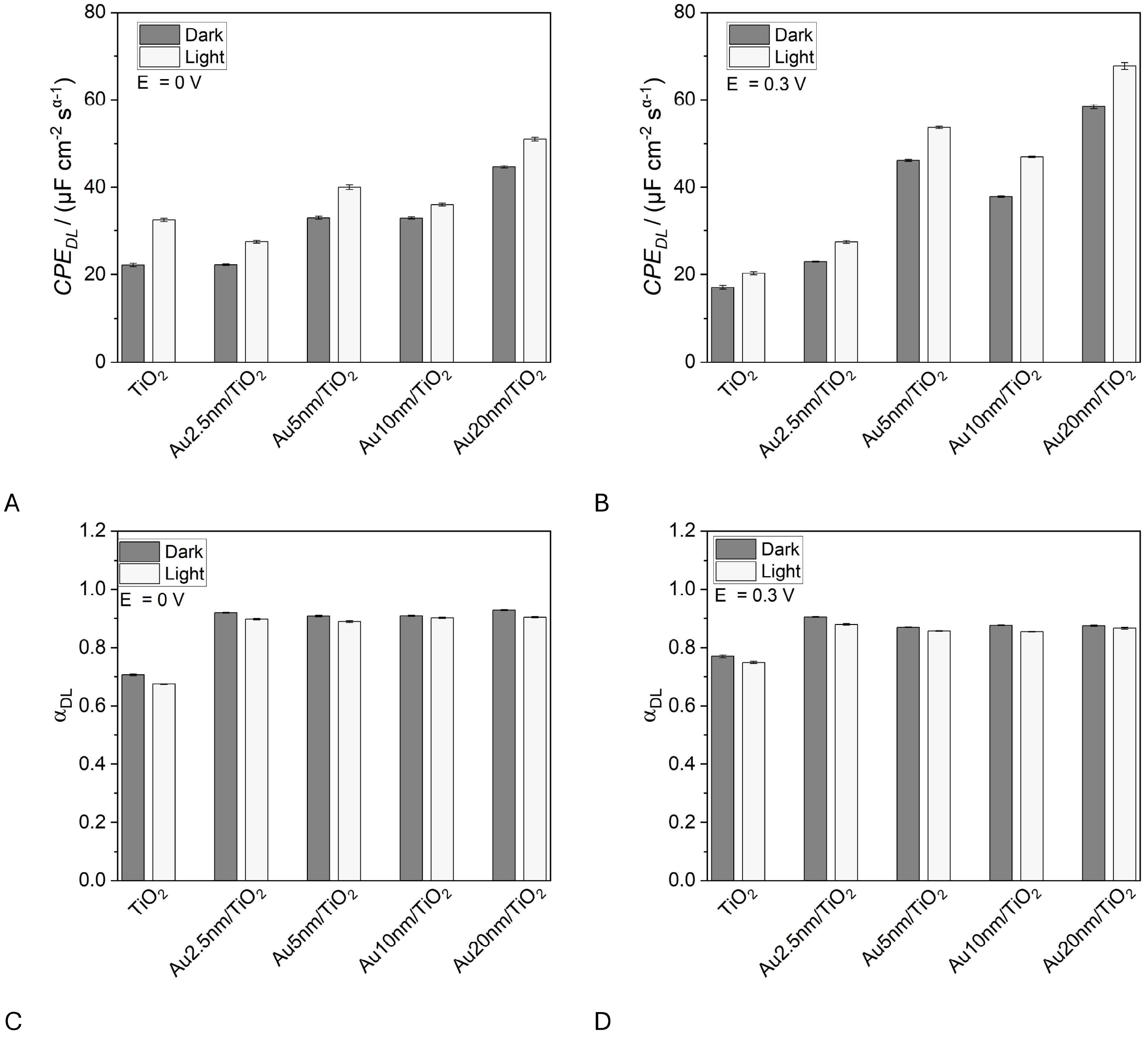

Figure 6.16 - CPE parameters recorded at 0V (A-C) and 0.3V (B-D) in $NaClO_4$ 0.1M

For all the samples, the value of the cell resistance remains very similar, and is not affected by the irradiation (Figure 6.15 A-B). The same is valid for the value of α_{DL}, which is expected as the material of the electrode remains unaltered (Figure 6.16 C-D). A trend can be observed for the value of CPE_{DL}, which increases upon irradiation due to the formation of new charge carriers in the material. It is also possible to observe that the value is higher for the electrodes prepared with more gold (Figure 6.16 A-B).

The value of R_{CT}, reported in Figure 6.17 clearly highlight that irradiation lead to a decrease charge transfer resistance and this trend is linear with the amount of gold in the sample.

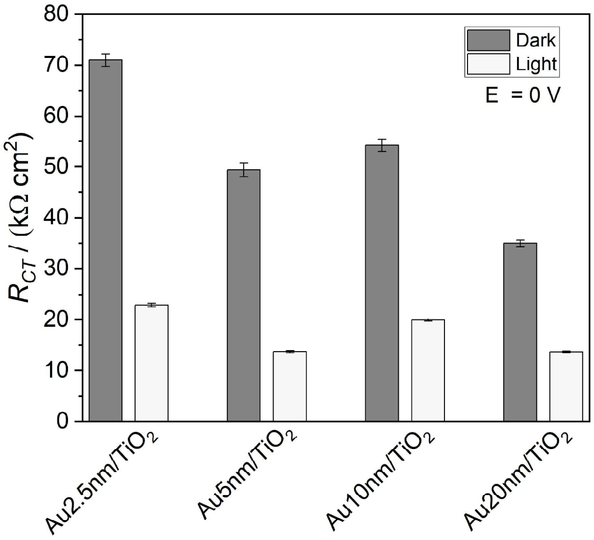

Figure 6.17 - Values of R_{CT} recorded at 0V in $NaClO_4$ 0.1M

An example of the obtained photocurrent is reported in Figure 6.18 A for a FTO glass slide covered with the thin film of TiO_2 under 395 nm LED irradiation.

Upon irradiation, charge separation is promoted and a peak can be observed in the amperogram. After a few seconds, electron and holes recombination lead to a stable value of stationary photocurrent. For all the tested samples, the first dark/light cycle lead to higher PEC values, possibly due to a cleaning of the TiO_2 surface that takes place when holes are formed and trapped at the TiO_2/solution interface.

By increasing the amount of gold content in the electrode, as shown in Figure 6.18 B, the value of photocurrent increases until a maximum value is achieved.

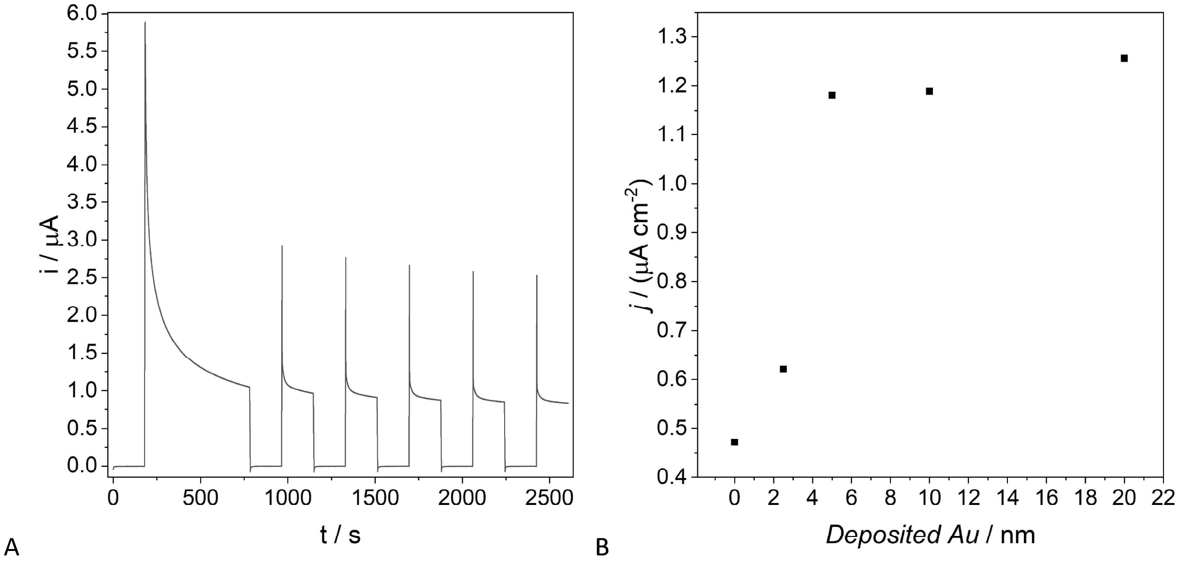

Figure 6.18 – (A) PEC response of a FTO/TiO_2 electrode at 0.1V vs SCE in $NaClO_4$ 0.1M under 395 nm LED irradiation. (B) Variation of stationary photocurrent intensity value with the amount of gold in the samples, recorded in in $NaClO_4$ 0.1M under 395 nm LED irradiation at 0.1V vs SCE

For all the tested samples, increasing the irradiation wavelength from 395 nm to 455 nm and 530 nm lead to a decrease in PEC intensity. This is expected, as the PEC activity is due to TiO_2, and the peak absorbance of TiO_2 is in the UV / near UV region.

An example of this is reported in Figure 6.19 (A) for the FTO/TiO_2 electrode. It is also clear from the recorded signal that the transient photocurrent decay is much faster at higher wavelength. The same behavior was observed in the samples with 5, 10 and 20 nm of deposited gold below the TiO_2 layer. An interesting difference arises when the sample prepared with the smallest nanoparticles (from the 2.5 nm film) was irradiated at 530 nm. In this case, the recorded signal was cathodic, as shown in Figure 6.19 B. This indicates that a different process is taking place, and is expected as the irradiation wavelength is close to the plasmon resonance peak of gold nanoparticles of 13.6 ± 0.7 nm.

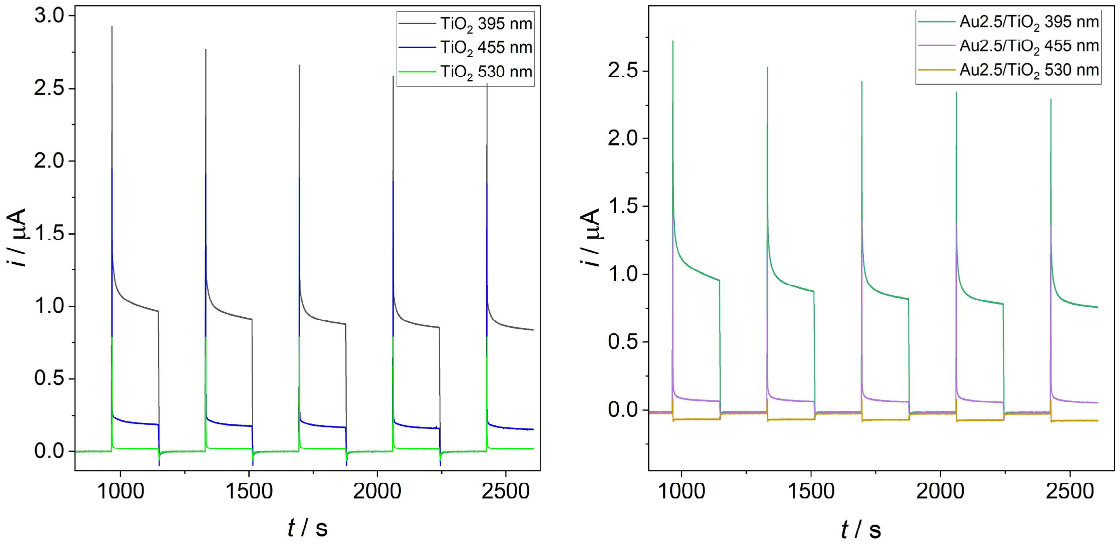

Figure 6.19 - (A) PEC recorded with a FTO/TiO_2 electrode at + 0.1V vs SCE in $NaClO_4$ 0.1M under LED irradiation.(B) PEC recorded with a FTO/TiO_2 electrode at + 0.1V vs SCE in $NaClO_4$ 0.1M under LED irradiation

The electron-hole recombination rates were also obtained by fitting the decay curve using OriginPro software. Three types of fitting were tested, with the following equations:

Equation 6.1 –

$$y = y_0 + A_1 e^{-x/t_1}$$

Equation 6.2 –

$$y = y_0 + A_1 e^{-x/t_1} + A_2 e^{-x/t_2}$$

Equation 6.3 –

$$y = y_0 + A_1 e^{-x/t_1} + A_2 e^{-x/t_2} + A_3 e^{-x/t_3}$$

When using a mono-exponential fitting (Equation 6.1), all the samples presented values between 8 and 20 s when irradiated at 395 nm, due to the charge separation happening in the TiO_2. No significant trend could be observed. At higher wavelengths, the value was always lower than 0.3 s.

Moving to a bi-exponential fitting (Equation 6.2) a first, fast decay could be observed followed by a second, slower one. It is worth mentioning that this equation has already been used in Chapter 3, but only the trend in the same batches of TiO_2 are considered, so no comparison of the obtained values will be made. This is related to the fact that the value of τ is highly dependent on the layer thickness and can vary significantly due to improved operator's ability to perform the dip-coating. Other environmental factors that could not be controlled (temperature and relative humidity) also influence the deposition, which is therefore considered "the same" only between samples of the same batch.

T1 was close to zero for all the samples except those containing high amount of gold (initial film thickness >= 5 nm). The latter presented values close to 5 s. As for T2, a more interesting trend was observed. As reported in Figure 6.20, TiO_2 only presented high value when irradiated at 395 nm. All the samples containing gold also presented a 15 s time when irradiated at 455 nm. This can be explained as the presence of gold nanoparticles increased the light absorbance in the visible light region of the spectra. The values of R^2 obtained for the bi-exponential fitting are higher than the values obtained for the mono-exponential one, suggesting that the model is more accurate.

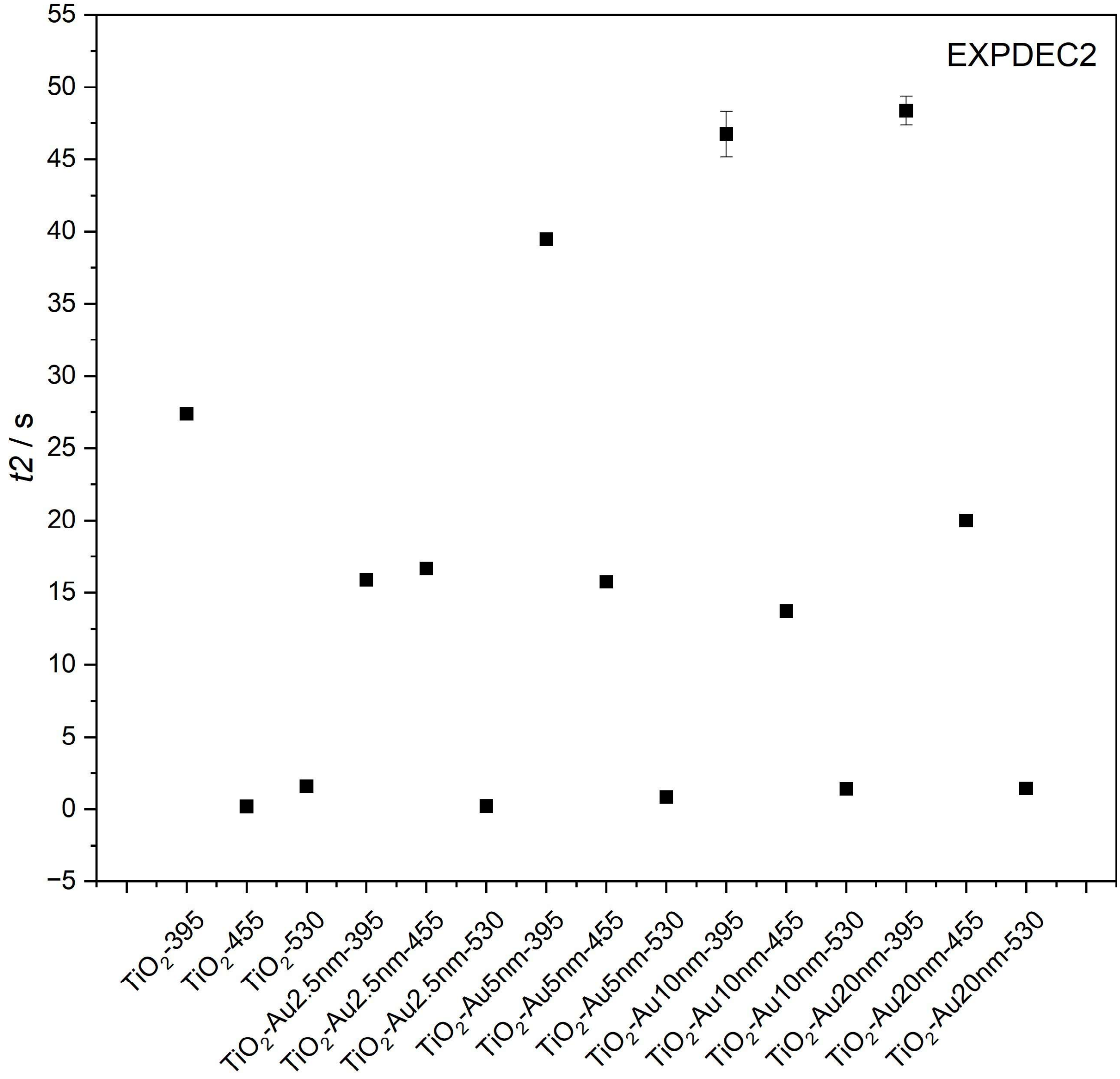

Figure 6.20 - t2 value for different electrodes at 395, 455 and 530 nm

The analysis of the tri-exponential fitting did not lead to significant results. The values of R^2 did not improve compared with the bi-exponential fitting. At 395 nm, T2 was higher than T1 for all the samples, while at other wavelengths no difference was observed. The values of T3 were higher for all the samples at all the wavelengths, but no trend was present, thus such plots were disregarded.

6.4 H_2O_2 Electrochemical detection

H_2O_2, as shown in Figure 6.21 A, cannot be effectively detected on a bare TiO_2 film. When a layer of gold nanoparticles is located below the TiO_2 layer, a significant signal increase can be observed upon H_2O_2 consecutive additions, as shown in Figure 6.21 B and C.

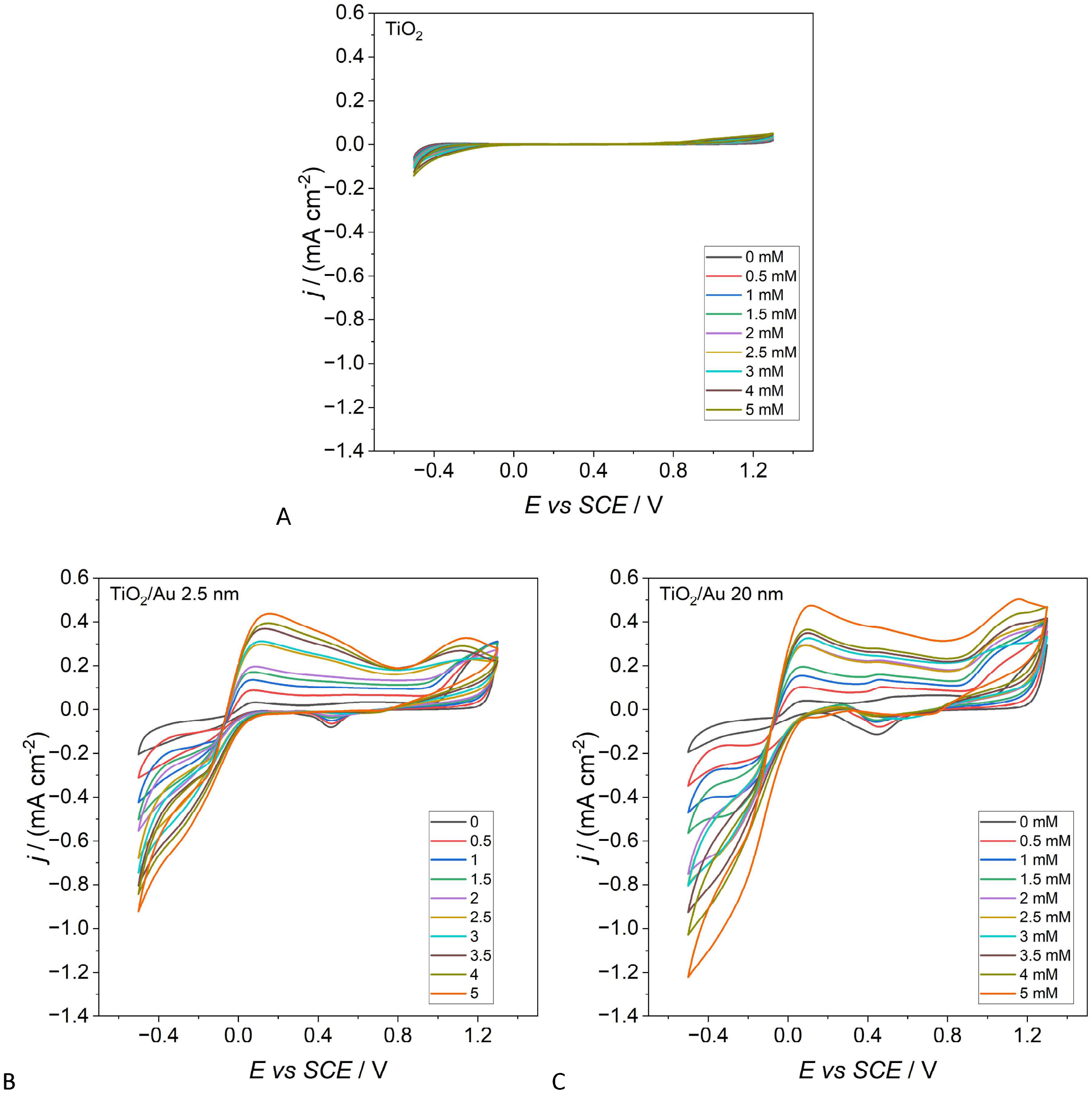

Figure 6.21 - Behavior of (A) TiO_2 and TiO_2 with small (B) and big (C) gold nanoparticles. Note that the graphs are reported with the same scale

All the materials show an increase of the cathodic current at -0.5V vs SCE. In addition, the electrodes containing gold nanoparticles also present two anodic peaks. The first one, located at +0.1 V vs SCE, can be quantified in the whole concentration range, while the latter, at + 1.2 V vs SCE, only appears at higher concentrations of H_2O_2. The sensitivity of the cathodic current of the three materials is compared in Figure 6.22 A and the anodic peak at +0.1V of the composite electrodes was also compared in Figure 6.22 B.

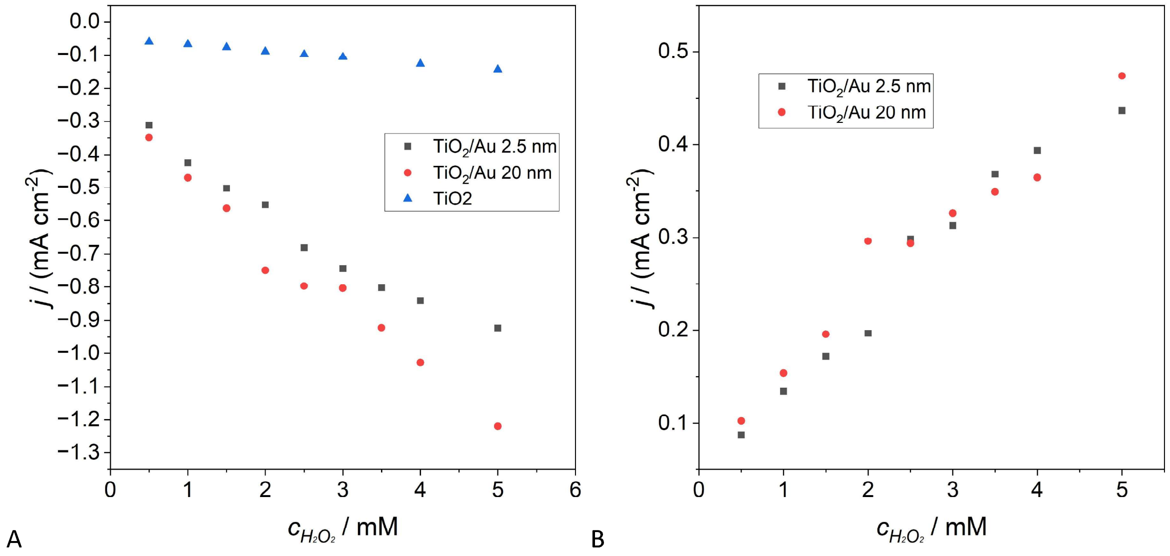

Figure 6.22 - Calibration plots obtained for different materials using the cathodic value at -0.5 V vs SCE (A) and the anodic peak at + 0.1V vs SCE

Interestingly, no significant difference could be observed when working with different amounts of sputtered gold under the TiO_2 layer. This suggests that the employing lower amount of gold could be more convenient.

If compared to the performances of gold nanoparticles on FTO without the TiO_2 layer, a clear trend is observed: The exposed gold leads to the highest sensitivity, TiO_2 alone does not detect the analyte and the composite material lays in the middle. For the comparison reported in Figure 6.23, the cathodic signal was selected although only exposed gold presented a peak, while the values of the other electrodes are the current recorded at the lower vertex potential of the CV scan.

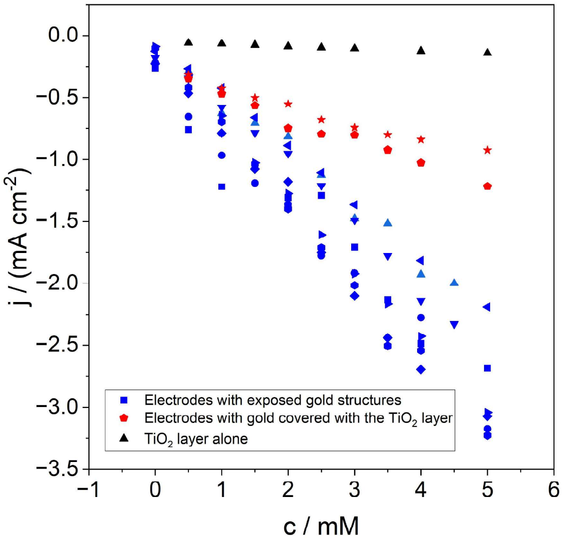

Figure 6.23 - Calibration plots of the cathodic signal for different electrodes. A clear trend could be observed for the three types of materials

6.5 H_2O_2 PEC detection

As previously mentioned, one of the advantages of a TiO_2 layer is its photoactivity. Thus photo-electrochemical response of the electrode in the presence of H_2O_2 was studied.

First, the behavior of a 2.5nmAu/TiO_2 electrode was analyzed at different values of applied potentials (Figure 6.24). As expected, when the sample is irradiated in absence of H_2O_2 (point a) the PEC signal is proportional to the applied potential. Additions of H_2O_2 were performed during the dark phase (point b) and lead to different observations. When working at the lowest applied potential (+ 0.1V vs SCE), a cathodic signal was observed, indicating that a reduction reaction was taking place instead of the expected photo-electrochemical oxidation. At + 0.3 V a weak, but clear, signal was present. At higher values (+ 0.5 V and + 0.9 V) a clear rise of current was recorded.

Upon irradiation, a transient photocurrent peak was present at all potentials. At + 0.1 V, the oxidation of H_2O_2 carried out by the photogenerated holes was able to reduce the intensity of the cathodic signal.

At + 0.3V and + 0.5 V, both an anodic transient photocurrent and stationary photocurrent were observed, significantly higher than the current values recorded during the dark phases.

At + 0.9 V, a peak for transient photocurrent was observed, but the presence of additional charge carriers did not influence the value of recorded current, with respect to the dark value. This is because at such high applied potential, most of the reaction is electrochemical and the presence of a relatively small number of photogenerated holes is negligible.

At potential equal or higher than + 0.3V, a cathodic peak was also recorded immediately after the LED was turned off. This phenomenon, known as overshoot, arises because when the flux of holes to the interface is immediately interrupted, the flux of electrons continues, driven by the remaining holes, until all those are consumed by recombination or charge transfer.

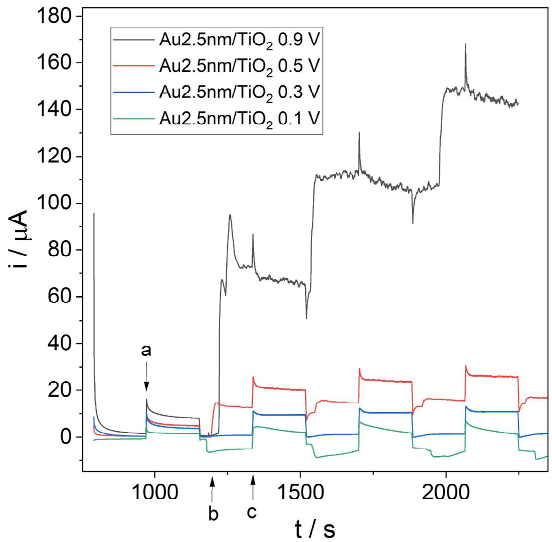

Figure 6.24 - PEC response recorded at 0.1, 0.3, 0.5 and 0.9 V vs SCE with a 2.5 nm dewetted gold electrode covered by TiO_2. (a) first light cycle; (b) addition of H_2O_2; (c) second light cycle

A choice was made to select + 0.3 V as the best potential to record a calibration plot. This allowed to obtain a good signal, while keeping a low potential, thus limiting tear of the electrode and the effects of possible interferents in solution. The recorded amperograms are reported in Figure 6.25.

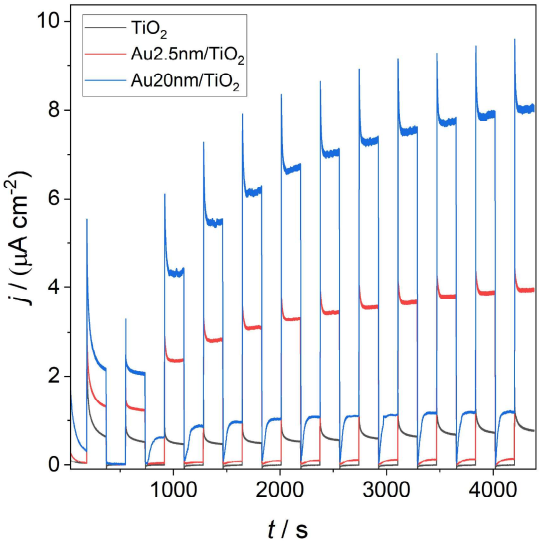

Figure 6.25 - Current recorded at + 0.3 V vs SCE in $NaClO_4$ 0.1 M solution with additions of H_2O_2 (from 0 mM to 0.5 mM)

For each electrode, three calibration lines were produced by measuring the maximum value of transient photocurrent, the value of stationary photocurrent and the plateau reached during the dark phase.

Two different linear ranges could be distinguished, one between 0 and 0.15 mM, present only for the samples containing gold, and the other between 0.2 and 0.5 mM. At higher concentration, saturation of the signal was observed.

The obtained values of sensitivity are reported in Figure 6.26, showing that the sensitivity in the lower range is higher than in the upper range for all the materials. TiO_2 alone could not detect H_2O_2 at + 0.3V without irradiation, while it was possible by the other samples thanks to the presence of gold. In all the tested cases, the sensitivity was proportional to the quantity of gold present in the sample.

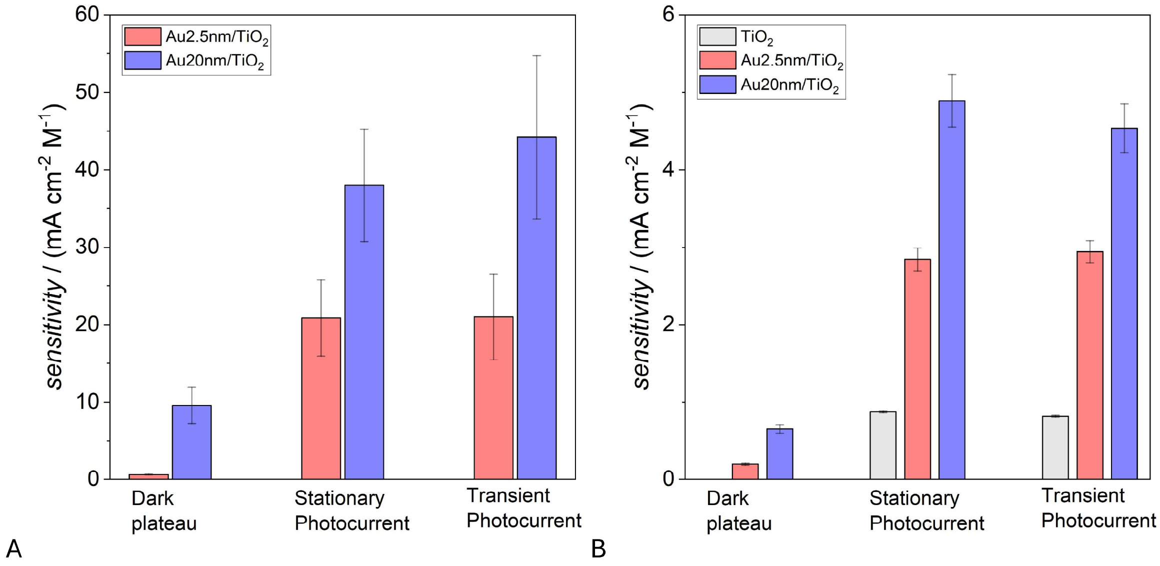

Figure 6.26 - Sensitivity values of the tested electrodes (A) in the range 0 - 0.15 mM and (B) 0.2 - 0.5 mM

Analysis of the electron–hole recombination kinetics for the Au/TiO_2 electrodes revealed that the addition of H_2O_2 to the solution led to a change in the photocurrent decay behavior from bi-exponential to mono-exponential. This is consistent with the known behavior of photoactive materials in the presence of efficient hole scavengers.[96,97]

The initial bi-exponential decay indicates the presence of two dominant recombination processes: a faster component, likely associated with bulk recombination or surface trap-assisted recombination, and a slower component, attributed to hole accumulation and their reaction with adsorbed water molecules. The transition to a mono-exponential decay upon addition of H_2O_2 suggests that one recombination pathway is now dominant, while the others have either been suppressed or proceed on a timescale too fast to be resolved.

In the presence of H_2O_2, photogenerated holes that would otherwise be trapped at surface defects or slowly oxidize water are rapidly scavenged. This efficient hole removal suppresses the slower recombination component, simplifying the decay kinetics to a predominantly single-process behavior.

7 Hybrid Ag/TiO_2 electrodes

In previous chapters the advantages of combining metal structures and a TiO_2 layer were presented. The possibility of exploiting both their synergistic activity and their specific catalytic properties for analyte quantification were tested.

In this chapter, a bimodal cetirizine sensor is proposed. It is based on silver structures covered by titanium dioxide and can combine the detection via photoelectrochemical (PEC) oxidation and electrochemical reduction, employing for both the same experimental setup. In PEC, the excitation source (external irradiation) is physically separated from the recording device, and this allows to obtain better signal-to-noise ratio. Interestingly, no sensors were found in the literature exploiting either PEC for oxidation of cetirizine or electrochemical reduction. The proposed sensor also exploits titanium dioxide photo-renewable surfaces to achieve anti-fouling properties and to increase the overall lifetime of the device.[6–8]

7.1 Electrode Preparation and Characterization

The electrodeposited structures of silver on fluorine-doped tin oxide (FTO) electrodes were characterized by SEM imaging before the deposition of the TiO_2 layer. As shown in Figure 7.1 A-B, two clearly different morphologies could be obtained: spheres present a diameter of 1 μm and dendrites are formed by a longer needle-like structure between 1 and 3 μm with smaller branches of less than 1 μm. After the deposition of the semiconductor, SEM images revealed a uniform cover of the electrode, but it was no longer possible to distinguish between the undelaying silver morphologies due to the high thickness of the deposited layer, which is known from previous works to be approximately 100 nm with a surface roughness of (8.6±0.9) nm (Figure 7.2). [38]

UV-VIS spectra of the assembled electrodes were recorded using an integrating sphere. As shown in Figure 7.1C, the transmittance clearly changes as the amount of the deposited silver is higher for the dendritic structure. This is in agreement with the deposited charge recorded during the electrodeposition, $(0.0214 \pm 0.0005)\ C\ m^{-2}$ for silver spheres and $(0.26 \pm 0.08)\ C\ cm^{-2}$ for silver dendrites.

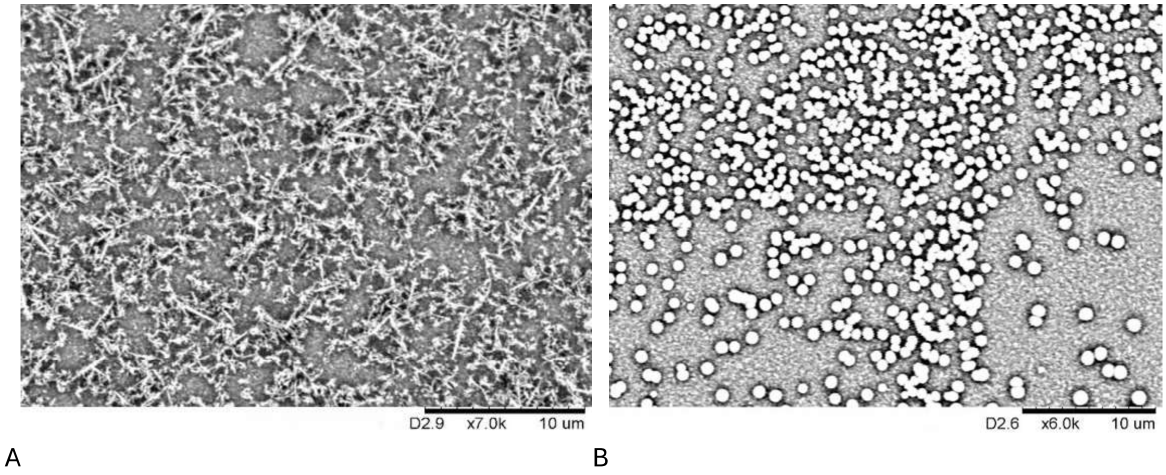

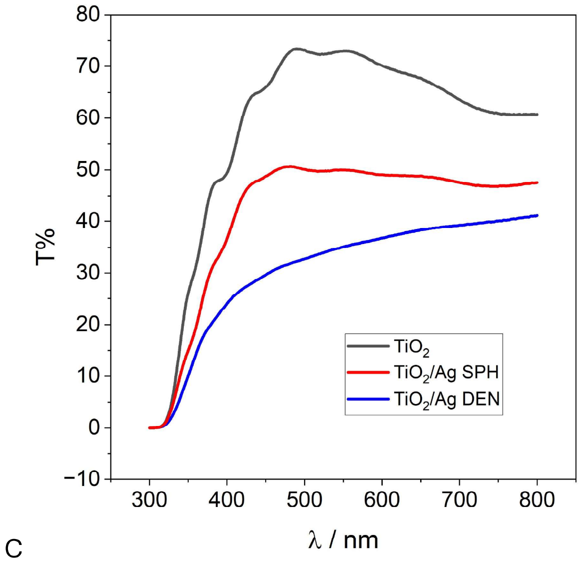

Figure 7.1 - SEM images of silver dendrites (A) and spheres (B) before TiO_2 layer deposition and UV trasmittance specta of the assembled devices (C)

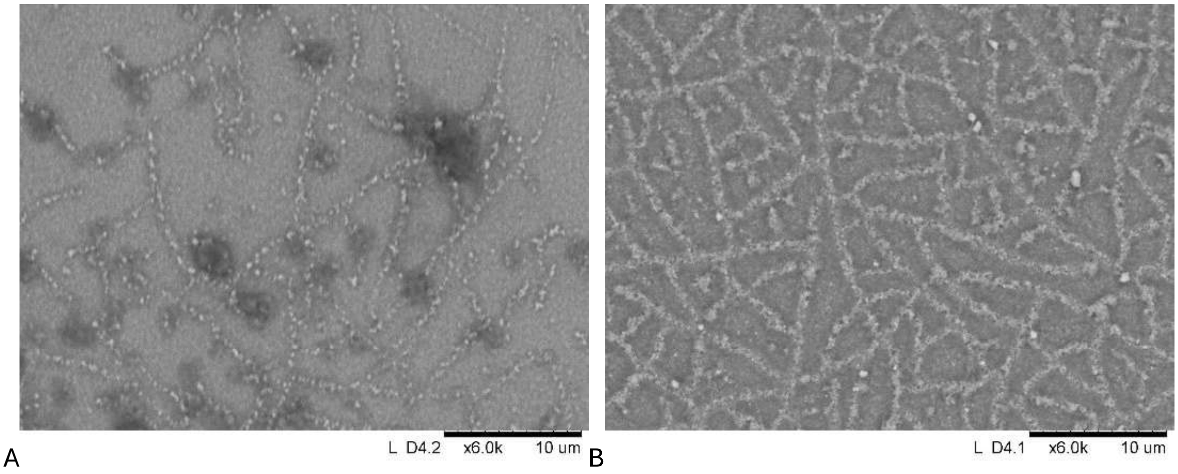

Figure 7.2 - SEM image of a TiO_2/AgDEN electrode (A) and TiO_2/AgSPH electrode (B)

Cyclic voltammetry, recorded in presence of 3 mM potassium ferrocyanide, highlighted the difference between the TiO_2 layer deposited on FTO and the electrodes where silver structure were also present (Figure 7.3 A). Furthermore, the electrodes prepared with silver spheres and those prepared with silver dendrites presented a different shape especially in the anodic region. In particular, dendrites show a multi-peak signal, probably due to a less homogeneous structure with different morphologies. A further difference between the two structures covered with TiO_2 was highlighted by diffusion studies conducted with ferricyanide probe at different scan rates. As reported in Table 7.1, the electrodes behaved significantly differently, showing for silver spheres the log(*j*) vs log(*v*) slope higher than 0.5, typical of particles more diffusionally accessible.[98]

Samples	**Log (j) vs Log (v)**	**j vs $\sqrt{v}$**
TiO_2/Ag spheres	1.11 ± 0.07	0.0130 ± 0.0008
TiO_2/Ag dendrites	0.5 ± 0.1	0.011 ± 0.002
TiO_2	0.184 ± 0.003	0.049 ± 0.003

Table 7.1 - Characterization of TiO_2/Ag electrodes in $K_4[Fe(CN)_6]$

The effect of silver structure can also be observed via electrochemical impedance spectroscopy: in particular, the charge transfer resistance of the electrode decreases drastically when conductive silver structure are used below the TiO_2 layer - from (37 ± 3) kΩ cm^2 to (0.6 ± 0.1) kΩ cm^2 (Ag SPH) and (0.45 ± 0.03) kΩ cm^2 (Ag DEN) (Figure 7.3 B).

The behaviour of the three electrodes upon 395 nm LED irradiation also presents a clear trend: TiO_2 leads to the highest photocurrent while the presence of silver structures decreases such value. The current intensity was inversely proportional to the total amount of electrodeposited silver (Figure 7.3Figure 7.3 - (A) CV curves recorded in NaClO4 0.1 M in presence of 3 mM $[Fe(CN)_6]^{3-/4-}$ (B) EIS recorded in NaClO4 0.1 M at + 0.25 V and (C) Photocurrent recorded at + 0.1V vs SCE under intermittent 395 nm LED irradiation

C), as only part of the (photo)generated electrons travel through the external circuit, while others are used to reduce the naturally oxidizing Ag^+ ions to the metallic state.[39]

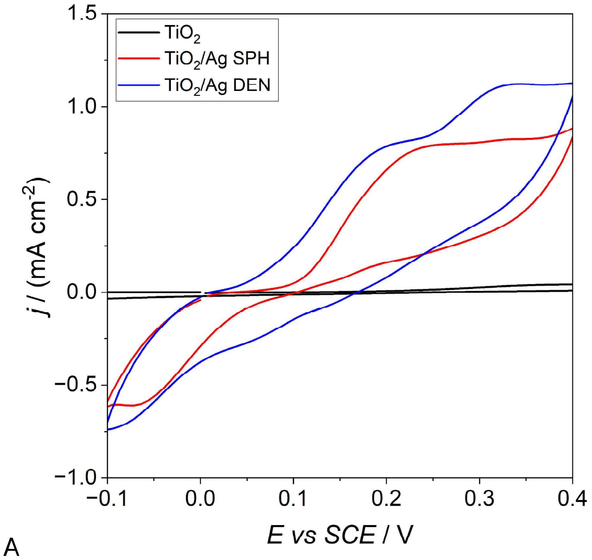

A

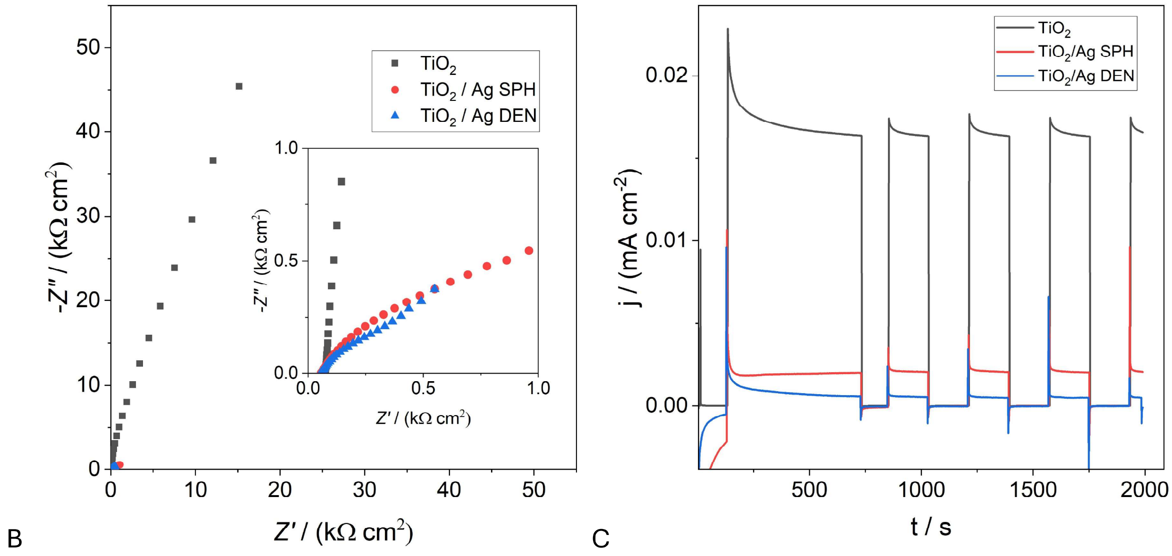

Figure 7.3 - (A) CV curves recorded in $NaClO_4$ 0.1 M in presence of 3 mM $[Fe(CN)_6]^{3-/4-}$ (B) EIS recorded in $NaClO_4$ 0.1 M at + 0.25 V and (C) Photocurrent recorded at + 0.1V vs SCE under intermittent 395 nm LED irradiation

7.2 Photo-Electrochemical oxidation of Cetirizine

Cetirizine was initially detected via PEC oxidation, working at + 0.1 V vs SCE and using a 395 nm LED as light source. The potential is maintained at + 0.1 V since the value of the photocurrent is high enough to assure the detection of CTZ and the possible interferences are minimized.

The analyte was added in a standard electrochemical cell during the “dark phase” of the chopped illumination cycle, and the current intensity was evaluated using the stationary photocurrent 3 minutes after irradiation. No drift of the baseline can be observed, suggesting that the low applied voltage is not enough to effectively oxidize the molecule, while an increase in the photocurrent signal can be observed after CTZ additions (Figure 7.4 A).

The photocurrent values were used to produce a calibration plot (reported in Figure 7.4 B), where two linear ranges could be observed, from 0 to 5 µM and from 8 to 18 µM. During the study, attention was focused on the lower linear range, which presented the highest slope and good linearity and the sensitivity of the three electrodes were compared (Figure 7.4 C).

Bare TiO_2 presented the highest slope, while the change of current was negligible when increasing analyte concentrations were tested with the dendrite-based electrode. This was expected as the photo-electrochemical oxidation current was the lowest for this sample. Interestingly, the electrode prepared with spheres, containing a lower quantity of silver, presented a good sensitivity being also the best candidate for the reductive dehalogenation of the target molecule.

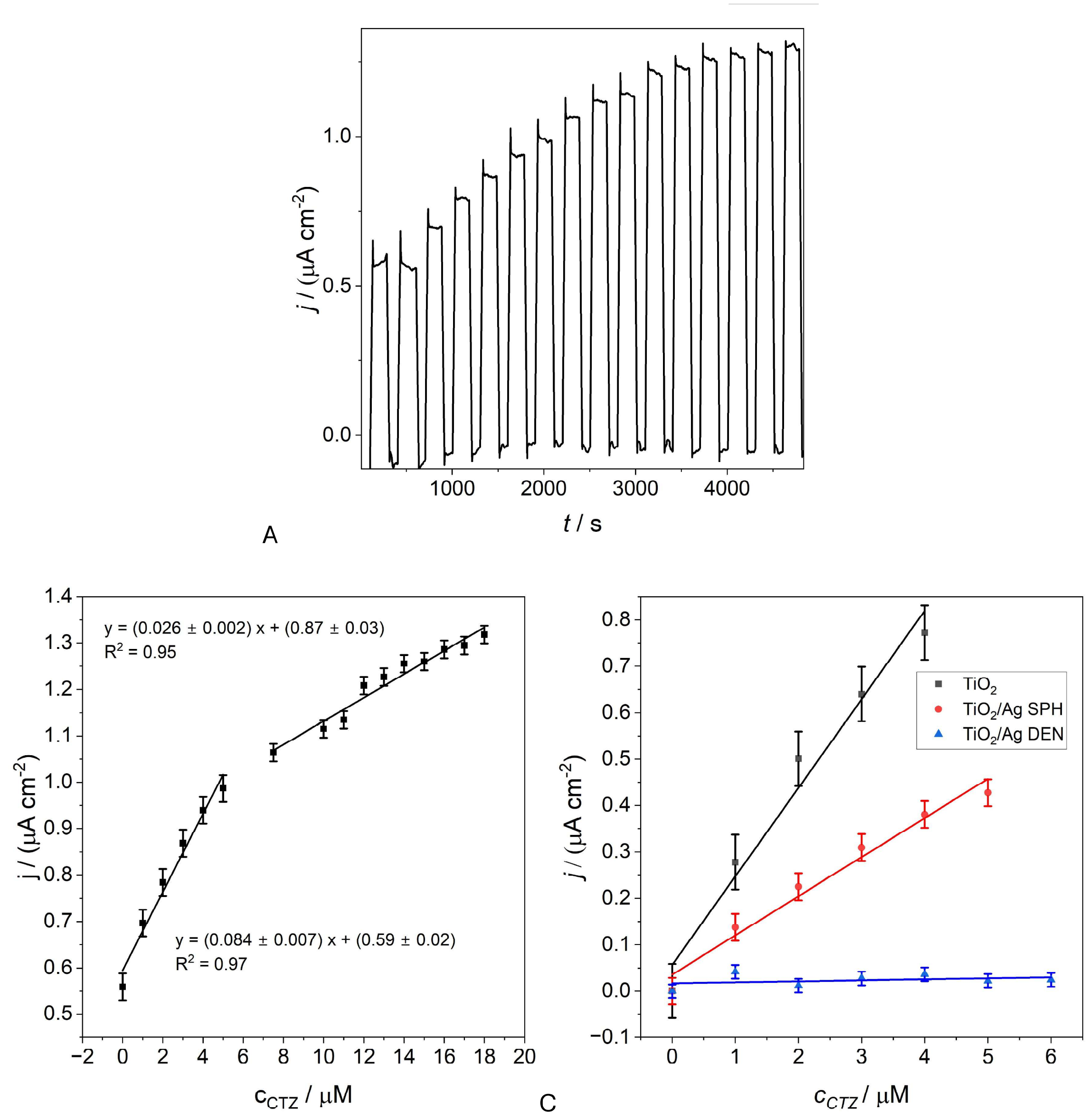

Figure 7.4 - (A) Example of photocurrent change with consecutive additions of cetirizine and (B) complete calibration plot for TiO2/Ag SPH electrode. (C) Comparison of the performances of the different electrodes in the selected concentration range towards CTZ determination: TiO_2 (0.19 ± 0.02) μA cm^{-2} μM^{-1}, TiO2/Ag SPH (0.084 ± 0.007) μA cm^{-2} μM^{-1}, TiO2/Ag DEN (0.002 ± 0.002) μA cm^{-2} μM^{-1}

7.3 Electrochemical Reduction of Cetirizine

The cathodic region where the reduction peak could be observed for the electrode TiO_2/SPH was identified via CV (Figure 7.5 A) and, in order to improve the detection limit, Differential Pulse Voltammetry (DPV) was recorded with consecutive cetirizine additions (Figure 7.5 B). DPV operating parameters were carefully optimized (see experimental section) and nitrogen purge was used to obtain a clearer signal.

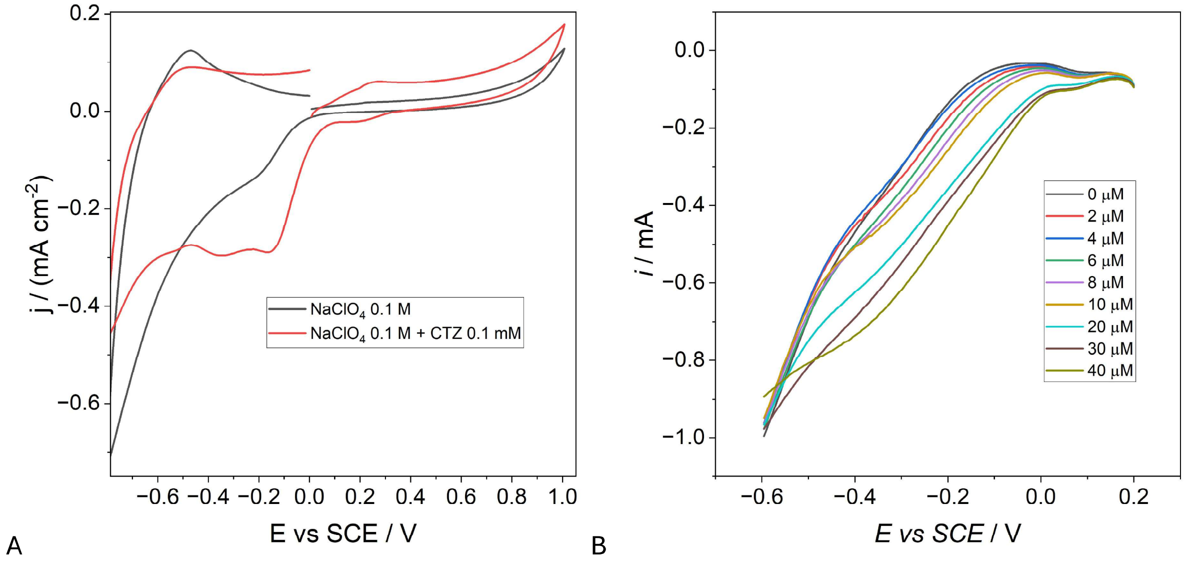

Figure 7.5 – (A) CVs recorded with and without addition of cetirizine and (B) DPV recorded with consecutive additions of CTZ

Upon background subtraction, a clear trend could be observed as reported in Figure 7.6 A. The area of the peaks was used to plot a calibration line, reported in Figure 7.6 B. Interestingly, such trend was not observed when working with the dendritic structure, probably due to the more fragmented metal structure, and as expected when working with the bare TiO_2 electrode, for the absence of the metal.

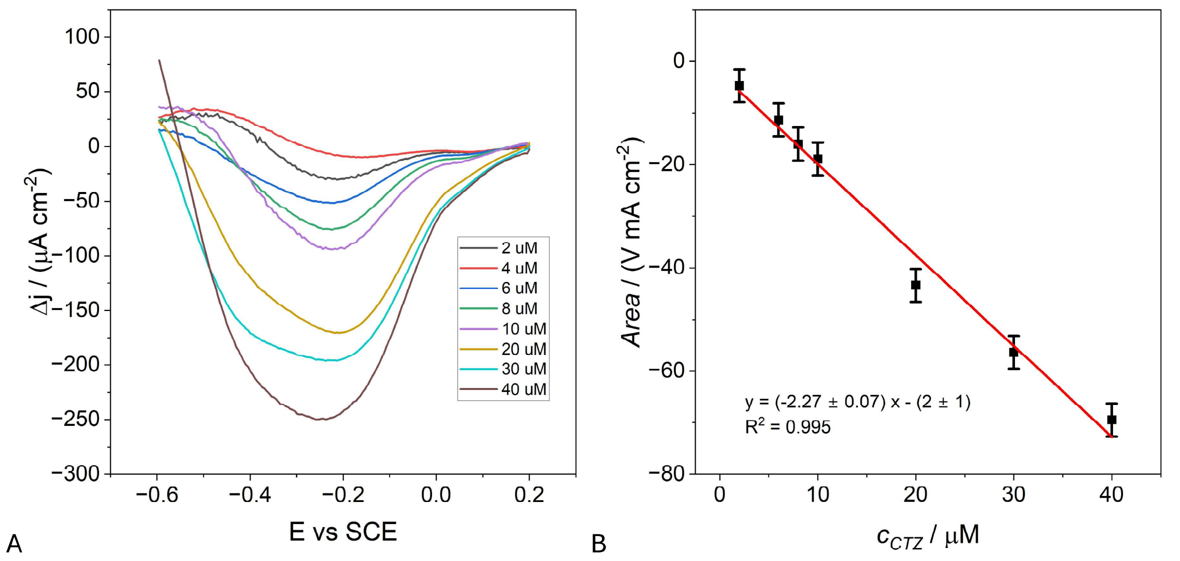

Figure 7.6 - (A) DPV curves (background subtracted) of cetirizine consecutive addition in NaClO4 0.1M and (B) corresponding calibration plot

7.4 Data analysis

The analytical parameters of the bimodal sensor are reported in Table 1. The LOD (3σ/S) are very similar, being (1.03 ± 0.08) μM and (3.2 ± 0.1) μM for PEC oxidation and EC reduction, respectively. The small difference can be caused by the better signal-to-noise ratio of PEC analysis and by the possible fouling of the silver during the reductive dehalogenation. LOQs (10σ) follows the same trend and the apparent recovery factors are satisfactory for both techniques, being very close to 100 %.

Table 1. Analytical parameters of the prepared FTO/Ag(sph)/TiO_2 electrode with two different techniques.

	PEC Oxidation	DPV Reduction
LOD / μM	1.03 ± 0.08	3.2 ± 0.1
LOQ / μM	3.4 ± 0.3	10.7 ± 0.3
Apparent recovery factor	103.2 %	97.2 %
Sensitivity	0.084 ± 0.007 μA cm^{-1} μM^{-1}	2.27 ± 0.07 V mA cm^{-2}

7.5 Interferents

To validate the concept of a bimodal sensor, interferents study and real sample analysis were performed. Paracetamol, diclofenac, ascorbic acid, and inorganic ions as Mg^{2+}, K^+, SO_4^{2-} and PO_4^{3-} were not detected with the bimodal device (Figure 7.7), both in EC and PEC determination. In particular, attention was focused on glycerol, as it is present at high concentration in many commercial formulations of cetirizine, such as Cetirizina Pensa®. As shown in Figure 7.8 A, when working with the photo-electrochemical oxidation it was possible to detect the presence of glycerol, even though the sensitivity was much lower compared to that toward cetirizine. With that technique glycerol could be thus considered an effective interferent species. On the other hand, analysis in DPV were not able to detect glycerol. A direct comparison of the results obtained with the two techniques can give better understanding of the phenomena that are observed in the solution.

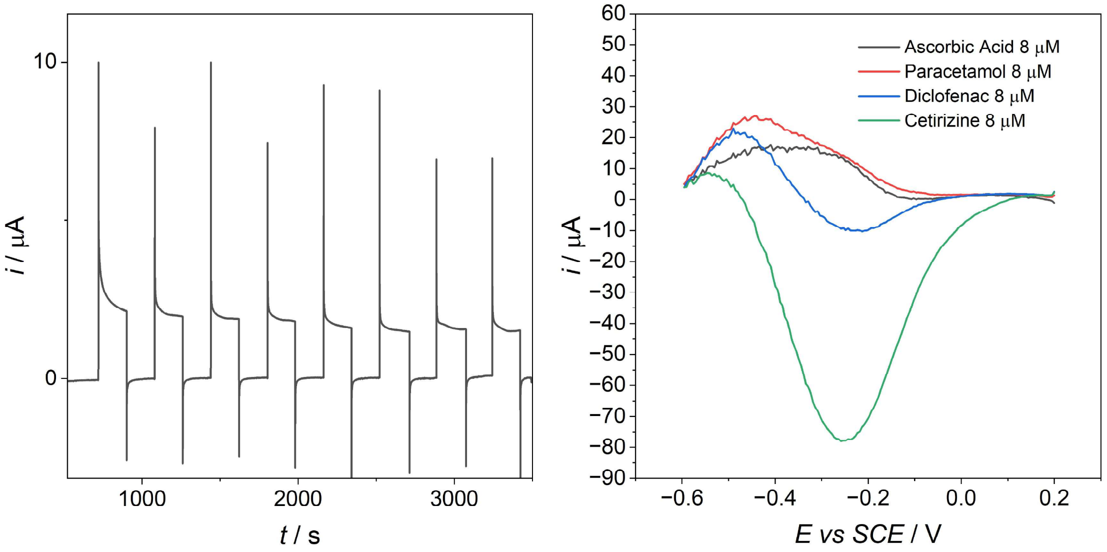

Figure 7.7 - Interferents test (PEC on the left and DPV on the right). In PEC, the reported cycles are: background (3x), K_3PO_4 80 µm, $MgSO_4$ 80 µm, Ascorbic acid 8 µm, paracetamol 8 µm, diclofenac 8 µm

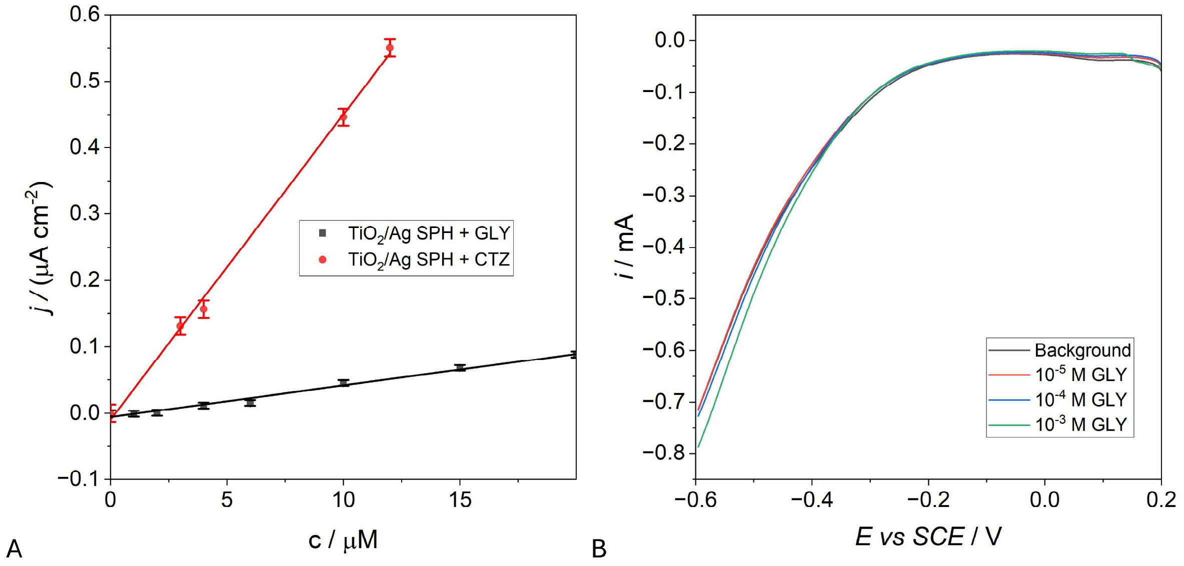

Figure 7.8 - (A) PEC-oxidation conducted at + 0.1V vs SCE with 395 nm LED irradiation and (B) DPV measurements with glycerol in NaClO$_4$ 0.1 M

7.6 Advantages of the combined electrode

The usage of the two materials combined in the same device leads to specific advantages compared to the use of two different electrodes. As reported in previous works[38], the presence of a physical layer of TiO$_2$ above the deposited metal plays an important structural role, preventing the loss of silver in solution and mechanical damages of the surface. No tests were conducted with exposed silver structures, as they were lost in solution before being able to collect significant data (Figure 7.9).

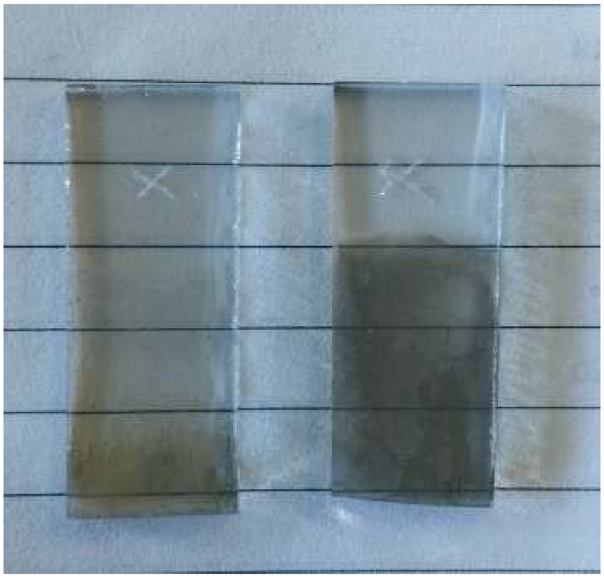

Figure 7.9 - Electrodes of uncovered Ag structures after the electrochemical test (left) and comparison with a freshly prepared one (right)

On the other hand, photoactivity of the TiO_2 layer can also be used to improve the lifetime of the sensor. Upon irradiation, electrons and hole are generated. The holes migrate toward the electrode-solution interface and can be used to oxidize adsorbed molecule present on the electrode's surface. This allows to restore the background signal after tests, limiting electrode fouling as reported in Figure 7.10 A. In order to achieve such result in only one hour, a more powerful 500W UV lamp was used as light source.

Photogenerated electrons also play an important role in restoring the electrode performances, as they can reduce the naturally occurring silver oxide to metallic silver. This process can be followed via CV (Fig. 6B) by observing the increase of the Ag oxidation peak and via EIS (Fig. 6C), checking the reduction of the electrode's resistivity after 1 hour of irradiation, from (8.00 ± 0.05) kΩ cm^2 to (4.22 ± 0.08) kΩ cm^2.

Interestingly, the literature focuses on the oxidation of the molecule but no data were found about cetirizine electroreduction (Table 2) and no bimodal detection was proposed. Moreover, although the LODs in this work are higher than other studies, they remain in the range of many pharmaceutical compounds. Finally, the CTZ potentials for the bimodal techniques are much lower than all the other electrodes, which represents an undoubted advantage both for the least damage to the electrode and for the least possibility of interferences.

Table 2. List of other works focusing on the detection of Cetirizine.

Material	Technique	LOD / µM	Linear Range µM	CTZ potential /V	Ref
PLMCNTPE [a]	CV ox	0.17	5-50	+ 0.75 vs SCE	73
PMO/CNTPE [b]	CV ox	0.076	2-45	+ 0.75 vs SCE	74
Ag-TiO_2-MWCNTs/CPE	SWV ox	0.00876	0.3 - 3	+ 0.71 vs SCE	77
CHO-GO/CPE [c]	SWV ox	0.009	0.1 – 3	+ 1.06 vs SCE	75
ZnO-Gr/CPE [d]	DPV ox	0.028	0.05 – 4	+ 1.16 vs SCE	76
p.GP [e]	SWV ox	0.16	0.5 - 25	+ 0.96 vs SCE	72
TiO_2/Ag	PEC ox	1.03 ± 0.08	0 - 6	+ 0.1 vs SCE	This work
	DPV red	3.2 ± 0.1	0 - 40	-0.25 vs SCE	This work

[a] Poly(L-Leucine) layered carbon nanotube paste electrode. [b] Poly (methyl orange) Modified Carbon Nanotube Paste Electrode. [c] Graphene oxide/cholesterol nanohybrids. [d] Zinc Oxide–Graphene Nanocomposite. [e] Pretreated graphite pencil.

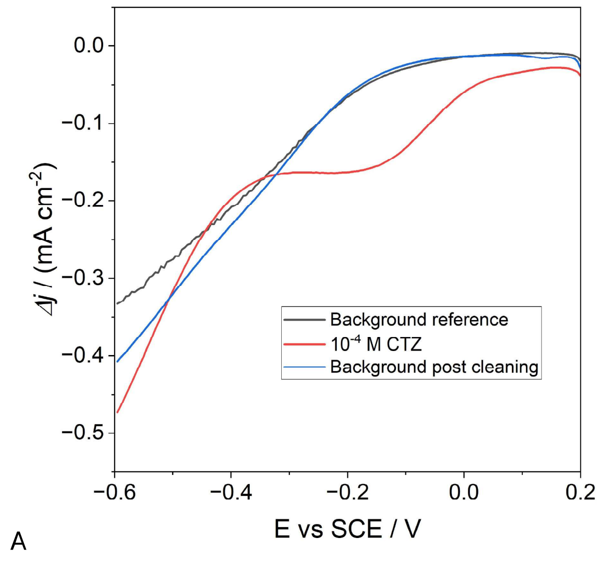

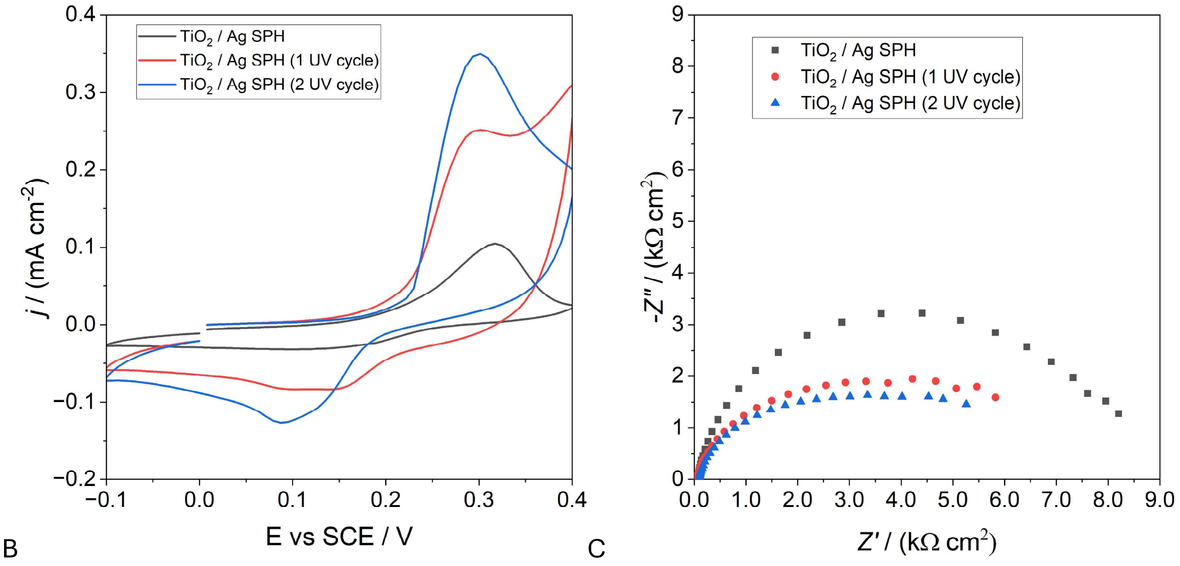

Figure 7.10 - (A) Cleaning of the electrode's surface upon irradiation – CVs recorded in NaClO4 0.1 M; (B) CV and (C) EIS highlighting the effect of 500W 365 nm UV irradiation on the metallic silver content and resistance of the device. Tests recorded in NaClO4 0.1 with 3 mM [Fe(CN)6]3-/4-, EIS recorded at + 0.25 V vs SCE

7.7 Conclusions

In this chapter, a bimodal device capable of exploiting its components for both photo-electrochemical oxidation and electrochemical reduction analyzed on the same analyte molecule was tested. The presence for TiO_2 was essential for the PEC oxidation and the semiconductor photoactivity was responsible for such process. Silver structures, on the other hand, allowed to obtain the electrochemical reduction of the molecule due to their catalytic properties. The presence of both materials lead to a synergistic effect, not only allowing to perform both the measurements with a single device and the same experimental setup, but also to obtain a more stable and reusable electrode. The obtained analytical parameters are satisfactory for both techniques. The comparison of the results allows to achieve better reliability, eliminating the effect of specific interferents (glycerol) that would affect only one of the two analytical techniques used.

8 Conclusions

This research work began with a systematic investigation of the properties and behavior of titanium dioxide (TiO_2) thin films, with particular emphasis on their synthesis and photo-electrochemical (PEC) characterization. The initial phase involved preparing a sol using titanium isopropoxide as the precursor, which was then subjected to controlled aging over various time intervals. Experimental results demonstrated a clear correlation between the aging duration of the sol and the performance of the resulting TiO_2 film. Specifically, a 14-day aging period yielded the most favorable outcomes, including enhanced surface coverage and a significantly stronger photocurrent response.

To further explore the functional versatility of the TiO_2 film, the film was modified by incorporating gold nanoparticles (AuNPs) synthesized via wet chemical methods. This modification aimed to evaluate how the presence of metallic nanostructures could influence the electrochemical and sensing capabilities of the device. It became evident that the TiO_2 layer played a crucial role in stabilizing the gold nanoparticles, which otherwise exhibited poor retention and rapid dissolution in solution. The protective TiO_2 coating not only preserved the integrity of the gold structures but also contributed to a marked improvement in the device's sensing performance, particularly when compared to the unmodified TiO_2 film. Ciprofloxacin, a wide range antibiotic was selected as target analyte and cloud be detected with good sensitivity even in the presence of various interferent.

As nanoparticles proved to play a key role on device performance, the study progressed to investigate alternative fabrication techniques for producing metal nanostructures. Wet synthetic methods, while commonly used, were found to suffer from several limitations: low structural stability, poor control over spatial distribution, and complex, multi-step procedures involving numerous chemical reagents. To address these drawbacks, a purely physical approach—solid-state dewetting—was proposed and implemented. In this method, a thin metallic film was sputtered onto a conductive substrate and subsequently annealed to induce the formation of nanoparticles with uniform size and spacing. The diameter of the resulting nanoparticles could be finely tuned by adjusting the initial thickness of the deposited metal layer.

To further understand the interplay between TiO_2 and metal nanoparticles, a TiO_2 layer was deposited on top of the dewetted gold nanostructures. This configuration led to a noticeable decrease in electrochemical sensitivity, a result that aligned with expectations given TiO_2's insulating behavior under certain conditions. However, the inclusion of TiO_2 introduced additional functional properties, most notably its intrinsic photoactivity. This characteristic was harnessed to enable photo-electrochemical detection of H_2O_2, demonstrating that the same device could be used to quantify the analyte through two distinct mechanisms—electrochemical and photo-electrochemical. This dual-functionality concept is referred to as bimodality.

Building on this bimodal approach, a new device was developed using TiO_2 in combination with silver nanostructures. The objective was to evaluate how substituting gold with silver would influence the device's behavior and to test the feasibility of bimodal sensing in a context closer to real-world application. In this configuration, TiO_2 was essential for enabling PEC oxidation, leveraging its semiconductor properties and photoactivity. Silver, on the other hand, facilitated the electrochemical reduction of the target molecule due to its well-known catalytic properties.

The integration of both materials resulted in a synergistic effect. Not only did this allow for both PEC and EC measurements to be conducted using a single device and unified experimental setup, but it also led to improved electrode stability and reusability. The analytical parameters obtained—such as sensitivity, limit of detection, and reproducibility—were satisfactory for both techniques. Moreover, the ability to cross-validate results from two independent detection modes enhanced the reliability of the measurements. This dual-readout strategy proved particularly effective in mitigating the impact of specific interferents, which would otherwise compromise the accuracy of one technique while leaving the other unaffected.

9 Appendix 1 - Techniques

During this Thesis' work, many techniques played an important role for the investigation of the electrodes' material properties. While the experimental parameters will be presented in details at the end of the thesis, a brief introduction on the working principle for these techniques will now be presented.

9.1 Cyclic voltammetry

Cyclic voltammetry (CV) is a powerful and popular electrochemical technique commonly employed to investigate the reduction and oxidation processes of molecular species.[99] It is particularly useful to determine the location of the redox potential of the electroactive species.

The electrochemical setup used for this technique is a classical three-electrode cell consisting of a Reference Electrode(RE), Counter Electrode (CE) and Working Electrode (WE, as reported in Figure 9.1 A. Most analysis performed during this work did not require to operate in degassed solutions, so a standard 50 mL beaker was used to contain the electrodes. The general scheme of a potentiostat is reported in Figure 9.1 B.[100]

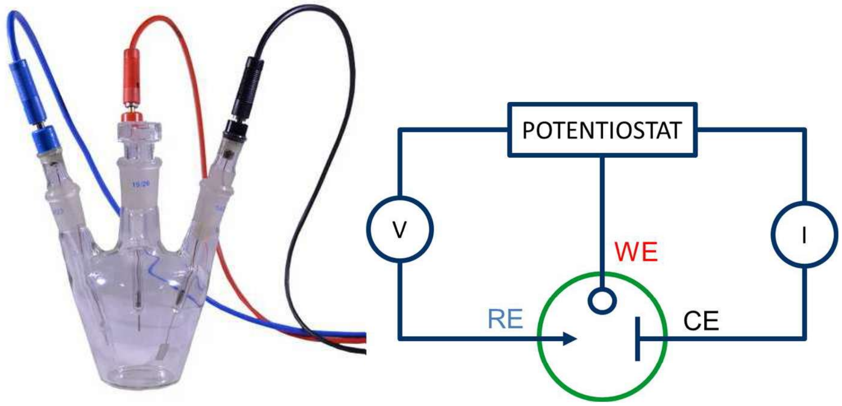

Figure 9.1 – (A) Three electrode setup for cycling voltammetry and (B) general scheme of a potentiostat

During the analysis, the potential is varied between the WE and RE with a triangular waveform, as reported in Figure 9.2, inset. The extremes of the potential range are commonly referred as upper and lower vertex potential. The current flow between the WE and CE is recorded.

If no reaction takes place in the selected range, a rectangular shaped voltammogram is obtained. It is due to the phenomena of charging and discharging of the surface, e.g. the capacitance of the system. When a reaction takes place, a corresponding peak can be located. As shown in Figure 9.2, the shape of such peak can give interesting information on the nature of the electron transfer process, like its electrochemical reversibility.[101]

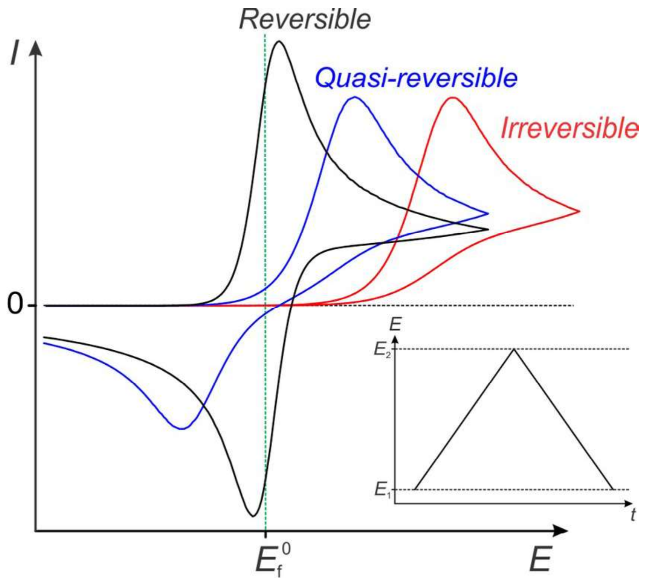

Figure 9.2 - A comparison of CV wave-shapes for reversible, quasi-reversible, and irreversible electron transfer process with the same formal potential, Ef0, on a macro-disk electrode (where planar diffusion dominates). The inset shows the triangular potential "ramp" applied to the working electrode during measurement

The CV shape is influenced by reagent concentration, number of exchanged electrons, electrode's surface and diffusion coefficient of the reagent.

As for the diffusion processes from the bulk of the solution to the electrode surface, such processes have been extensively studied by Compton.[83] It is known that for a planar electrode, the current intensity is related to the diffusion of the active specie with the Cottrell equation (Equation 9.1), where where D is the diffusion coefficient, c* represents the bulk concentration and t is the time.

Equation 9.1 - $$j = Dc^* \frac{1}{\sqrt{D\pi t}} \qquad I = \frac{nFA\sqrt{D}c^*}{\sqrt{\pi t}}$$

This typically lead to a peak-shape signal. If the macroelectrode is spherical, the Cottrell equation must take into account another factor, related to the sphere radius r_e, as reported in Equation 9.2.

Equation 9.2 - $$j = Dc^* \left\{\frac{1}{\sqrt{D\pi t}} + \frac{1}{r_e}\right\}$$

At low time values, the radius element is negligible, and the electrode behaves as the planar electrode. In this case, the radius must be higher than the diffusion boundary layer. At high time values, the first term in the braces become negligible and the flux and current can be calculated as reported in Equation 9.3.

Equation 9.3 - $$j = D\frac{c^*}{r_e} \qquad I = 4\pi r_e DFc^*$$

The latter case is characterized by a typical step-like shape, as the diffusion layer has time to expand and the electroactive molecule concentration at the electrode does not decrease over time. This diffusion is called "convergent" and happens when the radius of the spherical electrode is smaller than the diffusion boundary layer.

This shape changing effect can also be observed as the dimension of the electrode changes, as shown in Figure 9.3, for example moving from a macroscopic electrode to a microelectrode or a single nanoparticle.

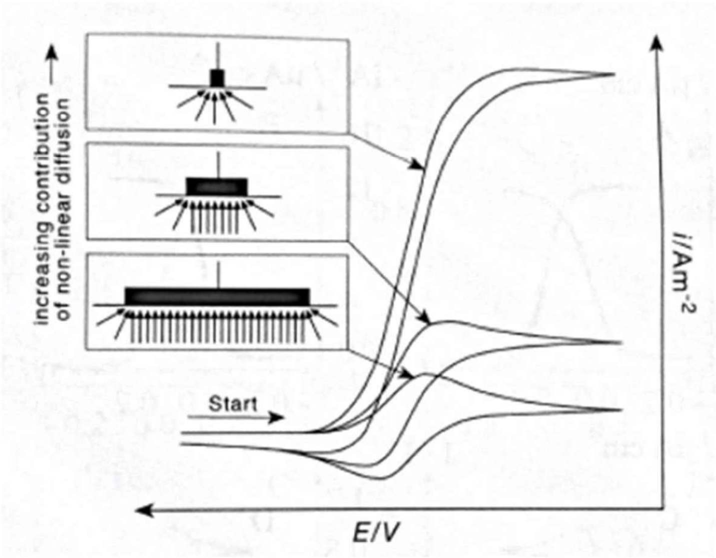

Figure 9.3 - Effect of electrode size on the recorded signal [98]

Small microelectrodes presents many advantages compared to a wide planar one, such as more efficient diffusion, faster kinetic, reduced capacity, limited noise and lower Ohmic drop. It is therefore convenient to engineer the electrode surface to move from a macroscopic active layer to an array of microelectrodes. This can be achieved, for example, by covering the active layer with an insulator, as reported in Figure 9.4.

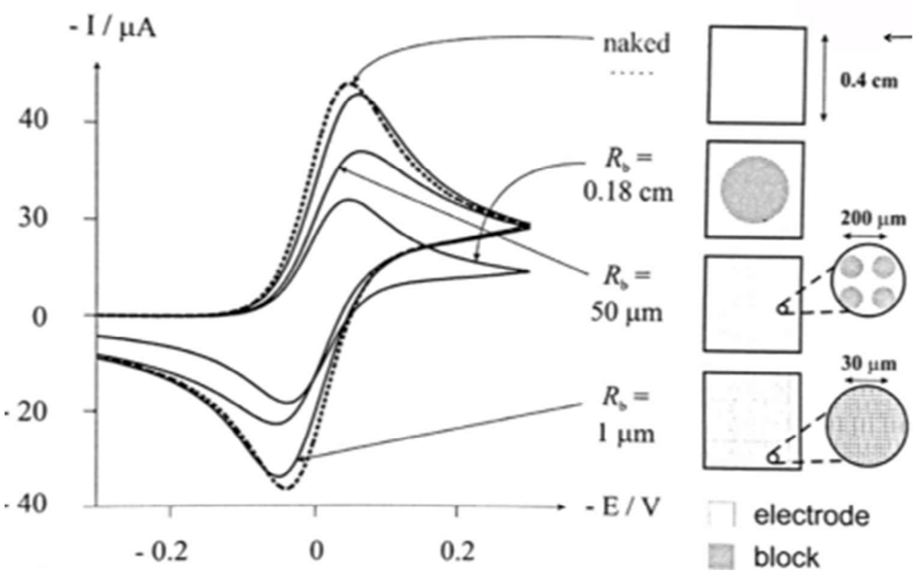

Figure 9.4 - CV recorded for electrodes with different covering distribution on the surface [98]

Such surface morphology greatly affect the electrode behavior. As reported in Figure 9.5, 4 different cases can be observed. In case 1, the insulating material is concentrated in few spots, and linear diffusion takes place on the exposed parts of the electrode. In case 2, exposed parts of the electrode have small dimensions and behave as microelectrodes with non-planar diffusion. As the number of microelectrode increases, and their distance decreases, (case 3) the diffusion layer overlap and the overall effect can be similar to planar diffusion (as shown in case 4).

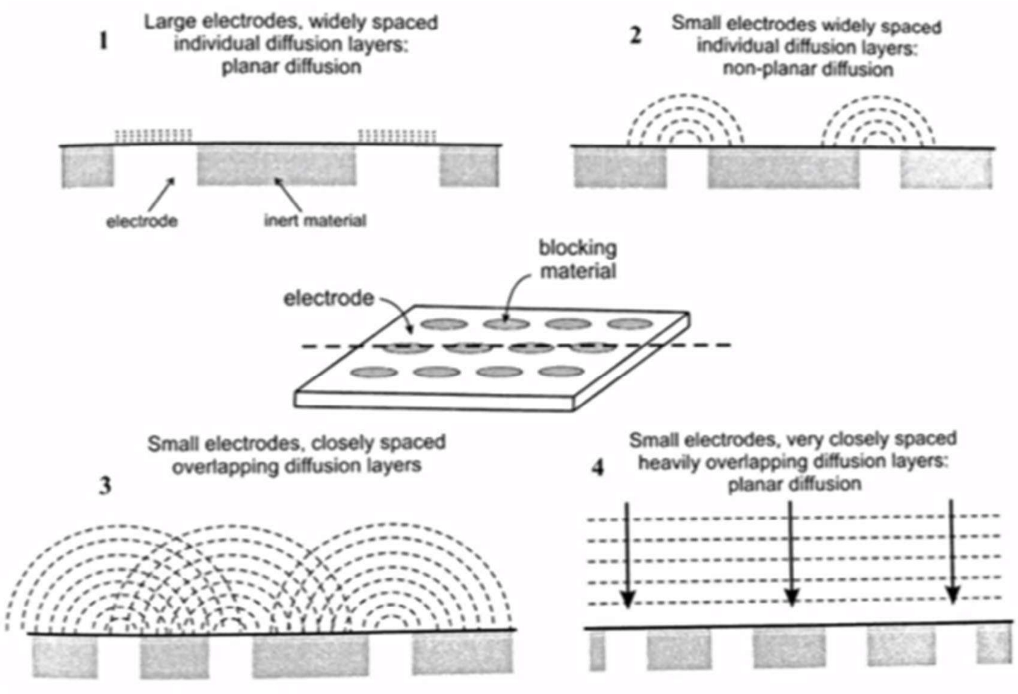

Figure 9.5 - Variation of the diffusion lines at the electrode surface with different covering distribution

Instead of using a blocking material, it is also possible to obtain the same effect by depositing metal nanoparticles in a controlled way, as shown in Figure 9.6.

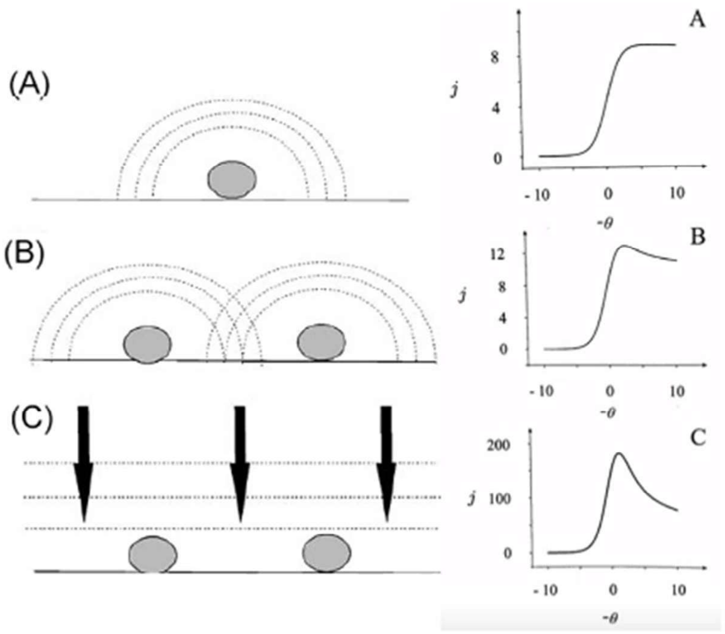

Figure 9.6 - Effect of nanoparticle distribution on the current signal observed in CV

In this case, the current for each particle can be calculated as:

Equation 9.4 $$I_{lim} = 8.71\, n\, F\, D\, c_{bulk}\, r$$

While the overall current equals:

Equation 9.5 $$I_{tot} = I_{lim}\, A\, (10\, r)^{-2}$$

These values can be compared with those of the Randles-Sevcik equation for macroelectrodes:

Equation 9.6 $$I_{peak} = 2.69 \cdot 10^{-5} n^{3/2} D^{1/2} c_{bulk} v^{1/2} A$$

It is possible to evaluate how current values change with the scan rate for different surface coverings. Positive deviations from the Randles-Sevcik plot can be observed with high surface coverage, while low surface coverage will lead to uncomplete diffusion layers overlapping. Therefore, convergent diffusion will prevail, and a negative deviation will be observed. as exemplified in Figure 9.7.

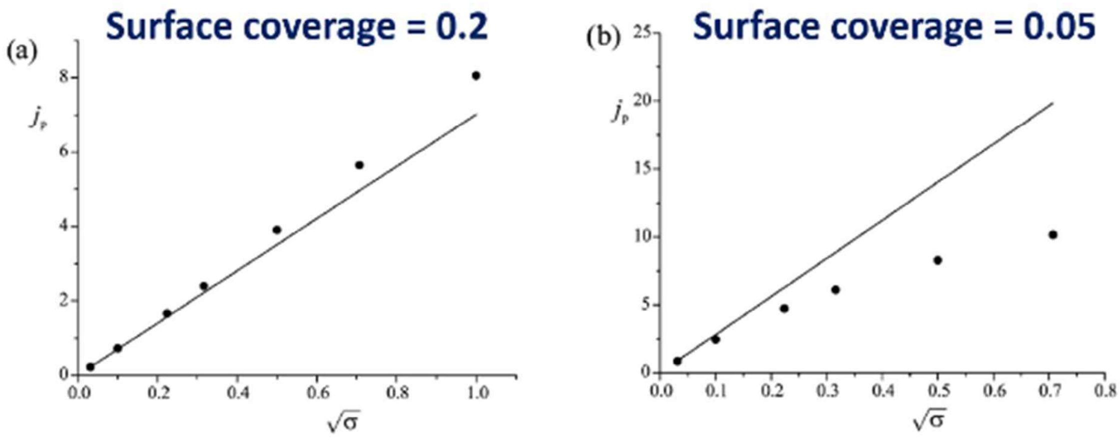

Figure 9.7 - Deviation from the Randles-Sevcik plot with high and low surface coverage

9.2 Impedance spectroscopy

Impedance spectroscopy is a complex electrochemical technique that allows to study the properties of materials and interfaces. In general, this technique allows to see an electrochemical system as its "equivalent circuit", which means to represent it with an electronic circuit (e.g., with resistors and capacities in series or in parallel). The analyses reported in this work are performed in a standard 3-electrode cell, with a platinum counter electrode, a working electrode with the material of interest and a reference electrode (generally Ag/AgCl or SCE). The measure consists in applying an oscillating voltage and recording the corresponding current values. After a mathematical elaboration, data are presented in three forms:

- In the Nyquist plot, data are presented in a graph Z' vs Z". The first one represents the "real part", related to the resistance, while the latter represent the "imaginary part", related to the capacity. The name comes from the mathematical treatment of the data, where imaginary numbers are used. Here, each point is a value of explored frequency and the frequency increases moving from the right of the plot to its left side.
- Bode module plot uses the natural logarithm of |Z| on the y-axis versus the natural logarithm of the frequency value as the x-axis.
- Bode phase plots use the phase value on the y-axis and the logarithm of the frequency of the x-axis.

Nyquist and Bode phase plots will be presented in the following pages. In the Nyquist plot, it is common to observe a semicircle and a line as the one reported in Figure 9.8. [102]

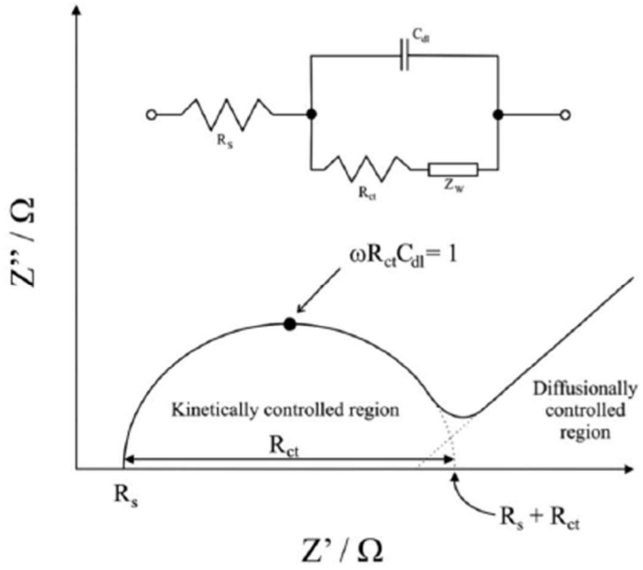

Figure 9.8 - A depiction of a typical impedance spectrum

The measured value of resistance can be obtained by the radius of the semicircle in a Nyquist plot and from the peak in a Bode phase plot. As for the linear part observable at lower frequencies, it is related to mass transfer. If the line's slope is approximately 45°, it is called "Warburg resistance". The value of the slope can be easily read on the y-axis of the Bode phase plot and is equal to 100° for a pure capacitor.

9.3 Chronoamperometry and PEC measurements

Chronoamperometry is an electrochemical techniques that can be performed with an experimental setup similar to the one presented in Figure 9.1. In this case, a constant potential is applied and the current is measures.

This techniques is particularly useful when the material used as WE is photoactive, as it is possible to irradiate the electrode with proper wavelengths to observe a change in the current intensity, as shown in Figure 9.9.[103]

For a n-type semiconductor, like the previously mentioned TiO_2, a photoanode behavior is expected. When the electrode is irradiated at t=0 s, a peak called "transient photocurrent" is observed due to the separation of electron-hole pairs. The presence of holes on the surface causes a flow of electrons towards them (i.e., a negative current), and recombination occurs. This phenomenon leads to a photocurrent decay and the "stationary photocurrent" value is reached. At such point, a steady state is reached in which the rate at which holes reach the interface is exactly balanced by the rate at which they are consumed by charge transfer and recombination, and therefore the photocurrent becomes constant and equal to the current passing across the semiconductor/electrolyte interface.

When irradiation is turned off, a negative overshoot can be observed. This is because the hole flux to the interface is immediately interrupted, while the electron flux continue until all the excess holes are consumed by recombination or charge transfer.

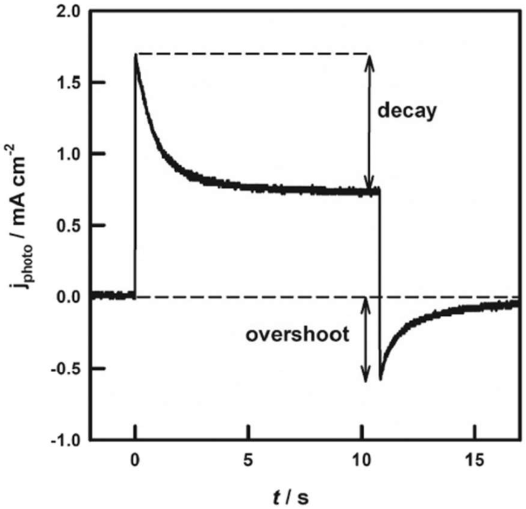

Figure 9.9 - Transient photocurrent response of an α-Fe2O3 electrode showing the typical decay and overshoot interpreted as evidence of surface electron-hole recombination. Note that the 'decay' is significantly larger than the 'overshoot'

The value of current measured at any given time can be calculated according to equation Equation 9.7. Figure 9.10 shows the same process graphically.

Equation 9.7

$$J_{photocurrent}(t) = J_{Hole} + J_{recombination} = J_{charging} + J_{transfer}$$

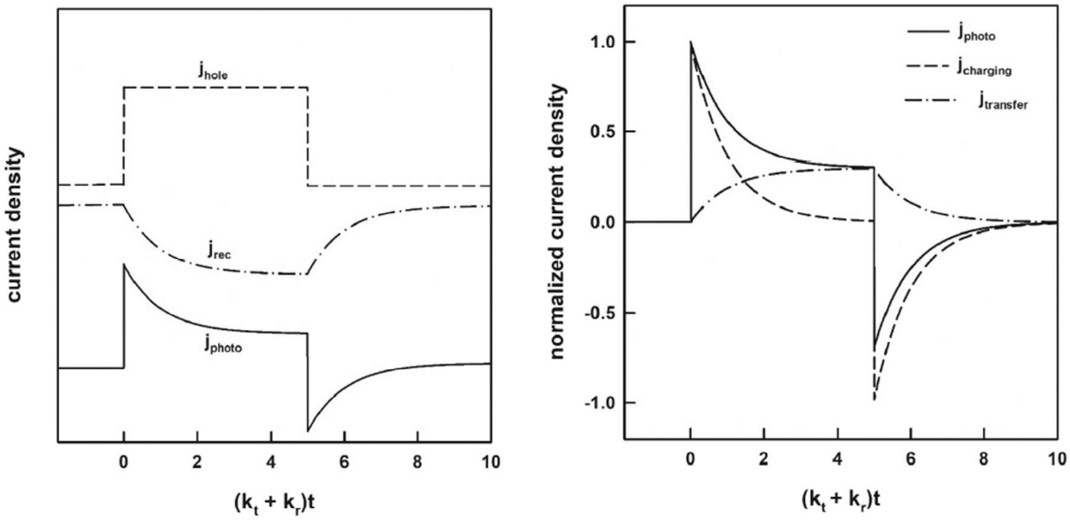

Figure 9.10 - Deconvolution of the photocurrent into contributions from hole and electron current densities (left) and charge transfer and charging/discharging of the space charge capacitance (right)

9.4 UV-Vis spectroscopy

UV-Vis spectroscopy an analytical technique that measures the absorption and transmission of ultraviolet and visible light by a sample. It can be particularly useful for material characterization or quantification of the concentration of a species in solution, often requiring the reparation of a calibration line.

In the instrument, a light beam is generated by lamps, typically a deuterium lamp (UV region) and tungsten-halogen lamp (Visible region) to cover the full spectrum. The light beam, as shown in Figure 9.11, is directed to a dispersive element, usually a prism or a diffraction grating, to divide specific wavelengths in separate beams. The selected beam passes through the sample and reaches the detector, a photodiode or photomultiplier that converts light intensity into an electrical signal.

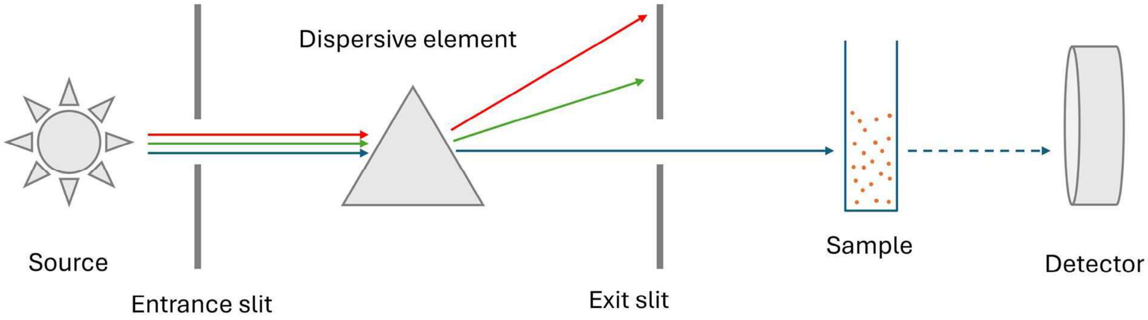

Figure 9.11 - General scheme of a spectrophotometer

For solutions, the obtained value of absorbance can be calculated as reported in Equation 9.8, where A is the absorbance, ε is the Molar absorptivity ($L \cdot mol^{-1} \cdot cm^{-1}$), c the concentration of the analyte (mol/L) and l the path length of the cuvette (usually 1 cm). This law shows that absorbance is directly proportional to the concentration of the sample and the path length—making UV-Vis a powerful tool for quantitative analysis.

Equation 9.8 - $A = \varepsilon \cdot c \cdot l$

For common organic molecules, a signal is related to electronic transitions, typically $\pi \rightarrow \pi^*$ or $n \rightarrow \pi^*$. Specific signal can also be observed for metal nanoparticles, due to the phenomenon of Localized Surface Plasmon Resonance (LSPR). LSPR occurs when conduction electrons on metallic nanoparticles oscillate collectively in resonance with incident light, and is especially common when working with small gold and silver nanoparticles.

Resonance is highly sensitive to nanoparticle size, shape, and surrounding medium. For gold nanoparticles, typical values range between 20–580 nm. A change in peak wavelength can indicate various processes, such as changes in particle size or shape, molecular adsorption on the particle surface or variations in the dielectric environment. The value of intensity, on the other hand, can be used to monitor nanoparticle concentration or aggregation.

9.5 SEM-EDX

An in-depth investigation of the morphology of deposited films and prepared nano- or micro- structures is crucial for better understanding the electrodes' properties. Such characterization can be carried out using Electron Scanning Microscopy (SEM).

This technique uses a focused beam of high-energy electrons to scan the surface of a sample, and allows to obtain information regarding surface topography and composition. As electrons have shorter wavelength compared to traditional light, SEM allows to obtain better resolution compared to optical microscopy, even lower than 1 nm.

Briefly, electrons are generated from a source, usually a tungsten wire, focused and accelerated toward the sample via magnetic lenses. The interaction of the beam and the sample lead to the emission of secondary electrons, backscattered electrons and X-Rays from the sample.

In particular, secondary electrons can be used to obtain information on surface morphology and X-Rays the elemental composition through the so called Energy Dispersive X-Ray (EDX) spectroscopy.

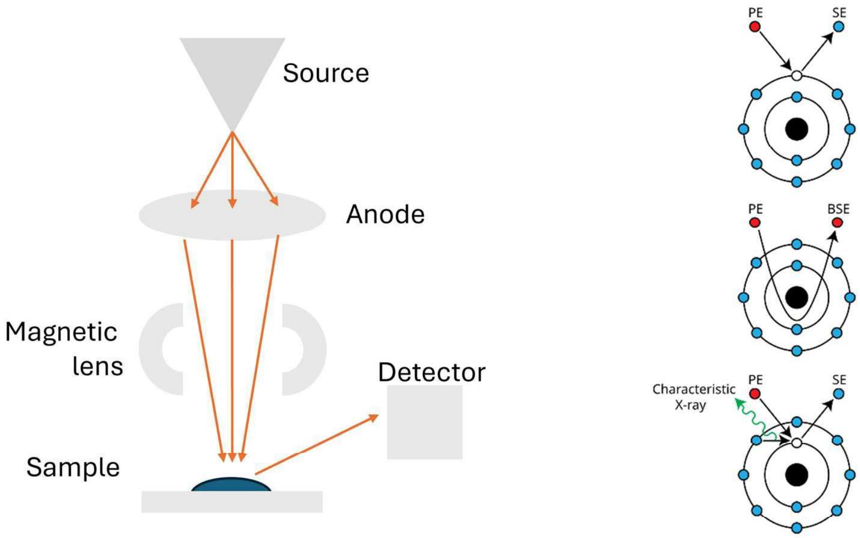

Figure 9.12 - (A) SEM scheme and (B) mechanisms for the production of secondary, backscattered electrons and X-rays

SEM-EDX was extensively used as it allowed to obtain critical information on the electrodes' surface, often complementary to electrochemical and spectroscopical data. Furthermore, the analysis proved to be quick and non-destructive.

9.6 Sputtering

A sputtering machine operates based on a physical vapor deposition (PVD) process used to deposit thin films of material onto a substrate. In this technique, a vacuum chamber is evacuated to a low pressure and filled with an inert gas, typically argon.

A target material, which is the source of the coating, is bombarded by high-energy argon ions generated by a plasma. This ion bombardment causes atoms from the target to be ejected—a process known as sputtering. These ejected atoms then travel through the chamber and condense onto the surface of the substrate, forming a thin, uniform film. Sputtering can be conducted using different methods, such as direct current (DC) sputtering for conductive materials or radio frequency (RF) sputtering for insulating materials. The process offers precise control over film thickness and composition, making it widely used in semiconductor fabrication, optics, and materials science.

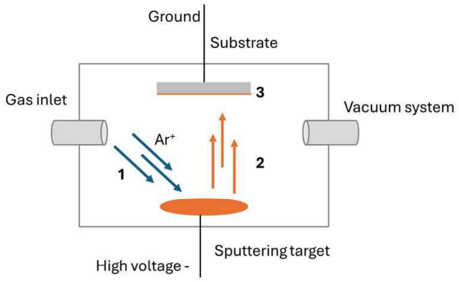

Figure 9.13 - Schematic representation of a sputtering process

10 Appendix 2 - Experimental section

10.1 Preparation of the TiO_2 layer

14.2 g of $Ti(OiPr)_3$ were added in a beaker with 50 cm^3 of EtOH. The solution was poured in a 100 mL flask and 0.45 cm^3 of HCl 37% were added under magnetic stirring. A solution of 0.235 g of Lutensol (a non-ionic surfactant) in 50 cm^3 of ethanol was added in the flask, which was then closed. The solution was stirred for 1 hour and then the sol was stored in glass bottles.

To form the TiO_2 film, the electrode was dipped in the TiO_2 precursor's sol for 60 seconds, then placed in a glass tube with N_2 flux (200 cm^3 min^{-1}) and calcinated in an oven at 400 °C for 1 hour [104–108].

Titanium(IV) isopropoxide (546-68-9), hydrochloric acid 37% (7647-01-0) and ethanol absolute (64-17-5) were purchased at Sigma-Aldrich, while Lutensol ON70 at BASF.

10.2 Preparation of Gold Nanoparticles

Three solutions containing respectively 0.015 g of $AuCl_3$, 0.022 g of trisodium citrate dihydrate and 0.01375 g of PVP10 in 50 cm^3 of water were mixed in a round-bottomed flask using a mechanical stirrer, and a solution prepared by dissolving 0.001875 g of $NaBH_4$ in 1.25 cm^3 of milliQ water was added dropwise. The solution was left under stirring for 15 minutes, kept at room temperature away from light for a few hours and then stored in a plastic bottle at 4 °C.

Gold nanoparticles were prepared using $AuCl_3$ (13453-07-1), trisodium citrate (6132-04-3), PVP10 - Polyvinylpyrrolidone (9003-39-8) and $NaBH_4$ (16940-66-2) purchased at Sigma-Aldrich.

10.3 Deposition of gold nanoparticles

The sensor was prepared on a 2x3 cm FTO support, which was previously sonicated in a 1:1:1 isopropanol:acetone:water solution for 10 minutes, dried with N_2 flux and irradiated for 1 hour with a 500 W UV lamp. The cleaned FTO electrode was dipped in a concentrated H_2SO_4 solution for 90 seconds, then rinsed with water and carefully dried with N_2 flux. The electrode was laid in a reactor created ad hoc, with the conductive side on top, with 18 cm^3 of anhydrous toluene. The reactor was carefully sealed and N_2 was fluxed for 3 minutes before placing it in a crystallizer with water and kept at 70±5 °C for 1 hour.

A solution made with 2 cm^3 of toluene, 36 mm^3 of MPTMS (3-mercaptopropyltrimethoxysilane) and 4 mm^3 of APTES (3-aminopropyltriethoxysilane) was added in the reactor, which had to be kept at 70±5 °C for another 3 hours.

The electrode was then carefully removed from the reactor, rinsed and sonicated with toluene for 3 minutes. The cleaning procedure was also repeated with ethanol and water, before drying with N_2 flow. Such electrode was placed in a petri dish with the conductive side on top and was covered with a gold nanoparticle solution for 1 hour. The excess of solution was later washed away with water, and the surface was dried with N_2 flow.

As for the device preparation, FTO (fluorine tin oxide) covered glass slides (7 Ω/sq), acetone (67-64-1), sulfuric acid (7664-93-9), toluene anhydrous (108-88-3), MPTMS - 3-mercaptopropyltrimethoxysilane (4420-74-0) and APTES – 3-aminopropyltriethoxysilane (919-30-2), where purchased at Sigma-Aldrich while 2-propanol (67-63-0) at Carlo Erba.

10.4 Gold electrodeposition

After the functionalization of the surface with -OH groups, obtained by dipping the electrode in 98% H_2SO_4 solution, the FTO electrode is put in an electrochemical cell (Figure 10.1) as working electrode, with a SCE as reference and a platinum wire as counter electrode. The solution for the deposition is composedby 0.003 M $AuCl_3$in 0.1 M of sodium perchlorate, used as supporting electrolyte.

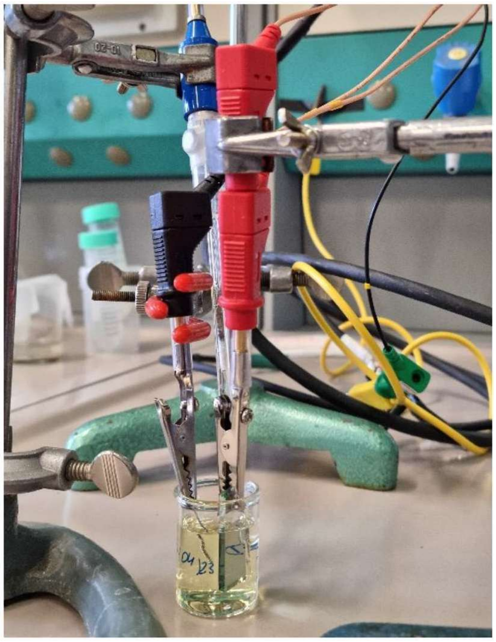

Figure 10.1 - electrochemical cell for the preparation of the electrodeposited electrodes. In the figure it can be seen the platinum wire

The procedure consisted of an applied potential of 1.1V vs SCE for 5 s followed by the electrodeposition at -0.1V for different time, depending on the desired amount of electrodeposited gold (generally between 15 and 60 s).

AuCl3 and $NaClO_4$ were bought from Sigma-Aldrich.

10.5 Gold sputtering and dewetting

Fluorine-doped Tin Oxide (FTO) covered glass slides were carefully cleaned by sonication in a 1:1:1 isopropanol:acetone:water solution and dried with N_2 stream. The obtained samples were located in the vacuum chamber of a sputter machine and hold in place using double sided tape.

A formula developed internally in the PCS Group allowed to estimate the sputtered film tichkness:

$$Thickness = \frac{r_0 \cdot r \cdot W_i \cdot t}{W}$$

Where:

- r_0 = sputter rate copper, provided by the supplier.
- r = sputter rate of copper at power W (0.070 nm/s)
- Wi = Sputtering power of metal i (W)
- t = time of sputtering
- W = Sputtering power of Cu resulting in r as deposition rate (20W)

The deposition was carried out with direct current at 20W, depositing for different times and thus obtaining different thickness, as presented below:

Deposited Thickness	Power	Deposition time
20 nm	20W	150 s
10 nm	20 W	75 s
5 nm	20 W	37.5 s
2.5 nm	20 W	19 s

The obtained samples were placed in a tube furnace with constant Ar flow (50 mL min^{-1}) flow and heated according to the following temperature ramp:

	Time / min	Temperature / °C	Rate / °C min^{-1}	Ar flow / mL min^{-1}
0	120	25	10	50
1	48	500	10	50
2	60	500	10	50
3	180	25	10	50

10.6 Silver electrodeposition

FTO glass slides (1 cm x 3 cm) were pre-treated in order to clean the surface and increase the number of -OH termination. First, the slides were sonicated for 10 minutes in a 1:1:1 (isopropanol: acetone: water) solution, then sonicated in 1:5 nitric acid solution for another 10 minutes.

The obtained electrodes were immersed in a standard 3 electrode cell (immersed area approximately 2 cm^2) with a platinum foil as counter electrode (CE) and a double-salt-bridge reference electrode, consisting of an internal Saturated Calomel Electrode (SCE) and a saturated KNO_3 external solution.

The solution of $AgNO_3$ and citric acid for the metal structure preparation was freshly prepared to prevent reduction. Different metal structures were obtained according to the following procedures:

- silver spheres were obtained using a 50 mL solution containing 2 g L^{-1} of silver nitrate and 40 g L^{-1} of citric acid. Chronopotentiometry was carried out for 50 s at a current value of -1 mA
- silver dendrites were obtained using a 50 mL solution containing 1 g L^{-1} of silver nitrate and 40 g L^{-1} citric acid. The deposition was performed using cyclic voltammetry between 0 and -1.6 V, at a scan rate of 20 mV s^{-1}.

Both the solutions were stirred before starting the deposition. During the deposition the stirring was stopped. The obtained electrodes were briefly rinsed with water to remove excess citric acid and dried with N_2 stream.

FTO (fluorine tin oxide) covered glass slides (7 Ω sq^{-1}), isopropanol (67-63-0), acetone (67-64-1) and HNO_3 (7697-37-2) purchased at Sigma-Aldrich were used as received for the electrode pre-treatments.

$AgNO_3$ (7761-88-8), citric acid (77-92-9) and KNO_3 (7757-79-1) purchased at Sigma-Aldrich were used as received for the silver electrodepositions.

10.7 Instruments

Atomic Force Microscopy (AFM) images were acquired on a Nanoscope Multimode IIId (Bruker) instrument. Root mean squared roughness (RMS) values were determined on 1 x 1 μm^2 areas.

SEM images were acquired with a HITACHI TM-1000, except those presented in Chapter 5, for which a field emission scanning electron microscope (FE-SEM, JEOL JSM-7610F) was used.

EDX analysis were acquired with a HITACHI TM-1000.

Sputtered samples were prepared using a using a magnetron sputter coater (ATC Polaris, AJA International Inc., USA) and dewetted in a tube furnace (Carbo-lite HST12/300).

Electrochemical measurements were recorded using mainly Autolab instrument from MetrOhm (PGSTAT30). The data presented in Chapter 5 were recorded using a BioLogic VMP3 potentiostat.

Irradiation with high power UV lamp was achieved using a 500 W UV Lamp [HG 500] from Jelosil. A distance of 15 cm was maintained between the electrode and the lamp. The UV emission spectra of the lamp is reported in Figure 10.2.

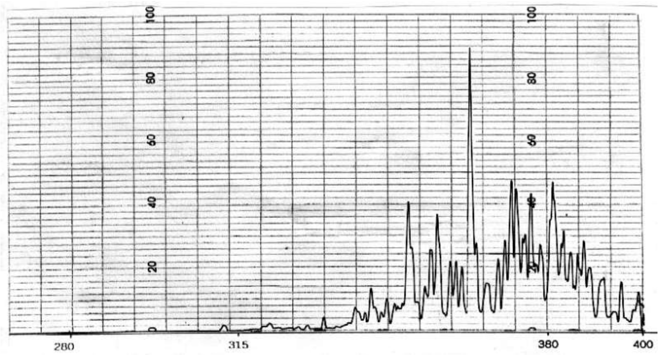

Figure 10.2 - UV emission spectra pof the 500W UV lamp

while low power irradiation was obtained with the LEDD1B power supply from Thorlabs connected to LEDs of various wavelengths (M395L4, M455L4 and M530L4). In order to tur the LED on and off, the power supply was initially controlled with an Arduino Uno and later directly with the Nova 2.0 software of the Autolab instrument.

UV-Vis measurements were recorded using a UV-2600 Spectrophotometer from Shimadzu.

10.8 Measurement parameters

For this work, $NaClO_4$ was used as supporting electrolyte, as it is reported in the literature that perchlorate does not interact with gold surfaces.[52]

Electrochemical measurements were performed in a standard 3-electrode cell consisting in a platinum wire as counter electrode, the modified FTO glass as working electrode and a Saturated Calomel Electrode (SCE) from Amel as reference electrode. $NaClO_4$ 0.1 M was used as support electrolyte.

Only for the study of uncovered dewetted gold structures a specific cell, reported in Figure 10.3, was used. It consisted of a PTFE block with a horizontal cylindrical cavity blocked at one hand by the CE (a Pt-sputtered Ti foil) and on the other hand by the working electrode. Metal plates were used to keep the electrode close and avoid any leak. Two holes were drilled from the top, one to insert the Ag/AgCl RE and one to allow for analyte and solution additions.

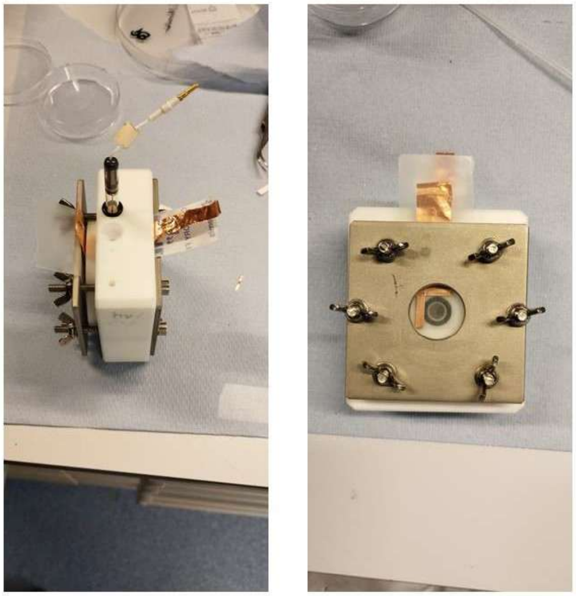

Figure 10.3 - Electrochemical cell used to study the dewetted gold structures

Unless specified otherway, cyclic Voltammetries where recorded with a potential step of 0.008 V and a scan rate of 0.1 V/s, Impedance Spectroscopy was recorded between 65000 Hz and 0.1 Hz with an amplitude of 0.01 V_{RMS}.

Photoelectrochemistry was evaluated by keeping the light source at a controlled distance from the electrode (2 cm for LEDs, 20 cm for the 500W lamp), and the sampling interval was 1s during the dark phase and 0.1 s during the light phase.

H_2O_2 DETECTION

For H_2O_2 detection, 15 cycles were recorded for each addition, between -0.5 V and + 1.3 V vs Ag/AgCl at a scan rate of 0.1 V/s. $NaClO_4$ was used as supporting electrolyte.

STABILITY TESTS

For the stability tests, 10 scans of cyclic voltammetry between +1.2 V and –0.5 V were recorded and then 2 electrochemical impedance spectroscopy measurements were recorded at 0.25 V – the potential at which $K_4[Fe(CN)_6]$ is achieved. EIS frequency was vaied between 65000 Hz and 0.1 Hz with an amplitude of 0.01 V_{RMS}. This sequence was repeated 10 times. The tests were conducted in $NaClO_4$ 0.1 M with the presence of $K_4[Fe(CN)_6]$ 1 mM, which is known in literature to interact with Au structures and cause it's dissolution, in order to accelerate any possible change of the samples.

$NaClO_4$ (7601-89-0) and $[Fe(CN)_6]^{3-/4-}$ (14459-95-1) from Sigma-Aldrich dissolved in milliQ water were used, as received, as supporting electrolyte and electroactive probe, respectively, during the electrochemical tests.

CETIRIZINE QUANTIFICATION

Photocurrent was recorded at + 0.1 V vs SCE, under 395 nm LED illumination. Cycles of 3 minutes of irradiation and darkness were used. The solution was stirred and the analyte was added during the dark phase. DPV was recorded between + 0.2 and - 0.6 V vs SCE. The optimized conditions for the measurements are the following: Step = 0.005 V; Modulation amplitude = 0.1 V; modulation time = 0.05 s; interval time = 0.5 s. N_2 bubbling was used to remove oxygen from the solution and to mix after analyte addition and was stopped while recording DPV. EIS was recorded between 65 kHz and 0.1 Hz with a potential amplitude of 0.01 V_{RMS}.

Cetirizine (83881-52-1), glycerol (56-81-5), paracetamol (103-90-2), diclofenac (15307-79-6), $MgSO_4$ (7487-88-9) and K_3PO_4 (7778-53-2) purchased at Sigma-Aldrich, as received, were tested as analytes.

10.9 Data analysis

Data processing was performed mainly using OriginPro and Microsoft Excel.

Graphs presented throughout the thesis were plotted using OriginPro.

Particle size analysis was performed manually using ImageJ Software.

11 Glossary

CA	Chronoamperometry
CIP	Ciprofloxacin
CTZ	Cetirizine
CV	Cyclic Voltammetry
DEN	Dendrites
DPV	Differential Pulse Voltammetry
EC	Electrochemical
EDX	Energy-Dispersive X-ray
EIS	Electrochemical Impedance Spectroscopy
FTO	Fluorine Doped Tin Oxide
LED	Light Emitting Diodes
LSPR	Localized Surface Plasmon Resonance
NPs	Nanoparticles
PEC	Photo-electrochemical
SCE	Saturated Calomel Electrodes
SEM	Scanning Electron Microscopy
SPH	Spheres
XRD	X-Ray Diffraction

12 References

1. International Measures of Prevention, Application, and Economics of Corrosion Technologies (IMPACT). *NACE International* (2016).
2. Baranwal, J., Barse, B., Gatto, G., Broncova, G. & Kumar, A. Electrochemical Sensors and Their Applications: A Review. *Chemosensors* vol. 10 363 Preprint at https://doi.org/10.3390/chemosensors10090363 (2022).
3. Zhang, X., Guo, Y., Liu, M. & Zhang, S. Photoelectrochemically active species and photoelectrochemical biosensors. *RSC Advances* vol. 3 2846–2857 Preprint at https://doi.org/10.1039/c2ra22238h (2013).
4. Liu, S., Zhan, J. & Cai, B. Recent advances in photoelectrochemical platforms based on porous materials for environmental pollutant detection. *RSC Advances* vol. 14 7940–7963 Preprint at https://doi.org/10.1039/d4ra00503a (2024).
5. Katangur, P., Patra, P. K. & Warner, S. B. Nanostructured ultraviolet resistant polymer coatings. *Polym Degrad Stab* **91**, 2437–2442 (2006).
6. Wang, X. *et al.* Photocatalytic and antifouling properties of TiO2-based photocatalytic membranes. *Materials Today Chemistry* vol. 23 Preprint at https://doi.org/10.1016/j.mtchem.2021.100650 (2022).
7. Liu, T., Liang, R. & Qin, W. Anti-fouling TiO2-Coated Polymeric Membrane Ion-Selective Electrodes with Photocatalytic Self-Cleaning Properties. *Anal Chem* **95**, 6577–6585 (2023).
8. He, X. *et al.* Hierarchical TiO2–Ag/hydrogel coating used for outstanding antifouling detection of serotonin. *Macromol Res* **32**, 553–563 (2024).
9. Hu, X. *et al.* Mechanisms underlying the photocatalytic degradation pathway of ciprofloxacin with heterogeneous TiO2. *Chemical Engineering Journal* **380**, (2020).
10. Qin, J. *et al.* The mechanism of efficient photoreduction nitrate over anatase TiO2 in simulated sunlight. *Chemosphere* **307**, (2022).
11. Comis, S. Toward a better cleaning and selectivity in electroanalysis: TiO2 based sensors and enantioselective materials. (Università degli Studi di Milano, 2023).
12. Mokhtar, B., Kandiel, T. A., Ahmed, A. Y. & Komy, Z. R. New application for TiO2 P25 photocatalyst: A case study of photoelectrochemical sensing of nitrite ions. *Chemosphere* **268**, 128847 (2021).
13. Luttrell, T. *et al.* Why is anatase a better photocatalyst than rutile? - Model studies on epitaxial TiO2 films. *Sci Rep* **4**, (2015).
14. Reverberi, A. P., Kuznetsov, N. T., Meshalkin, V. P., Salerno, M. & Fabiano, B. Systematical analysis of chemical methods in metal nanoparticles synthesis. *Theoretical Foundations of Chemical Engineering* **50**, 59–66 (2016).
15. Jamkhande, P. G., Ghule, N. W., Bamer, A. H. & Kalaskar, M. G. Metal nanoparticles synthesis: An overview on methods of preparation, advantages and disadvantages, and applications. *Journal*

of Drug Delivery Science and Technology vol. 53 Preprint at https://doi.org/10.1016/j.jddst.2019.101174 (2019).

16. Kaliyaraj Selva Kumar, A., Zhang, Y., Li, D. & Compton, R. G. A mini-review: How reliable is the drop casting technique? *Electrochemistry Communications* vol. 121 Preprint at https://doi.org/10.1016/j.elecom.2020.106867 (2020).

17. Pérez-Ràfols, C. *et al.* Ag nanoparticles drop-casting modification of screen-printed electrodes for the simultaneous voltammetric determination of Cu(II) and Pb(II). *Sensors (Switzerland)* **17**, (2017).

18. Li, C. *et al.* Electrochemical Deposition: An Advanced Approach for Templated Synthesis of Nanoporous Metal Architectures. *Acc Chem Res* **51**, 1764–1773 (2018).

19. Tonelli, D., Scavetta, E. & Gualandi, I. Electrochemical deposition of nanomaterials for electrochemical sensing. *Sensors (Switzerland)* vol. 19 Preprint at https://doi.org/10.3390/s19051186 (2019).

20. Harsha, S. *et al.* Dewetting of Pt Nanoparticles Boosts Electrocatalytic Hydrogen Evolution Due to Electronic Metal-Support Interaction. *Adv Funct Mater* https://doi.org/10.1002/adfm.202403628 (2024) doi:10.1002/adfm.202403628.

21. Harsha, S., Wichmann, L., Mul, G. & Altomare, M. An adapted rotating disk electrode setup to test non-standard-disk electrodes: On the enhanced hydrogen evolution performance of model dewetted Pt nanoparticles vs. Pt thin films under hydrodynamic conditions. Preprint at https://doi.org/10.26434/chemrxiv-2025-vlcns (2025).

22. Dierner, M. *et al.* Role of polycrystalline F-SnO2 substrate topography in formation mechanism and morphology of Pt nanoparticles by solid-state-dewetting. *Nanoscale* **17**, 14338–14347 (2025).

23. Altomare, M., Nguyen, N. T. & Schmuki, P. Templated dewetting: designing entirely self-organized platforms for photocatalysis. *Chem Sci* **7**, 6865–6886 (2016).

24. Jiran, E. & Thompson, C. V. Capillary instabilities in thin films. *J Electron Mater* **19**, 1153–1160 (1990).

25. Oh, H., Pyatenko, A. & Lee, M. A hybrid dewetting approach to generate highly sensitive plasmonic silver nanoparticles with a narrow size distribution. *Appl Surf Sci* **542**, (2021).

26. Miliutina, E. *et al.* PVP-assisted thermal annealing of thin Au layer for creation of effective and reproducible SERS substrates. *Nano-Structures and Nano-Objects* **17**, 77–83 (2019).

27. Ruffino, F. & Grimaldi, M. G. Formation of patterned arrays of Au nanoparticles on SiC surface by template confined dewetting of normal and oblique deposited nanoscale films. *Thin Solid Films* **536**, 99–110 (2013).

28. Torrisi, V. *et al.* Characteristics of Pd and Pt nanoparticles produced by nanosecond laser irradiations of thin films deposited on topographically-structured transparent conductive oxides. *Coatings* **9**, (2019).

29. Qi, X. & Bi, J. Plasmonic sensors relying on nanoparticle arrays created by a template-directed dewetting process. *Opt Commun* **453**, (2019).

30. Kracker, M., Worsch, C., Seeber, W. & Rüssel, C. Optical hydrogen sensing with modified Pd-layers: A kinetic study of roughened layers and dewetted nanoparticle films. *Sens Actuators B Chem* **197**, 95–103 (2014).

31. Meshot, E. R., Zhao, Z., Lu, W. & Hart, A. J. Self-ordering of small-diameter metal nanoparticles by dewetting on hexagonal mesh templates. *Nanoscale* **6**, 10106–10112 (2014).

32. Grochowska, K., Siuzdak, K., Karczewski, J., Szkoda, M. & Śliwiński, G. Properties of Thermally Dewetted Thin Au Films on ITO-Coated Glass for Biosensing Applications. *Plasmonics* **12**, 1939–1946 (2017).

33. Scandurra, A., Ruffino, F., Censabella, M., Terrasi, A. & Grimaldi, M. G. Dewetted gold nanostructures onto exfoliated graphene paper as high efficient glucose sensor. *Nanomaterials* **9**, (2019).

34. Scandurra, A., Censabella, M., Gulino, A., Grimaldi, M. G. & Ruffino, F. Gold nanoelectrode arrays dewetted onto graphene paper for selective and direct electrochemical determination of glyphosate in drinking water. *Sensing and Bio-Sensing Research* vol. 36 Preprint at https://doi.org/10.1016/j.sbsr.2022.100496 (2022).

35. Matvieiev, O. *et al.* Effect of different modification by gold nanoparticles on the electrochemical performance of screen-printed sensors with boron-doped diamond electrode. *Sci Rep* **13**, (2023).

36. Choi, J. *et al.* Identification and elimination of false positives in electrochemical nitrogen reduction studies. *Nat Commun* **11**, 5546 (2020).

37. Austin, C. C., Roberge, B. & Goyer, N. Cross-sensitivities of electrochemical detectors used to monitor worker exposures to airborne contaminants: False positive responses in the absence of target analytes. *Journal of Environmental Monitoring* **8**, 161–166 (2006).

38. Fumagalli, D., Comis, S., Pifferi, V. & Falciola, L. Gold Nanoparticles-Titania Heterojunction: Photoelectrochemical Detection of Ciprofloxacin. *ChemElectroChem* **10**, 1–8 (2023).

39. Di Liberto, G., Pifferi, V., Lo Presti, L., Ceotto, M. & Falciola, L. Atomistic Explanation for Interlayer Charge Transfer in Metal-Semiconductor Nanocomposites: The Case of Silver and Anatase. *Journal of Physical Chemistry Letters* **8**, 5372–5377 (2017).

40. Soliveri, G. *et al.* Self-cleaning properties in engineered sensors for dopamine electroanalytical detection. *Analyst* **140**, 1486–1494 (2015).

41. Pifferi, V. *et al.* Photo-renewable electroanalytical sensor for neurotransmitters detection in body fluid mimics. *Anal Bioanal Chem* **408**, 7339–7349 (2016).

42. Pifferi, V. *et al.* Electrochemical sensors cleaned by light: A proof of concept for on site applications towards integrated monitoring systems. *RSC Adv* **5**, 71210–71214 (2015).

43. Aidli, W. *et al.* β-cyclodextrin based platform for bimodal detection of o-toluidine and cholesterol: Electrochemical and fluorescence sensing. *Electrochim Acta* **464**, 142963 (2023).

44. Liu, Q. *et al.* Photoactivities regulating of inorganic semiconductors and their applications in photoelectrochemical sensors for antibiotics analysis: A systematic review. *Biosens Bioelectron* **216**, 114634 (2022).

45. Cao, L. *et al.* Sensitive Photoelectrochemical Determination of Ciprofloxacin Using an Indium Tin Oxide Photoelectrode Modified with Small Gold Nanoparticles. *Anal Lett* **0**, 1–17 (2020).

46. Xu, L. *et al.* Graphitic carbon nitride/BiOCl composites for sensitive photoelectrochemical detection of ciprofloxaci. *J Colloid Interface Sci* **483**, 241–248 (2016).

47. Yan, P. *et al.* Photoelectrochemical monitoring of ciprofloxacin based on metallic Bi self-doping BiOBr nanocomposites. *Electrochim Acta* **259**, 873–881 (2018).

48. Xu, L. *et al.* Metallic Bi self-doping BiOCl composites : Synthesis and enhanced photoelectrochemical performance. *Mater Lett* **196**, 225–229 (2017).

49. Yan, P. *et al.* Enhanced photoelectrochemical sensing performance of graphitic carbon nitride by nitrogen vacancies engineering. *Biosens Bioelectron* **148**, (2020).

50. Shen, B., Wen, X. & Korshin, G. V. Electrochemical oxidation of ciprofloxacin in two different processes: The electron transfer process on the anode surface and the indirect oxidation process in bulk solutions. *Environ Sci Process Impacts* **20**, 943–955 (2018).

51. Zhu, L., Santiago-Schübel, B., Xiao, H., Hollert, H. & Kueppers, S. Electrochemical oxidation of fluoroquinolone antibiotics: Mechanism, residual antibacterial activity and toxicity change. *Water Res* **102**, 52–62 (2016).

52. Gerlache, M., Senturk, Z., Quarin, G. & Kauffmann, J. M. Electrochemical Behavior of H2O2 on Gold. *Electroanalysis* **9**, 1088–1092 (1997).

53. Strbac, S. & Ad~id, R. R. *The Influence of OH-Chemisorption on the Catalytic Properties of Gold Single Crystal Surfaces for Oxygen Reduction in Alkaline Solutions*. *Journal of Electroanalytical Chemistry* vol. 403 (1996).

54. Fawcett, W. R., Fedurco, M., Kovseov5, Z. & Borkowska, Z. *Oxidation of Cysteine, Cysteinesulfinic Acid and Cysteic Acid on a Polycrystalline Gold Electrode*. *Journal of Electroanalytical Chemistry* vol. 368 (1994).

55. Vitl, J. E., Larm, L. A. & Johnson', D. C. *The Importance of Adsorption in Anodic Surface-Catalyzed Oxygen-Transfer Reactions at Electrodes Gold*. vol. 2 (1990).

56. Gallego, J. H., Castellano, C. E., Calandra, A. J. & Arvia, A. J. *THE ELECTROCHEMISTRY OF GOLD IN ACID AQUEOUS SOLUTIONS CONTAINING CHLORIDE IONS*. *J. Electroanal. Chem* vol. 66 (1975).

57. Gardner, J. R. & Woods, R. *THE HYDROPHILIC NATURE OF GOLD AND PLATINUM*. *J. Electroanal. Chem* vol. 81 (1977).

58. Johnston, D. A., Cardosi, M. F. & Huw Vaughan+' +, D. *The Electrochemistry of Hydrogen Peroxide on Evaporated Gold/Palladium Composite Electrodes. Manufacture and Electrochemical Characterization*.

59. Oliveira Brett, A. M., Matysik, F. M. & Vieira, M. T. Thin-Film Gold Electrodes Produced by Magnetron Sputtering. Voltammetric Characteristics and Application in Batch Injection Analysis with Amperometric Detection. *Electroanalysis* **9**, 209–212 (1997).

60. Johnson', D. C. & Lucourse, W. R. *Pulsed Electrochemical Detection at Noble Metal Electrodes in Liquid Chromatography*. *Electroanalysh* vol. 4 (1992).

61. Austin, D. S., Polta, J. A., Polta, T. Z., Tang & Cabelka. Electrocatalysis At Platinum Electrodes For Anodic Electroanalysis. *J. electroanal. Chem* **168**, 227–248 (1984).

62. Burke, L. D. & Buckley, D. T. *The Complex Nature of Hydrous Oxide Film Behaviour on Platinum*. *Journal of Electroanalytical Chemistry* vol. 405 (1996).

63. Aysla Costa De Oliveira, M., D'Epifanio, A., Ohnuki, H. & Mecheri, B. Platinum group metal-free catalysts for oxygen reduction reaction: Applications in microbial fuel cells. *Catalysts* vol. 10 Preprint at https://doi.org/10.3390/catal10050475 (2020).

64. Isse, A. A., Falciola, L., Mussini, P. R. & Gennaro, A. Relevance of electron transfer mechanism in electrocatalysis: The reduction of organic halides at silver electrodes. *Chemical Communications* 344–346 (2006) doi:10.1039/b513801a.

65. Isse, A. A. *et al.* Electrocatalysis and electron transfer mechanisms in the reduction of organic halides at Ag. *J Appl Electrochem* **39**, 2217–2225 (2009).

66. Bellomunno, C. *et al.* Building up an electrocatalytic activity scale of cathode materials for organic halide reductions. *Electrochim Acta* **50**, 2331–2341 (2005).

67. Zahran, M., Khalifa, Z., Zahran, M. A. H. & Abdel Azzem, M. Recent advances in silver nanoparticle-based electrochemical sensors for determining organic pollutants in water: A review. *Materials Advances* vol. 2 7350–7365 Preprint at https://doi.org/10.1039/d1ma00769f (2021).

68. Pagliara, A. *et al. Molecular Properties and Pharmacokinetic Behavior of Cetirizine, a Zwitterionic H 1-Receptor Antagonist*. https://pubs.acs.org/sharingguidelines (1998).

69. Mead, R. N., Barefoot, S., Helms, J. R., Morgan, J. B. & Kieber, R. J. Photodegradation of the antihistamine cetirizine in natural waters. *Environ Toxicol Chem* **33**, 2240–2245 (2014).

70. Kosonen, J. & Kronberg, L. The occurrence of antihistamines in sewage waters and in recipient rivers. *Environmental Science and Pollution Research* **16**, 555–564 (2009).

71. Pavúková, D. *et al.* Removal of Environmentally Harmful and Hardly Degradable Pharmaceuticals Sulfamethoxazole, Diclofenac, and Cetirizine by Adsorption on Activated Charcoal. *Water (Switzerland)* **14**, 3988 (2022).

72. Karakaya, S. & Dilgin, D. G. Low-cost determination of cetirizine by square wave voltammetry in a disposable electrode. *Monatsh Chem* **150**, 1003–1010 (2019).

73. Pushpanjali, P. A. *et al.* Voltammetric analysis of antihistamine drug cetirizine and paracetamol at poly(L-Leucine) layered carbon nanotube paste electrode. *Surfaces and Interfaces* **24**, 101154 (2021).

74. Islam, M. M., Hafsa, N. E., Rahman, M. M., Arifuzzaman, M. D. & Rushd, S. Sensitive Voltammetric Analysis of Cetirizine Using Electrochemical Sensor Based on Poly (methyl orange) Modified Carbon Nanotube Paste Electrode. *Int J Electrochem Sci* **17**, (2022).

75. Killedar, L. S. *et al.* An electrochemical sensor based on graphene oxide/cholesterol nanohybrids for the sensitive analysis of cetirizine. *J Environ Chem Eng* **10**, 2213–3437 (2022).

76. Sawkar, R. R., Shanbhag, M. M., Tuwar, S. M., Mondal, K. & Shetti, N. P. Zinc Oxide–Graphene Nanocomposite-Based Sensor for the Electrochemical Determination of Cetirizine. *Catalysts* **12**, 1166 (2022).

77. Shetti, N. P., Malode, S. J., Nayak, D. S., Aminabhavi, T. M. & Reddy, K. R. Nanostructured silver doped TiO2/CNTs hybrid as an efficient electrochemical sensor for detection of anti-inflammatory drug, cetirizine. *Microchemical Journal* **150**, (2019).

78. Dyakonov, T., Muir, A., Nasri, H., Toops, D. & Fatmi, A. Isolation and characterization of cetirizine degradation product: Mechanism of cetirizine oxidation. *Pharm Res* **27**, 1318–1324 (2010).

79. Rondinini, S. *et al.* Electroreductions on silver-based electrocatalysts: The use of Ag nanoparticles for CHCl3 to CH4 conversion. *Fuel Cells* **9**, 253–263 (2009).

80. Mubarak, M. S. & Peters, D. G. Using silver cathodes for organic electrosynthesis and mechanistic studies. *Current Opinion in Electrochemistry* vol. 2 60–66 Preprint at https://doi.org/10.1016/j.coelec.2017.03.001 (2017).

81. Maino, G. *et al.* Electrochemically assisted deposition of transparent, mechanically robust TiO2 films for advanced applications. *Journal of Nanoparticle Research* **15**, (2013).

82. Maino, G. *et al.* Electrochemically assisted deposition of transparent, mechanically robust TiO2 films for advanced applications. *Journal of Nanoparticle Research* **15**, (2013).

83. Compton, R. G. & Banks, C. E. *Understanding Voltammetry*. *Understanding Voltammetry* (2018). doi:10.1142/q0155.

84. Sanz-Navarro, C. F., Lee, S. F., Yap, S. S., Nee, C. H. & Yap, S. L. Electrochemical stability and corrosion mechanism of fluorine-doped tin oxide film under cathodic polarization in near neutral electrolyte. *Thin Solid Films* **768**, (2023).

85. Li, M. *et al.* A fluorine-doped tin oxide electrode modified with gold nanoparticles for electrochemiluminescent determination of hydrogen peroxide released by living cells. *Microchimica Acta* **184**, 603–610 (2017).

86. Martín, H. *et al.* Influence of adsorbates on the growth mode of gold islands electrodeposited on the basal plane of graphite. *Langmuir* **16**, 2915–2923 (2000).

87. Moradi, K. & Melander, M. M. The Surface Chemistry of Au(111) and Au(100) Electrodes under Oxygen Reduction and Evolution Potentials. *ACS Electrochemistry* https://doi.org/10.1021/acselectrochem.5c00202 (2025) doi:10.1021/acselectrochem.5c00202.

88. Hua, X., Xia, H. L. & Long, Y. T. Revisiting a classical redox process on a gold electrode by operando ToF-SIMS: Where does the gold go? *Chem Sci* **10**, 6215–6219 (2019).

89. Nath Rai, V. & Srivastava, A. K. *Correlation Between Optical and Morphological Properties of Nanostructured Gold Thin Film*. https://www.researchgate.net/publication/308364028 (2016).

90. Tremiliosi-Filho', G., Dall'Antonia, L. H. & Jerkiewicz, G. *Limit to Extent of Formation of the Quasi-Two-Dimensional Oxide State on Au Electrodes*. *Journal of Electroanalytical Chemistry* vol. 422 (1997).

91. Pifferi, V., Barsan, M. M., Ghica, M. E., Falciola, L. & Brett, C. M. A. Synthesis, characterization and influence of poly(brilliant green) on the performance of different electrode architectures based on carbon nanotubes and poly(3,4-ethylenedioxythiophene). *Electrochim Acta* **98**, 199–207 (2013).

92. Łapiński, M. *et al.* Thermal Instability of Gold Thin Films. *Coatings* **13**, (2023).

93. Pasta, M., La Mantia, F. & Cui, Y. Mechanism of glucose electrochemical oxidation on gold surface. *Electrochim Acta* **55**, 5561–5568 (2010).

94. Scandurra, A. *et al*. Model of Chronoamperometric Response towards Glucose Sensing by Arrays of Gold Nanostructures Obtained by Laser, Thermal and Wet Processes. *Nanomaterials* **13**, (2023).

95. Fumagalli, D., Aidli, W., Falciola, L. & Pifferi, V. Bimodal (Photo)electrochemical Sensor for Cetirizine Detection. *Electroanalysis* **37**, (2025).

96. Courtin, E. *et al*. *New Fe 2 TiO 5-Based Nanoheterostructured Mesoporous Photoanodes with Improved Visible Light Photoresponses*.

97. Hirakawa, T. & Nosaka, Y. Properties of O2.- and OH. Formed in TiO2 aqueous suspensions by photocatalytic reaction and the influence of H2O2 and some ions. *Langmuir* **18**, 3247–3254 (2002).

98. Compton, R. G. & Banks, C. E. *Understanding Voltammetry*. *Understanding Voltammetry* (2018). doi:10.1142/q0155.

99. Elgrishi, N. *et al*. A Practical Beginner's Guide to Cyclic Voltammetry. *J Chem Educ* **95**, 197–206 (2018).

100. Wurster, B. *Two-Dimensional Metal-Organic Networks as a New Class of Electrocatalysts*. https://www.researchgate.net/publication/283624265.

101. Lee, J. Electrochemical Sensing of Oxygen Gas in Ionic Liquids on Screen Printed Electrodes. 251 (2014).

102. BARD, A. J., FAULKNER, L. R. *Electrochemical Methods: Fundamentals and Applications*. (Wiley, New York, 2001).

103. Peter, L. M., Walker, A. B., Bein, T., Hufnagel, A. G. & Kondofersky, I. Interpretation of photocurrent transients at semiconductor electrodes: Effects of band-edge unpinning. *Journal of Electroanalytical Chemistry* **872**, 114234 (2020).

104. Maino, G. *et al*. Electrochemically assisted deposition of transparent, mechanically robust TiO2 films for advanced applications. *Journal of Nanoparticle Research* **15**, (2013).

105. Pifferi, V. *et al*. Photo-renewable electroanalytical sensor for neurotransmitters detection in body fluid mimics. *Anal Bioanal Chem* **408**, 7339–7349 (2016).

106. Soliveri, G. *et al*. Self-cleaning properties in engineered sensors for dopamine electroanalytical detection. *Analyst* **140**, 1486–1494 (2015).

107. Di Liberto, G., Pifferi, V., Lo Presti, L., Ceotto, M. & Falciola, L. Atomistic Explanation for Interlayer Charge Transfer in Metal-Semiconductor Nanocomposites: The Case of Silver and Anatase. *Journal of Physical Chemistry Letters* **8**, 5372–5377 (2017).

108. Pifferi, V. *et al*. Electrochemical sensors cleaned by light: A proof of concept for on site applications towards integrated monitoring systems. *RSC Adv* **5**, 71210–71214 (2015).